

CHARACTERIZATION AND MODELING
OF THE INTRINSIC PROPERTIES OF $1.5\mu\text{M}$
 GaInNASb/GaAs LASERS

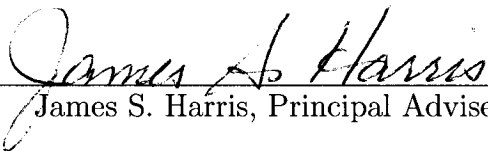
A DISSERTATION
SUBMITTED TO THE DEPARTMENT OF PHYSICS
AND THE COMMITTEE ON GRADUATE STUDIES
OF STANFORD UNIVERSITY
IN PARTIAL FULFILLMENT OF THE REQUIREMENTS
FOR THE DEGREE OF
DOCTOR OF PHILOSOPHY

Lynford Goddard

March 2005

© Copyright by Lynford Goddard 2005
All Rights Reserved

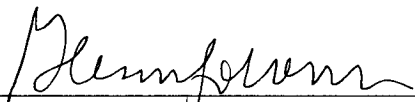
I certify that I have read this dissertation and that, in my opinion, it is fully adequate in scope and quality as a dissertation for the degree of Doctor of Philosophy.


James S. Harris, Principal Adviser

I certify that I have read this dissertation and that, in my opinion, it is fully adequate in scope and quality as a dissertation for the degree of Doctor of Philosophy.


David A. B. Miller

I certify that I have read this dissertation and that, in my opinion, it is fully adequate in scope and quality as a dissertation for the degree of Doctor of Philosophy.


Glenn S. Solomon

Approved for the University Committee on Graduate Studies.

Abstract

Low cost access to optical communication networks is needed to satisfy the rapidly increasing demands of home-based high speed Internet. Existing light sources that operate in the low-loss 1.2-1.6 μm telecommunication wavelength bandwidth are prohibitively expensive for large-scale deployment, e.g. incorporation in individual personal computers.

Recently, we have extended the lasing wavelength of room-temperature continuous wave (CW) GaInNAs(Sb) lasers grown monolithically on GaAs by molecular beam epitaxy (MBE) up to 1.52 μm in an effort to replace the traditional, more expensive, InP-based devices. In addition to lower cost wafers, GaInNAs(Sb) opto-electronic devices have fundamental material advantages over InP-based devices: a larger conduction band offset which reduces temperature sensitivity and enhances differential gain, a lattice match to a material with a large refractive index contrast, i.e. AlAs, which decreases the necessary number of mirror pairs in distributed Bragg reflectors (DBRs) for vertical-cavity surface-emitting lasers (VCSELs), and native oxide apertures for current confinement. High performance GaInNAs(Sb) edge-emitting lasers, VCSELs, and distributed feedback (DFB) lasers have been demonstrated throughout the entire telecommunication band.

In this work, we analyze the intrinsic properties of the GaInNAsSb material system, such as: recombination, gain, band structure and renormalization, and efficiency. Theoretical modeling is performed to calculate a map of the bandgap and

effective masses for various material compositions. We also present current record device performance results, such as: room temperature CW threshold densities below $450\text{A}/\text{cm}^2$, quantum efficiencies above 50%, and over 425mW of total power from a single quantum well (SQW) laser when mounted epitaxial side up and minimally packaged. These results are generally 2-4x better than the previous world records for GaAs based devices at $1.5\mu\text{m}$. The high CW power and low threshold exhibited by these SQW lasers near $1.5\mu\text{m}$ make feasible many novel applications, such as broadband Raman fiber amplifiers and uncooled wavelength division multiplexing (WDM) at the chip scale. Device reliability of almost 500 hours at 200mW CW output power has also been demonstrated. Comparative experiments using innovative characterization techniques, such as: the multiple section absorption/gain method to explore the band structure, as well as the Z-parameter to analyze the dominant recombination processes, have identified the physical mechanisms responsible for improved performance. Also, by measuring the temperature dependence of relevant laser parameters, we have been able to simulate device operation while varying temperature and device geometry.

Acknowledgments

I give special appreciation to my parents, Marilyn and Lawford Goddard, for their loving support throughout the years and for encouraging me to pursue mathematics at a young age; to my brother Lamar, for being a part of so many of my life lessons and for deep discussions about computer science and number theory; to my wife Tiy, for her deep love and compassion and for having the patience for me to discover myself in graduate school; to her parents: Celestine Corrigan and Charlie Martin, and to her siblings: Laticia Brame, Nomi Martin, Jamie Martin, Erin Martin-Rose, and Chessa Hallman for the caring support of an extended family network.

I am extremely grateful to my advisor, Professor James S. Harris (known affectionately as “Coach”) for his support and guidance throughout the years and for welcoming me into his group late in my third year of graduate school. The following year, I thoroughly enjoyed his well-taught semiconductor optoelectronic device classes, EE216 and EE243, and realized that I could learn quite a bit of physics under his supervision. He has a knack for selecting novel research topics that lead to significant advances in the scientific community while still retaining commercial practicability. I am also thankful for his career advice and professional guidance.

I would also like to thank Professor Douglas Osheroff, who served as my undergraduate Physics advisor and graduate mentor/department liaison, helped me find my research group, and served on my oral exam thesis defense committee. Thanks to my reading and oral exam committee members: Professor David A. B. Miller and

Professor Glenn S. Solomon, as well as my oral exam committee chairman, Professor Robert Sinclair. The feedback provided by the entire thesis defense committee was an invaluable assessment of the areas that needed attention in my thesis. I am grateful for the administrative support provided by Gail Chun-Creech, whose tireless effort led to the smooth day-to-day operation of Coach's extremely large research group.

I give thanks to the entire Harris group for providing a strong peer network. Although two years younger, Seth Bank taught me a lot about succeeding in graduate school, in particular how to successfully submit papers to conferences and journals and the keys to a good oral presentation. I am especially grateful to him, and the other growers: Mark Wistey, Homan Yuen, and Hopil Bae, for their tireless efforts in the MBE clean-room improving growth and processing techniques resulting in lasers with world-record performance and so many interesting physical mechanisms for me to characterize. Thanks to the growers and also Vincenzo Lordi, Rafael Aldaz, Evan Thrush, Alireza Khalili, Luigi Scaccabarozzi and Vijit Sabnis for their feedback on some of the experimental techniques, interpretation of measurements results and advice on modeling theory. Great appreciation goes to Zhilong Rao for performing the focused ion beam etches that were so important to the Z-parameter and multiple section gain/absorption measurements.

I would like to thank Professor Alfred R. Adams at the University of Surrey, Professor Nelson Tansu at Lehigh University, and Dr. Dave P. Bour of Agilent Technologies for discussions regarding Auger recombination, carrier leakage, IVBA, and the Z-parameter. I also wish to thank Sarah Zou of Santur Corp. for assistance in wafer thinning and facet coatings and Akihiro Moto of Sumitomo Electric Industries for helpful discussions and donation of substrates. This work was supported under ARO DAAD17-02-C-0101, DARPA MDA972-00-1-0024, NSF PHY-01-40297, and ARO DAAD19-02-1-0184 grants, as well as the Stanford Network Research Center

(SNRC), the Stanford Photonics Research Center (SPRC), and the MARCO Interconnect Research Center. I am deeply grateful to Xerox Palo Alto Research Center (PARC) for two wonderful summer internships that introduced me to semiconductor device physics as well as for providing me with six years of stipend support in the form of a National Physical Science Consortium (NPSC) Fellowship.

Finally, I give all honor and glory to God, the Father Almighty; and peace and love to His people throughout the world. I am eternally grateful for His guidance and protection along my life path.

Dedication

The author wishes to dedicate this dissertation to his lovely wife, Tiy.

Table of Contents

Abstract	iv
Acknowledgments	vi
Dedication	ix
Chapter 1. Introduction	1
1.1 Lightwave Communication Systems	1
1.2 GaInNAsSb/GaAs Material System	6
1.3 Thesis Outline	10
Chapter 2. Band Structure Modeling	11
2.1 Multiband $\mathbf{k} \cdot \mathbf{p}$	11
2.2 Band Anti-Crossing Model	19
2.3 GaInNAsSb Band Structure - Compositional Simulations	24
Chapter 3. Semiconductor Optical Processes: A Study Of Recombina-	
tion, Gain, Band Structure, Efficiency, and Reliability	33
3.1 Laser Growth and Fabrication	34
3.2 Spontaneous Emission	36
3.2.1 Measurement Techniques	36

3.2.2	Results and Discussion	38
3.3	Multi-section Experiments	41
3.3.1	Measurement Techniques	41
3.3.2	Spontaneous Emission and Gain Results	44
3.3.3	Absorption Measurements	47
3.3.4	Band Structure	49
3.3.5	Bandgap Renormalization	55
3.3.6	Carrier Density	56
3.4	Internal Efficiency and Pinning of TSE	58
3.5	Local Z-parameter	62
3.5.1	Theory	62
3.5.2	Experiment	68
3.6	Reliability	73

Chapter 4. Characterization and Comparative Measurements of High

	Performance Lasers	77
4.1	Room Temperature Characterization	79
4.2	Z-Parameter Comparison	84
4.3	Characteristic Temperatures	86
4.4	Relative Intensity Noise (RIN)	91
4.4.1	Definition of RIN	91
4.4.2	RIN Analysis Theory	92
4.4.3	Measurement of RIN	95
4.5	Reliability of High Power Lasers	100

Chapter 5. Laser Modeling 102

5.1	Current-Voltage Characteristics	102
5.2	Thermal Resistance	108

5.3	Waveguide Simulations	114
5.4	Macroscopic Modeling	116
5.5	Microscopic Modeling – The Rate Equation Model	127
Chapter 6.	Conclusion	132
Chapter 7.	Future Research	137
Appendix A.	Laser Test Station	140
Appendix B.	Laser Sample Preparation	146
Appendix C.	Measuring Relative Intensity Noise With An Electrical Spectrum Analyzer	154
Appendix D.	LabView Data Acquisition And Analysis Programs	160
Appendix E.	List Of Acronyms	167

List of Tables

2.1	Binary alloy material parameters at 0K, except for the lattice constant, which is given at 300K.	24
2.2	Non-zero bowing parameters for ternary alloys formed from Ga, In, N, As, and Sb.	25
3.1	Energy level separations and their method of determination for our GaInNAsSb SQW inside GaNAs barriers	50
3.2	Derived band diagram parameters and their method of determination.	53
3.3	Performance metrics during life testing for two $20\mu\text{m} \times 1000\mu\text{m}$ devices at 10mW CW.	73
4.1	Z-parameter and current distribution at threshold.	84
4.2	Cavity length study parameters.	87
4.3	Material and device parameters results for 2^{nd} generation devices. . .	90
4.4	Relative intensity noise study parameters.	93
A.1	Fiber coupling efficiencies for various lens combinations.	144
B.1	Physical properties of various solders and heatsink materials.	148
E.1	List of Acronyms	167

List of Figures

1.1	Internet usage trend in recent years.	2
1.2	Signal transmission distance versus data bandwidth for various fiber systems and operation wavelengths.	2
1.3	Fiber loss for a “wet” and “dry” fiber versus wavelength and desired operating wavelength bands.	3
1.4	Bandgap versus lattice constant of common III-V semiconductor alloys.	7
1.5	Threshold current density versus wavelength for GaIn(N)As(Sb) lasers.	9
2.1	Band Anti-Crossing simulation of the dispersion relation for lattice matched $\text{Ga}_{0.96}\text{In}_{0.04}\text{N}_{0.02}\text{As}_{0.98}$	23
2.2	(Color) (a) Calculated strained bandgap map of GaInNAsSb alloys on a GaAs substrate and (b) Split-off energy, Δ	26
2.3	(Color) Band offsets for (a) electrons, (b) heavy holes, (c) light holes, and (d) split-off holes relative to valence band maximum of InSb.	28
2.4	(Color) Effective masses in the z-direction for (a) electrons, (b) heavy holes, (c) light holes, and (d) split-off holes.	29
2.5	(a) QW band offsets for slight perturbations from the standard recipe of $\text{Ga}_{0.62}\text{In}_{0.38}\text{N}_{0.023}\text{As}_{0.95}\text{Sb}_{0.027}$. (b) Barrier band offsets for slight perturbations from the standard recipe of $\text{GaN}_{0.025}\text{As}_{0.975}$	30
3.1	WINDOW and EDGE measurement configurations for TSE.	36

3.2	(Color) TSE-WINDOW spectra after background subtraction and FFT smoothing for a $20\mu\text{m} \times 306\mu\text{m}$ device. (a) is at $T_a \approx 50^\circ\text{C}$ for 1, 2, and $3\text{kA}/\text{cm}^2$, while (b) is at $3\text{kA}/\text{cm}^2$ for $T_a \approx 50, 90, \text{ and } 120^\circ\text{C}$	39
3.3	Multi-section gain and amplified spontaneous emission configuration.	42
3.4	Normalized TE and TM spontaneous emission spectra at $T_s=15^\circ\text{C}$ for 0.8, 1.2, 1.6, and $2.0\text{kA}/\text{cm}^2$	45
3.5	Material gain spectra at $T_s=15^\circ\text{C}$ for 0.8, 1.2, 1.6, and $2.0\text{kA}/\text{cm}^2$	46
3.6	Peak TE material gain versus current density and logarithmic fit.	46
3.7	Modal absorption spectra of the unpumped section for $T_a \approx T_s=35^\circ\text{C}$	48
3.8	Flat-band diagram with confinement energies for our 800°C annealed, unpumped, $7.8\text{nm Ga}_{0.62}\text{In}_{0.38}\text{N}_{0.023}\text{As}_{0.950}\text{Sb}_{0.027}$ SQW inside of $22\text{nm GaN}_{0.025}\text{As}_{0.975}$ barriers embedded in a GaAs waveguide at $T_a=35^\circ\text{C}$	54
3.9	Quasi-Fermi level separation and carrier concentration versus current density.	56
3.10	Peak TE gain versus carrier concentration and its linear fit.	57
3.11	TSE-EDGE spectra at 15°C at uniformly spaced energies versus current density in pulsed mode.	59
3.12	Simulation of the behavior of the Z-parameter versus carrier density for various recombination mechanisms.	66
3.13	(a) Measured Z-Parameter for $T_s=15-65^\circ\text{C}$ versus current density for a $10\mu\text{m} \times 750\mu\text{m}$ device using WINDOW configuration in CW mode ($J_{th}^{CW}=1.0\text{kA}/\text{cm}^2$ at $T_s=15^\circ\text{C}$) and (b) J_{Trap} and Z_0 versus stage temperature.	68
3.14	(a) Operation current versus time for two $20\mu\text{m} \times 1000\mu\text{m}$ devices at 10mW CW, (b) CW L-I-V curves before life testing and after 50 hours, and (c) Z-J curves during life testing.	72

4.1	CW L-I-V curve for a 20x1222 μm 2 nd generation laser at 20 ° C. . . .	79
4.2	Optical spectra at various operation points for the laser of Fig. 4.1. . .	80
4.3	Pulsed L-I-V curve for a 20x1222 μm 2 nd generation laser at 20 ° C. . .	81
4.4	Dependence of P_{max} and R_s on number of probes.	81
4.5	CW L-I-V curves for a 20x2150 μm 2 nd generation laser at 15 ° C versus number of probe contacts.	82
4.6	Optical spectra at various operation points for the laser of Fig. 4.5. . .	83
4.7	CW L-I-V curves for a 20x2150 μm 2 nd generation laser with 5 probes at 15 ° C.	84
4.8	Z-parameter versus current density for 1 st and 2 nd generation samples at 20 ° C and 55 ° C.	85
4.9	Pulsed L-I curves for a 2 nd generation 20x2150 μm laser at various tem- peratures.	88
4.10	Temperature dependence of J_{th} and η_e for the laser of Fig. 4.9.	88
4.11	Temperature dependence of g_0 , J_{tr} , and J_{th}^∞	89
4.12	Temperature dependence of η_i and α_i	89
4.13	Cavity length dependence of T_0 and T_1	91
4.14	RIN spectrum (linear-scale) and its fit for a 2 nd generation 10x1222 μm laser at 1.2x I_{th} at room temperature.	96
4.15	RIN spectrum (log-scale) for various currents for the laser of Fig. 4.14.	96
4.16	Resonance frequency vs square root of optical power for the laser of Fig. 4.14.	97
4.17	Damping coefficient vs resonance frequency squared for the laser of Fig. 4.14.	97
4.18	Temperature dependence of dg/dn and ε for the laser of Fig. 4.14. . .	99
4.19	Time evolution of I_{op} and V_{op} at 200mW CW output from a 20x2150 μm 2 nd generation laser.	101

5.1	Series resistances for six devices of varying length and width and the fitted series resistance of Equation 5.7.	104
5.2	Series resistances versus temperature for a 5, 10, and 20 μm wide stripe of length 1222 μm	105
5.3	V_0 versus $-nk_B T/q \cdot \text{Ln}(A)$ at 15 ° C.	106
5.4	$qV_0/nk_B T + \text{Ln}(A)$ versus temperature for the 5, 10, and 20 μm wide stripe of length 1222 μm	107
5.5	R_{th} versus mesa stripe width and the theoretical prediction (no free fit parameters) of Equation 5.16 for a 983 μm long sample.	111
5.6	Individual contributions of the substrate, solder, and heatsink to R_{th} (log-scale) versus mesa stripe width for a 983 μm long sample.	111
5.7	Simulation of R_{th} versus mesa stripe width for a 983 μm long sample mounted epi-down to a copper heatsink for 1, 5, and 10 μm thicknesses of ^{100}In solder.	112
5.8	Simulation of R_{th} versus mesa stripe width for a 983 μm long sample for our current epi-up mounting and for epi-down mounting to AlN, Cu, and diamond CVD heatsinks using a 1 μm thickness of ^{100}In solder.	113
5.9	(Color) Waveguide simulations for a 10 μm wide ridge. (a) Contours of constant E-field magnitude in 10% steps. (b) and (c) cross-sectional views of the E-field profile.	115
5.10	L-I-V simulations. (a) Simulation and experimental data for a typical 10x1222 μm device at 15 ° C and (b) for an outstanding 20x1222 μm device at 20 ° C.	117
5.11	Epi-up standard mounting; box plot simulations of a 20 μm wide SQW laser versus cavity length under CW operation. (a) threshold current, (b) threshold density, (c) external efficiency, and (d) maximum output power.	118

5.12	Epi-down mounting to diamond; box plot simulations of a $20\mu\text{m}$ wide SQW laser versus cavity length for comparison with epi-up mounting in Fig. 5.11.	119
5.13	Epi-up standard mounting (a) and (b) and Epi-down mounting to diamond (c) and (d); box plot simulations of a $20\times 1000\mu\text{m}$ HR coated SQW laser versus output facet reflectivity.	122
5.14	Epi-up standard mounting (a) and (b) and Epi-down mounting to diamond (c) and (d); box plot simulations of a $1000\mu\text{m}$ long SQW laser versus ridge width.	123
5.15	Epi-up standard mounting (a) and (b) and Epi-down mounting to diamond (c) and (d); box plot simulations of a $20\mu\text{m}$ wide DQW laser versus cavity length for comparison with SQW laser mounted epi-up in Figs. 5.11(b) and 5.11(d) and epi-down in Figs. 5.12(b) and 5.12(d).	125
5.16	Epi-up standard mounting; box plot simulations of a $20\times 1000\mu\text{m}$ wide laser versus number of quantum wells.	126
5.17	(Color) Simulations of eye diagram, small signal response, relative intensity noise, and L-I characteristics using the rate equation model for a $10\times 500\mu\text{m}$ laser.	128
5.18	(Color) Simulations of carrier and photon dynamics for a $10\times 500\mu\text{m}$ laser under a 5mA modulation.	130
A.1	Voltage and current monitoring circuit.	141
B.1	SEM image of a $750\mu\text{m}$ long HR coated bar with a windows etched in the top metal.	147
C.1	RIN measurement setup.	157

C.2	Overall electrical gain of the RIN measurement system as a function of frequency.	157
C.3	System noise sources as a function of input DC optical power.	158
C.4	Overall RIN measurement sensitivity with and without noise subtraction as a function of input DC optical power.	158
D.1	(Color) LabView main program front panel with L-I-V data from our 1 st CW laser.	161

Chapter 1

Introduction

1.1 Lightwave Communication Systems

In the last decade, the incredible growth in consumer demand for high-speed Internet in the home and on the desktop (See Fig. 1.1) has created a pressing need for **low cost** access to optical communication networks. As a result, the requirements for data bandwidth, network capacity, and repeater-free transmission distance of the local, metro, wide, and storage area networks are constantly being pushed to unprecedented performance levels. Text and pictures still constitute the bulk of information on the Internet and so ever-growing consumer demand should be expected as online video entertainment and communication continue to expand.

As shown in Fig. 1.2, the transmission distance decreases quite rapidly as a function of the data bandwidth of the optical network. At low data rates, the transmission distance in fiber is limited by optical attenuation. At high data rates, the distance is limited by group velocity dispersion, i.e. the difference in transmission speeds for different wavelengths. There is a far more substantial drop in transmission distance as a function of data rate in the high speed, dispersion-limited regime. Intermodal dispersion causes an additional reduction in the transmission distance in multimode fibers or for Fabry-Pérot lasers.

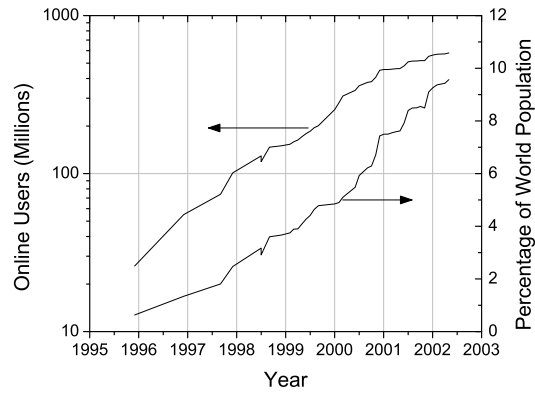


Figure 1.1: Internet usage trend in recent years. (Source: Nua Ltd. [1])

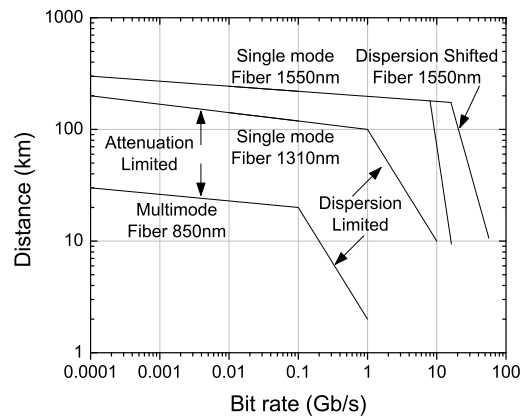


Figure 1.2: Signal transmission distance versus data bandwidth for various fiber systems and operation wavelengths.

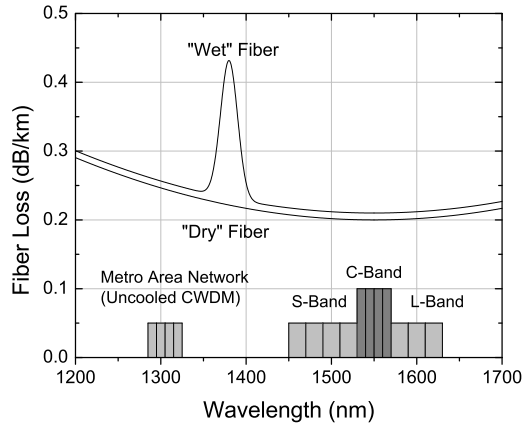


Figure 1.3: Fiber loss for a “wet” and “dry” fiber versus wavelength and desired operating wavelength bands. Water absorption causes a peak near 1400nm.

Optical networks conventionally use either vertical-cavity surface-emitting lasers (VCSELs) or distributed feedback (DFB) lasers and operate at 850, 1310, or 1550nm. VCSELs offer low cost 2-D scalability, while DFB lasers provide better single mode operation, i.e. higher side mode suppression ratios. GaAs is the established material system for laser sources at 850nm because of its low manufacturing cost, and excellent reliability, speed, and thermal performance. In the late 1970s, 45Mb/s with 10km repeater spacing was demonstrated. This enabled a much larger repeater spacing compared with the 1km spacing of existing coaxial electrical networks and significantly reduced the dominant cost of the data network, namely the installation and maintenance of the repeaters. However, operation at 850nm is limited primarily to local area networks today because of the incredibly short transmission distance under the demands of Gb/s operation.

Most landline and intercontinental silica fibers deployed in the 1980s and 1990s have a low fiber loss bandwidth window between 1200 and 1700nm as shown in Fig. 1.3. Rayleigh scattering, which decreases as $1/\lambda^4$, is the dominant loss at short wavelengths, while infrared absorption, which depends on the impurity concentration

of the fiber, dominates at long wavelengths. In the last decade, the water absorption peak near 1400nm has been virtually eliminated from commercially available “dry” fibers. The overall telecommunications bandwidth window is divided into six bands: original (O) 1260-1360nm, extended (E) 1360-1460nm, short wavelength (S) 1460-1530nm, conventional (C) 1535-1565nm, long wavelength (L) 1565-1625nm, and ultra-long wavelength (U) 1625-1675nm.

Time division multiplexing (TDM) or wavelength division multiplexing (WDM) is used to increase the system capacity without having to dig up and re-lay additional fibers. Bits associated with different channels are interleaved in the time or wavelength domain to form a composite bit stream that is de-multiplexed at the receiver end. WDM is more prevalent because the effective data transmission bit rate can be greatly increased by multiplexing hundreds of channels without increasing the channel modulation rate. Thus, there is considerable research and commercial interest in developing optoelectronic devices throughout the entire low-loss bandwidth to fully utilize the data carrying capacity of the fiber.

Two specific wavelengths of interest are 1310nm (center of O-band) and 1550nm (center of C-band) because of the zero dispersion and minimum attenuation at these wavelengths, respectively. Due to low dispersion, dense wavelength division multiplexing (DWDM) or uncooled coarse wavelength division multiplexing (CWDM) at 1310nm are ideal solutions for metro area networks because of the high number of simultaneous users. The International Telecommunication Union (ITU) generally defines DWDM as 8 or more channels per fiber; the standard channel spacing is 50 or 100GHz (0.4 or 0.8nm at 1550nm) for DWDM systems, while for CWDM it is defined to be 20nm (2.5THz at 1550nm) [2]. For long-haul networks, uncooled CWDM or temperature controlled DWDM can be used in the S, C, and L bands. Historically, InGaAsP semiconductor lasers on InP substrates have been the material system at

both wavelengths and nearly every long-wavelength ($>1.1\mu\text{m}$) laser in optical networks today is fabricated in this material system. However, the manufacturing costs are prohibitively expensive for large-scale deployment, e.g. incorporation in individual personal computers.

Even at 1550nm, fiber losses need to be periodically compensated in long-haul networks. This can be accomplished in an all-optical network with erbium doped fiber amplifiers (EDFAs) spaced 60-80km apart [3]. Erbium ions are excited to population inversion through optical pumping. Efficiencies as high as 11dB gain at 1550nm per 1mW at 980nm have been achieved [4]. However, the usable bandwidth of an EDFA covers only the C-band since the gain bandwidth is determined by the energy level of the ions. On the other hand, Raman amplifiers have a much wider gain window, determined by the wavelength of the pump. Raman amplifiers use stimulated Raman scattering (SRS), a process in which a pump photon gives up its energy to create another signal photon of reduced energy ($\approx 15\text{THz}$ or 120nm redshift) and optical phonons. Thus, it is possible to amplify a signal at any wavelength simply by selecting the appropriate pump wavelength. However, a high power CW source ($>300\text{mW}$ on fiber), very near to the signal wavelength, is needed for SRS.

Dispersion-shifted fibers, where the zero dispersion point is engineered to coincide with the minimum attenuation point at 1550nm, are becoming more widely deployed [5] due to the increased transmission distance above 10Gb/s (shown in Fig. 1.2), which creates the possibility of long-haul DWDM at 1550nm. This is an additional motivation for low-cost, low-threshold, uncooled, directly modulated, laser sources at 1550nm. Easily integrable semiconductor optoelectronic devices, such as: detectors, modulators, and switches will also be needed to realize all-optical networks, chip-scale optical links and photonic integrated circuits. A single material system where all of these devices can be grown economically and monolithically will certainly revolutionize the telecommunications industry.

1.2 GaInNAsSb/GaAs Material System

One of the most critical requirements that a proposed material system must satisfy is that the semiconductor alloy must be nearly lattice matched to readily available substrates, e.g. GaAs or InP. If the lattice mismatch is too large ($\approx 3-4\%$ for an 8nm quantum well layer), the resulting strain will relax by generating dislocations and the laser will fail because of high non-radiative recombination. In addition to the adequately lattice-matched alloy at the desired wavelength for the active region layer, wider bandgap lattice-matched alloys with lower refractive index are also needed for carrier and optical confinement. Fig. 1.4 shows the bandgap of common III-V semiconductor alloys as a function of lattice constant using the band structure models developed in Chapter 2; the vertical lines below GaAs and InP indicate lattice match to these substrate materials. Material compositions with a sufficiently close lattice match for growth of a quantum well layer on GaAs fall within the shaded regions. There is a wider region on the high lattice constant side of GaAs since high quality material can be grown at In concentrations as high as $\approx 40\%$ whereas a maximum of only $\approx 3-4\%$ of N is possible for laser quality material.

As mentioned previously, InGaAsP on InP has been the conventional material system for the low-loss fiber window. A major limitation of the InP based system is that the lattice-matched alloys have small refractive index differences. This increases the manufacturing difficulty for distributed Bragg reflectors (DBRs), an essential component of VCSELs. Fortunately, GaAs and AlAs are lattice matched and have a large refractive index difference. Since AlAs has a wider bandgap and lower refractive index than GaAs and arbitrary compositions of the ternary alloy $\text{Al}_x\text{Ga}_{1-x}\text{As}$ can be grown, it is much easier to make waveguides, separate confinement heterostructures, and DBRs in GaAs based devices. Further, AlGaAs can be selectively oxidized to define current apertures or to increase the index contrast for novel devices, such as photonic

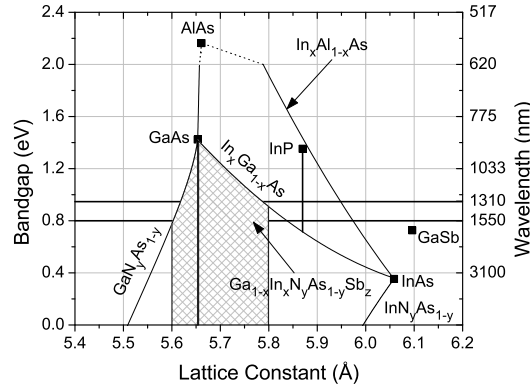


Figure 1.4: Bandgap versus lattice constant of common III-V semiconductor alloys. The vertical lines that are connected to GaAs and InP correspond to lattice matched alloys.

bandgap crystals. However, even in the mid 1990s, it was believed that there were no suitable alloys that are lattice matched to GaAs and that could lase beyond $1.1\mu\text{m}$. Thus, great effort was made to circumvent the shortcomings of the InGaAsP/InP system through non-epitaxial techniques, such as: fabricating DBR mirrors using metal mirrors [6], wafer bonded AlAs/GaAs mirrors [7], combined InGaAsP/InP and AlAs/GaAs metamorphic mirrors [8], AlGaAsSb/AlAsSb mirrors [9], dielectric mirrors [10] and InP/air mirrors [11, 12]. However, these solutions necessarily increase the manufacturing difficulty and cost or result in substandard performance making them impractical for widespread integration.

In 1994 (and 1996), Kondow and co-workers [13, 14] discovered that adding dilute amounts of nitrogen to GaAs (InGaAs) to form GaNAs (GaInNAs) dramatically reduced the bandgap. This allows the possibility of reaching much longer wavelengths while still maintaining lattice match to GaAs. The result contradicted the general trend of all previously studied III-V alloys that small lattice constant alloys have large bandgaps. It was particularly unexpected, since GaN (located way off the scale in the upper left corner of Fig. 1.4) has a much larger bandgap than GaAs

and zinc blende InN has a larger bandgap than InAs, though not by as much as was originally thought [15]. This unusual bandgap decrease will be described in Chapter 2. High quality growth of GaInNAs beyond $1.3\mu\text{m}$ has been challenging due to the large number of defects created by growing these highly metastable alloys at low temperatures. Research groups began adding Sb to push to longer wavelengths [16–18]. Sb acts both as a surfactant, which allows incorporation of more N while still maintaining crystal quality, and as a constituent, which naturally lowers the bandgap. Since N primarily affects the conduction band, Sb affects the valence band, and In affects both bands, it is conceivable that the extra degree of freedom in the quinary (five component) alloy will not only allow control of bandgap and lattice match, but also of the band offset ratio. This will be discussed at the end of Section 2.3.

Besides being lattice matched to GaAs/AlAs, GaInNAs(Sb) devices have several advantages over InGaAsP. First, the conduction band offset ratio is larger in GaInNAs(Sb) [14, 19, 20]. Since the electron effective mass is smaller than the heavy hole mass, electron confinement is more critical and so the larger offset ratio provides better overall carrier confinement. Confining electrons in a deeper quantum well results in less temperature sensitivity and enhanced differential gain, which facilitate uncooled and high-speed operation, respectively. Second, the thermal and electrical conductivity of the cladding layers or DBR mirrors is superior, which reduces junction heating. Third, due to the (essentially) unity sticking coefficients of In and N, the compositional control is much simpler for GaInNAs(Sb) compared to InGaAsP where both the In:Ga and As:P ratios must be accurately controlled to maintain the lattice match and emission wavelength. Fourth, GaAs wafers have lower cost and have higher yield than InP since they are less brittle and the manufacturing process is simpler. Also, due to the difficulty in fabricating DBR mirrors, the majority of InP based lasers are edge-emitters, which require expensive fiber pig-tailing or alignment modules and lack the 2-D scalability of VCSELs. Finally, due to its enormous

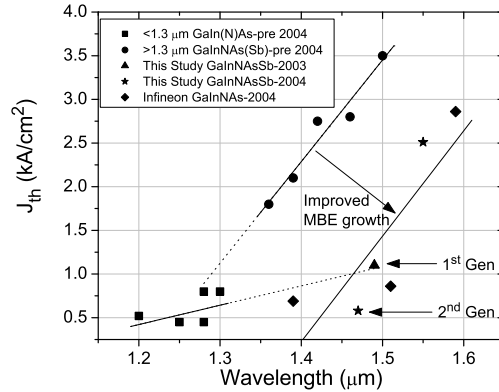


Figure 1.5: Threshold current density versus wavelength for long wavelength GaIn(N)As(Sb) lasers. Previously, there was a sharp rise in threshold density beyond $1.3\mu\text{m}$. Through improved growth and processing, the frontier for rising thresholds has been extended to $1.5\mu\text{m}$. We will discuss 1^{st} generation devices in Chapter 3 and compare them to 2^{nd} generation devices in Chapter 4.

bandgap range, from 0.75 to 1.4eV, GaInNAs(Sb) is the single material system we are looking for, where the entire low-loss window can be covered and an assortment of uncooled semiconductor devices can be monolithically integrated.

GaInNAs(Sb) edge-emitting lasers [17, 21–29], vertical-cavity surface-emitting lasers (VCSEL) [30–34], and distributed feedback (DFB) lasers [35, 36], grown monolithically on GaAs, have been demonstrated throughout the low-loss telecommunication bandwidth. The main fabrication issue has been the rapid degradation of material quality and device performance due to the large number of defects created as the nitrogen concentration is increased to extend the lasing wavelength beyond $1.3\mu\text{m}$. See Fig. 1.5. However, we have significantly reduced monomolecular recombination [37], the previous cause of high thresholds, by reducing ion-related damage during active layer growth [38–40] and minimizing defects by optimizing the rapid thermal annealing (RTA) process [40]. The reduced non-radiative recombination has also increased the differential quantum efficiency, output power, and reliability. By achieving room

temperature threshold densities below $500\text{A}/\text{cm}^2$ and CW output powers exceeding 425mW at $1.5\mu\text{m}$, we have demonstrated that the GaInNAsSb material system is capable of meeting the industry requirements for high power pump laser applications and could displace InP-based devices throughout the low-loss window.

1.3 Thesis Outline

This thesis is divided into seven chapters and five appendices. In Chapter 2, we discuss band structure modeling using the multiband $\mathbf{k} \cdot \mathbf{p}$ model, the Pikus-Bir strain Hamiltonian, and the Band Anti-Crossing model. We calculate the bandgaps, band offsets, and effective masses as a function of material composition in the GaInNAsSb material system. In Chapter 3, we present recombination measurements for GaInNAsSb lasers at $1.5\mu\text{m}$ for comparison with existing reports for GaInNAs/GaAs at $1.3\mu\text{m}$ and InGaAsP/InP at 1.3 and $1.5\mu\text{m}$ [41–43]. We also report on experimental measurements of gain, band structure, efficiency and reliability at $1.5\mu\text{m}$ for comparison with GaInNAs/GaAs at $1.3\mu\text{m}$ [15, 44–46] and InGaAsP/InP at 1.3 and $1.5\mu\text{m}$ [47–49]. In Chapter 4, we perform comparative measurements of the Z-parameter, which track the dominant sources of recombination, to investigate the improvements in device performance. Through the method of characteristic temperatures, we analyze the temperature sensitivity of gain, efficiency, and loss. We also study the temperature dependence of the differential gain, dg/dn , and non-linear gain compression factor, ε , by analyzing the relative intensity noise (RIN) spectra. Both analyses lead to a deeper understanding of device behavior with temperature or bias and enable us to perform modeling of laser performance in Chapter 5. We draw conclusions and summarize the intrinsic material parameters in Chapter 6. Future research areas are suggested in Chapter 7. The appendices provide detailed descriptions of the experimental set-up, laser testing methodology, data acquisition software and a list of acronyms used.

Chapter 2

Band Structure Modeling

Band structure modeling is important for laser device design and the analysis of gain, absorption, and spontaneous emission. There are several models for calculating the energy band structure of semiconductors, e.g. multiband $\mathbf{k} \cdot \mathbf{p}$ [50, 51], empirical tight-binding [52], and pseudopotential [53] models. Multiband $\mathbf{k} \cdot \mathbf{p}$ is the most straightforward and widely used model for direct bandgap semiconductors. It is invaluable in calculating the energy bandgap and dispersion near the Brillouin zone center in the effective mass approximation and has been generalized to include the effects of strain through the Pikus-Bir Hamiltonian [54, 55].

2.1 Multiband $\mathbf{k} \cdot \mathbf{p}$

Multiband $\mathbf{k} \cdot \mathbf{p}$ uses time-independent degenerate perturbation theory and Löwdin's renormalization near an extremum, such as the zone center $\mathbf{k}=0$, to determine the energy dispersion relationship. Using Bloch's theorem, the electronic wavefunctions for the periodic lattice potential are expressed as:

$$\psi_{n\mathbf{k}}(\mathbf{r}) = e^{i\mathbf{k} \cdot \mathbf{r}} u_{n\mathbf{k}}(\mathbf{r}) \quad (2.1)$$

where $u_{nk}(\mathbf{r})$ depend on the band index n and wave vector \mathbf{k} and are periodic:

$$u_{nk}(\mathbf{r} + \mathbf{R}) = u_{nk}(\mathbf{r}) \quad (2.2)$$

where $\mathbf{R} = n_1 \mathbf{a}_1 + n_2 \mathbf{a}_2 + n_3 \mathbf{a}_3$, and \mathbf{a}_1 , \mathbf{a}_2 , and \mathbf{a}_3 are the unit lattice vectors and n_1 , n_2 , and n_3 are integers. The functions $u_{nk}(\mathbf{r})$ solve the unit cell Schrödinger equation, which includes spin-orbit interaction [56]:

$$\left[H_0 + \frac{\hbar^2 k^2}{2m_0} + \frac{\hbar}{4m_0^2 c^2} \nabla V \times \mathbf{p} \cdot \sigma + \frac{\hbar}{m_0} \mathbf{k} \cdot \mathbf{p} + \frac{\hbar^2}{4m_0^2 c^2} \nabla V \times \mathbf{k} \cdot \sigma \right] u_{nk}(\mathbf{r}) = E_n(\mathbf{k}) u_{nk}(\mathbf{r}) \quad (2.3)$$

where V is the atomic potential, σ is the Pauli spin matrix and the free particle Hamiltonian H_0 is given by:

$$H_0 = \frac{p^2}{2m_0} + V(\mathbf{r}) \quad (2.4)$$

The last term on the left-hand side of Equation 2.3 is usually neglected since the crystal momentum \mathbf{k} is generally small compared to the atomic momentum \mathbf{p} . At the zone center, $\mathbf{k} = 0$ and $u_{n0}(\mathbf{r})$ satisfies the simpler equation:

$$\left[H_0 + \frac{\hbar}{4m_0^2 c^2} \nabla V \times \mathbf{p} \cdot \sigma \right] u_{n0}(\mathbf{r}) = E_n(\mathbf{0}) u_{n0}(\mathbf{r}) \quad (2.5)$$

For zinc-blende materials, e.g. our GaInNAsSb lasers, it is convenient to work with the basis functions of definite total angular momentum. By convention, the top of the valence band of the unstrained quantum well is set as the zero of energy. For the conduction band, the basis functions of the lowest energy bands are:

$$\left| \frac{1}{2}, \frac{\pm 1}{2} \right\rangle = \left| iS, \frac{\pm 1}{2} \right\rangle \quad (2.6)$$

for electrons, with energy E_g , where $|S\rangle = S(r)$ is spherically symmetric. For the valence band, the lowest bands are:

$$\left| \frac{3}{2}, \frac{\pm 3}{2} \right\rangle = \frac{\mp 1}{\sqrt{2}} \left| X \pm iY, \frac{\pm 1}{2} \right\rangle \quad (2.7)$$

$$\left| \frac{3}{2}, \frac{\pm 1}{2} \right\rangle = \frac{\mp 1}{\sqrt{6}} \left| X \pm iY, \frac{\mp 1}{2} \right\rangle + \sqrt{\frac{2}{3}} \left| Z, \frac{\pm 1}{2} \right\rangle \quad (2.8)$$

$$\left| \frac{1}{2}, \frac{\pm 1}{2} \right\rangle = \frac{1}{\sqrt{3}} \left| X \pm iY, \frac{\mp 1}{2} \right\rangle \pm \frac{1}{\sqrt{3}} \left| Z, \frac{\pm 1}{2} \right\rangle \quad (2.9)$$

for heavy, light and split-off holes, respectively. The energy is $E_0 + \Delta/3=0$ for the heavy and light holes and $-\Delta$ for the split-off holes, where E_0 is the eigenenergy of the degenerate eigenfunctions of H_0 : $|X\rangle = xf(r)$, $|Y\rangle = yf(r)$, and $|Z\rangle = zf(r)$. The split-off energy, Δ , is defined as:

$$\Delta \equiv \frac{3\hbar i}{4m_0^2 c^2} \left\langle X \left| \frac{\partial V}{\partial x} p_y - \frac{\partial V}{\partial y} p_x \right| Y \right\rangle \quad (2.10)$$

and is typically determined experimentally. The spin-orbit coupling splits the six-fold degeneracy into four-fold degenerate $\mathbf{J}=3/2$ bands (heavy and light hole) and two-fold degenerate $\mathbf{J}=1/2$ bands (split-off hole).

For $\mathbf{k} \neq 0$, the wavefunctions $u_{nk}(\mathbf{r})$ are expanded as a linear superposition of the $\mathbf{k}=0$ basis eigenfunctions with the valence band wavefunctions (Equations 2.7- 2.9) grouped into class A and analyzed separately from class B, which consists of the conduction band wavefunctions (Equation 2.6) and any other remote conduction or valence bands. The idea is to consider band mixing among states of class A, which have similar energy, and determine an effective Hamiltonian for these states by iteratively solving (Löwdin's renormalization) for the perturbative influence of class B states, usually only to first order. The mixing of the eigenfunctions of Equation 2.5 is caused precisely by the $\mathbf{k} \cdot \mathbf{p}$ term in Equation 2.3 and thus explains the model's name.

After strain effects are included, the general result is that the effective Hamiltonian for 6x6 $\mathbf{k} \cdot \mathbf{p}$ theory is given by [57]:

$$H \equiv - \begin{bmatrix} P+Q & -S & R & 0 & -\frac{1}{\sqrt{2}}S & \sqrt{2}R \\ -S^+ & P-Q & 0 & R & -\sqrt{2}Q & \sqrt{\frac{3}{2}}S \\ R^+ & 0 & P-Q & S & \sqrt{\frac{3}{2}}S^+ & \sqrt{2}Q \\ 0 & R^+ & S^+ & P+Q & -\sqrt{2}R^+ & -\frac{1}{\sqrt{2}}S^+ \\ -\frac{1}{\sqrt{2}}S^+ & -\sqrt{2}Q & \sqrt{\frac{3}{2}}S & -\sqrt{2}R & P+\Delta & 0 \\ \sqrt{2}R^+ & \sqrt{\frac{3}{2}}S^+ & \sqrt{2}Q & -\frac{1}{\sqrt{2}}S & 0 & P+\Delta \end{bmatrix} \begin{matrix} |\frac{3}{2}, \frac{3}{2}\rangle \\ |\frac{3}{2}, \frac{1}{2}\rangle \\ |\frac{3}{2}, \frac{-1}{2}\rangle \\ |\frac{3}{2}, \frac{-3}{2}\rangle \\ |\frac{1}{2}, \frac{1}{2}\rangle \\ |\frac{1}{2}, \frac{-1}{2}\rangle \end{matrix} \quad (2.11)$$

where P, Q, R, and S are each the sum of crystal momentum and strain terms (e.g. $P=P_k+P_\varepsilon$):

$$\begin{aligned} P_k &= \frac{\hbar^2}{2m_0} \gamma_1 k^2 & P_\varepsilon &= -|a_v| \text{Tr}(\varepsilon) \\ Q_k &= \frac{\hbar^2}{2m_0} \gamma_2 (k^2 - 3k_z^2) & Q_\varepsilon &= \frac{-b}{2} (\text{Tr}(\varepsilon) - 3\varepsilon_{zz}) \\ R_k &= \frac{\hbar^2}{2m_0} \sqrt{3} (-\gamma_2 (k_x^2 - k_y^2) + 2i\gamma_3 k_x k_y) & R_\varepsilon &= \frac{\sqrt{3}}{2} b (\varepsilon_{xx} - \varepsilon_{yy}) - id\varepsilon_{xy} \\ S_k &= \frac{\hbar^2}{2m_0} 2\sqrt{3}\gamma_3 (k_x - ik_y)k_z & S_\varepsilon &= -d(\varepsilon_{xz} - i\varepsilon_{yz}) \end{aligned} \quad (2.12)$$

where γ_1 , γ_2 , and γ_3 are the Luttinger parameters and are determined by various $\mathbf{k} \cdot \mathbf{p}$ matrix elements between states in class A and class B, a_v , b , and d are the Pikus-Bir deformation potentials and $\text{Tr}(\varepsilon) = \varepsilon_{xx} + \varepsilon_{yy} + \varepsilon_{zz}$ is the fractional change in volume of the crystal under uniform deformation. The absolute value of a_v is used to reconcile differing sign conventions found in the literature [58, 59]. For our case of a strained semiconductor layers grown pseudomorphically on a (001)-oriented substrate, the layers experience biaxial strain and the strain tensor elements are given

by [60]:

$$\begin{aligned}\varepsilon_{xx} &= \varepsilon_{yy} = \frac{(a_0 - a)}{a} \\ \varepsilon_{zz} &= -2\frac{C_{12}}{C_{11}}\varepsilon_{xx} \\ \varepsilon_{xy} &= \varepsilon_{yz} = \varepsilon_{zx} = 0\end{aligned}\tag{2.13}$$

where a_0 and a are the lattice constants of the host (substrate) and layer, respectively and C_{12} and C_{11} are elastic stiffness tensor coefficients. Thus, for biaxial strain, $\text{Tr}(\varepsilon) = 2(1 - C_{12}/C_{11})\varepsilon_{xx}$ and $R_\varepsilon = S_\varepsilon = 0$ in Equation 2.12.

Solving for the eigenenergies of Equation 2.11 to second order in \mathbf{k} gives the band edge energies and effective masses in the z -direction and transverse (x or y) direction [61]:

$$\begin{aligned}E_{HH}(\mathbf{0}) &= -P_\varepsilon - Q_\varepsilon \\ E_{LH}(\mathbf{0}) &= -P_\varepsilon + Q_\varepsilon + (r_+ - s)\Delta \\ E_{SO}(\mathbf{0}) &= -P_\varepsilon + r_- \Delta\end{aligned}\tag{2.14}$$

$$\begin{aligned}m_{HH}^z &= \frac{m_0}{\gamma_1 - 2\gamma_2} & m_{HH}^t &= \frac{m_0}{\gamma_1 + \gamma_2} \\ m_{LH}^z &= \frac{m_0}{\gamma_1 + 2f_+ \gamma_2} & m_{LH}^t &= \frac{m_0}{\gamma_1 - f_+ \gamma_2} \\ m_{SO}^z &= \frac{m_0}{\gamma_1 + 2f_- \gamma_2} & m_{SO}^t &= \frac{m_0}{\gamma_1 - f_- \gamma_2}\end{aligned}\tag{2.15}$$

where

$$\begin{aligned}s &= \frac{Q_\varepsilon}{\Delta} \\ r_\pm &= \frac{s - 1 \pm \sqrt{1 + 2s + 9s^2}}{2} \\ f_\pm(s) &= \frac{2s(1 + 3r + 3s)}{2r + 3r^2 - 3s^2}\end{aligned}\tag{2.16}$$

Note that if $s \ll 1$, i.e. the split-off energy, Δ , is large compared to the strain energy, Q_ε , so that there is negligible mixing with the split-off band, then $r_+ = s$, $r_- = -1$, $f_+ = 1$, and $f_- = 0$. In that limit, m_{SO} becomes isotropic and has a value of m_0/γ_1 ; however, there is a small correction to this effective mass if an $8 \times 8 \mathbf{k} \cdot \mathbf{p}$ unstrained Hamiltonian

is used [48] and so we propose a simple patching of the two results:

$$m_{SO}^z = \frac{m_0}{\gamma_1 - \gamma_{SO} + 2f - \gamma_2} \quad m_{SO}^t = \frac{m_0}{\gamma_1 - \gamma_{SO} - f - \gamma_2} \quad (2.17)$$

where

$$\gamma_{SO} = \frac{E_p \Delta}{3E_g(E_g + \Delta)} \quad (2.18)$$

Switching from a 6x6 to 8x8 $\mathbf{k} \cdot \mathbf{p}$ model, the heavy hole and light-hole masses are not significantly modified [48, 62].

For the lowest conduction band, a similar process is used with the lowest conduction band now being considered class A and the valence bands and other remote conduction bands being considered as class B. The result is that the band edge energy and conduction band effective mass are [48, 63]:

$$E_c(\mathbf{0}) = E_g + a_c \text{Tr}(\varepsilon) \quad (2.19)$$

$$m_e^z = m_e^t = \frac{m_0}{1 + 2F + \frac{E_p(3E_g + 2\Delta)}{3E_g(E_g + \Delta)}} \quad (2.20)$$

where a_c is the conduction band deformation potential, E_p and F are parameters determined by various matrix elements of \mathbf{p} between the conduction band and valence band or remote bands, respectively.

To calculate the band edges, offsets, and effective masses of strained III-V semiconductor alloys, the Luttinger parameters, Pikus-Bir deformation potentials, stiffness tensor coefficients, split-off energy, unstrained bandgap energy, lattice constant, and E_p and F parameters are needed. Conventionally, the majority of these properties are calculated using linear interpolation (Vegard's law) of the experimentally determined values for the binary alloy. The one notable exception is that interpolation of the

valence band masses along the z-direction and also of the difference $\gamma_3 - \gamma_2$ are recommended, rather than direct interpolation of the individual Luttinger parameters, in order to account for valence-band warping [48]. However, this procedure neglects strain effects and so we will proceed cautiously with direct interpolation of the individual Luttinger parameters. In the absence of strain, the effective mass along the important z-direction should be approximately the same using the two procedures (interpolation of m^z compared to interpolation of $1/m^z$). In the transverse direction, however, there may be more sizable discrepancies.

A bowing parameter, C, is usually included in the interpolation of the bandgap for ternary alloys to account for the deviation from the linear interpolation between two binary alloys A and B:

$$E_g(A_{1-x}B_x) = (1-x)E_g(A) + xE_g(B) - x(1-x)C \quad (2.21)$$

For most III-V alloys, the alloy bandgap is typically smaller than the linear interpolation result and so C is positive. A non-zero bowing parameter, C_P , may be included to account for non-linearity in a parameter, P, in a similar fashion to the bandgap bowing parameter. For quaternary alloys of the form $D_xE_{1-x}F_yG_{1-y}$ (two column III elements, D and E, and two column V elements, F and G), a weighted average of the four ternary alloys: DEF, DEG, DFG, EFG is used and additional bowing is neglected [15]:

$$P_{DEFG} = \frac{x(1-x)[(1-y)P_{DEG} + yP_{DEF}] + y(1-y)[(1-x)P_{EFG} + xP_{DFG}]}{x(1-x) + y(1-y)} \quad (2.22)$$

provided that either x or y is strictly between zero and one, i.e. a true quaternary and not a ternary. For the quinary $D_{1-x}E_xF_yG_{1-y-z}H_z$, with a third column V element,

H, the average can be expressed in terms of the nine ternary alloys:

$$P_{DEFGH} = \frac{\sum c_{ijk} P_{ijk}}{\sum c_{ijk}} \quad (2.23)$$

where c_{ijk} are the fractional composition components, e.g. $c_{ijk} = xy(1 - y - z)$ for EFG and the ternary parameter P_{EFG} is calculated for the same F:G ratio as was present in the quinary. Again, it is necessary that at least one of x , y or z is strictly between zero and one so that the denominator is nonzero. One must avoid over generalizing the averaging techniques, as averaging over three quaternary alloys to make up the quinary would give incorrect results. Equation 2.23 will only be used sparingly for III-N-V semiconductors since the addition of nitrogen strongly affects many parameters as will be discussed in Section 2.2.

The temperature dependence of most parameters is ignored except for bandgap, which is modeled by:

$$E_g(T) = E_g(0) - \frac{\alpha T^2}{T + \beta} \quad (2.24)$$

where α and β are the Varshni parameters, to be determined experimentally and the lattice constant, which is assumed to increase linearly:

$$a(T) = a(300) + \frac{da}{dT}(T - 300) \quad (2.25)$$

where $a(300)$ and da/dT ($\approx 2.5 \times 10^{-5} \text{ \AA/K}$) depend on material composition (see Table 2.1) and are also determined experimentally. As a consequence of Equation 2.24 we should also expect the band offsets to be temperature dependent since α and β are material dependent. Using the results of the thermodynamic analysis of Vechten and Malloy [64], the temperature dependence of the band positions for any III-V alloy is

given by:

$$\begin{aligned} CBO_{AB}(T) &\equiv E_c^A(T) - E_c^B(T) = E_c^A(0) - E_c^B(0) - 1.77\left(\frac{\alpha T^2}{T+\beta}\Big|_A - \frac{\alpha T^2}{T+\beta}\Big|_B\right) \\ VBO_{AB}(T) &\equiv E_v^A(T) - E_v^B(T) = E_v^A(0) - E_v^B(0) - 0.77\left(\frac{\alpha T^2}{T+\beta}\Big|_A - \frac{\alpha T^2}{T+\beta}\Big|_B\right) \end{aligned} \quad (2.26)$$

where CBO and VBO are the conduction and valence band offsets of material A relative to material B. This can be a sizable effect for some material combinations, e.g. the CBO for GaAs relative to InSb is 62meV larger at 300K compared to 0K, but this effect is smaller for more lattice matched materials and so the correction is generally within the experimental uncertainty of band offset measurements in the literature.

2.2 Band Anti-Crossing Model

The above procedures for band structure modeling yield accurate results for the majority of III-V semiconductors with the notable exception of dilute nitrides. The bandgap energy for GaN is 3.3eV for zinc-blende or 3.5eV for wurtzite, which is much larger than the bandgap of GaAs 1.4eV. Thus, the rapid bandgap reduction of GaN_yAs_{1-y} [13] or Ga_{1-x}In_xN_yAs_{1-y} [14] cannot be accurately modeled using interpolation, even if a bowing parameter is included. In 1999, Shan and co-workers used photoreflectance (PR) to measure the conduction band energy as a function of the applied hydrostatic pressure and proposed Band Anti-Crossing (BAC) as a semi-empirical model to explain the observed conduction band splitting and unusual bandgap reduction of InGaAs with the addition of dilute amounts of nitrogen [65].

The BAC model is based on an interaction between the conduction band and a narrow resonant band of localized N states. Nitrogen has a large electronegativity, which is the power of an atom in a molecule to attract electrons to that atom. The electronegativities of Ga, In, N, As, and Sb are 1.81, 1.78, 3.04, 2.18, and 2.05,

respectively [66, 67]. These values are on the Pauling scale, which ranges from 0.7 for Fr to 3.98 for F. The large electronegativity of N leads to stronger electron localization around the N atom in III-N bonds compared to the column III atoms or even the As or Sb atoms in III-As or III-Sb bonds. Since these electronic states are localized in real space, they are spread out in momentum space and so a flat energy-wavevector dispersion is assumed.

The interaction of the resonant band of localized N states with the conduction band is modeled using perturbation theory by the BAC Hamiltonian [15, 65, 68]:

$$H_{BAC} = \begin{bmatrix} E_M(k) & V_{MN}\sqrt{y} \\ V_{MN}\sqrt{y} & E_N \end{bmatrix} \begin{matrix} |\Phi_M\rangle \\ |\Phi_N\rangle \end{matrix} \quad (2.27)$$

where $E_M(k)$ is the conduction band dispersion of the unperturbed nitride-free semiconductor after the overall strain effects of the nitride-containing semiconductor have been included. In other words, the position of $E_M(0)$ is given by adding the nitride-free semiconductor bandgap to the nitride-containing valence band maximum position plus the nitride-containing conduction band strain energy contained in Equation 2.19; the effective mass is determined with Equation 2.20 using the nitride-free parameters. E_N is the position of the nitrogen isoelectronic impurity level in that semiconductor, V_{MN} is the interaction matrix element between the two bands and y is the nitrogen concentration. E_N and V_{MN} are temperature independent empirical parameters. V_{MN} is assumed to be pressure and strain independent, while E_N is slightly pressure dependent, 15-25meV/GPa [65, 69], compared to the 100-120meV/GPa for $E_M(k)$ in $\text{Ga}_{1-x}\text{In}_x\text{N}_y\text{As}_{1-y}$ depending on the In concentration [65, 69]. Thus, the strain dependence of V_{MN} is neglected while a small deformation potential, a_N , for the nitrogen level of -0.65eV is assumed [69]. The original BAC model assumes that the valence band states are unaffected; however a small linear shift of 30meV per percent N for the chemical valence band offset, i.e. the band offset in the absence of strain,

of GaNAs relative to GaAs is assumed [69] for better agreement with data in the literature, which mostly indicate a type-I alignment for low N concentrations. We will assume that this nitrogen induced valence band shift occurs at the same rate for all ternary III-N-V alloys and will use it to calculate the net valence band offsets of dilute nitride ternary alloys (III-N-V).

The dependence of the model's empirical parameters E_N and V_{MN} on material composition must be carefully chosen to obtain the correct bandgaps and effective masses; however, there is insufficient data in the literature to cover the wide range of alloys possible in the GaInNAsSb material system. For GaInNAs, Vurgaftman and Meyer argue that the position of the E_N level should be independent of the host material in the absence of strain [15]. This location is 1.65eV above the valence band of GaAs. This value yields consistent results with reports in the literature at the two endpoints of $E_N=1.65\text{eV}$ for GaNAs and $E_N=1.44\text{eV}$ for InNAs. The effect of adding Sb has not been well parameterized, mainly due to the scarcity of reports in the literature on InNSb and no reports on GaNSb because of the very large miscibility gaps in these alloys. A value of $E_N=0.65\text{eV}$ for InNSb has been determined [15], which is 200meV lower than what would be obtained under the assumption that the E_N level is independent of the host material. We believe that this discrepancy is due to the large difference in electronegativities for As and Sb. The reduced electronegativity of Sb compared to As allows the electron to be more tightly bound to the N atom and thereby increases its distance to the vacuum level. To account for this difference and to make the existing reports on E_N consistent, we propose that the value of E_N for Sb containing alloys should be reduced linearly by 2.0meV per percent Sb. This assumption will be validated if future reports on GaNSb show a similar 200meV reduction for E_N .

For the compositional dependence of V_{MN} in GaInNAs, Vurgaftman and Meyer recommend an interpolation as in Equation 2.21 using the values of 2.7eV for GaNAs

and 2.0eV for InNAs with a bowing parameter of 3.5eV [15]. However, there are wide discrepancies in the literature for V_{MN} with 20-40% In concentrations. For similar GaInNAs compositions, the value has ranged from 1.7eV [70, 71] to 2.5eV [72] and depending on which electron QW level is involved from 2.8 to 3.0eV [73]. Thus, the bowing parameter for V_{MN} is not well defined. We will assume zero bowing of V_{MN} and simply use linear interpolation of the known values for GaNAs and InNAs. This will produce values of V_{MN} closer to those obtained in [72] and [73]. As before, the dependence on Sb is not well known. With the reduced electronegativity of Sb, the electron will couple more strongly with the N atom and thereby increase the interaction strength V_{MN} . A value of $V_{MN}=3.0\text{eV}$ for InNSb has been determined [15], which is higher than the $V_{MN}=2.0\text{eV}$ value for InNAs. Thus, we again propose a linear interpolation of the value from InNAs to InNSb, i.e. 10.0meV increase per percent Sb.

Combining the above analysis with the pressure dependent results in [69], the values for E_N and V_{MN} relative to the valence band maximum of $\text{Ga}_{1-x}\text{In}_x\text{N}_y\text{As}_{1-y-z}\text{Sb}_z$ in eV are:

$$\begin{aligned} E_N &= (1.65 + VB_{\text{GaInNAsSb}}^{\text{Max}} - VB_{\text{GaAs}}^{\text{Max}}) - 0.2z + a_N \text{Tr}(\varepsilon) \\ V_{MN} &= 2.7 - 0.7x + 1.0z + VB_{\text{GaInNAsSb}}^{\text{Max}} - VB_{\text{GaAs}}^{\text{Max}} \end{aligned} \quad (2.28)$$

with $a_N=-0.65\text{eV}$.

The eigenenergies of the 2x2 Hamiltonian of Equation 2.27 yield the dispersion relations:

$$E_{\pm}(k) = \frac{E_N + E_M(k) \pm \sqrt{(E_N - E_M(k))^2 + 4V_{MN}^2 y}}{2} \quad (2.29)$$

The electron effective mass of the lowest sub-band, after some algebra, is given by:

$$m_e^z = m_e^t = \frac{\hbar^2}{\left. \frac{\partial^2 E_-}{\partial k^2} \right|_{k=0}} = m_e^M \left(1 + \frac{E_M(0) - E_-(0)}{E_N - E_-(0)} \right) \quad (2.30)$$

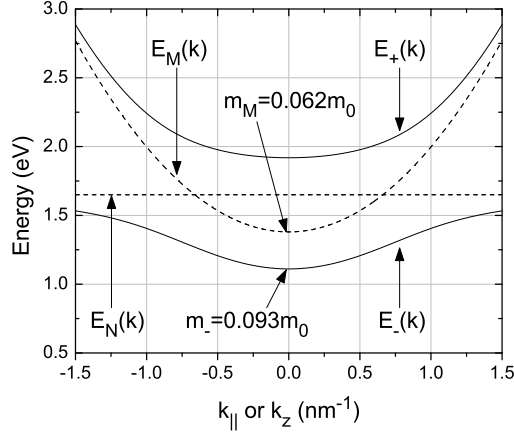


Figure 2.1: Band Anti-Crossing simulation of the dispersion relation for lattice matched $\text{Ga}_{0.96}\text{In}_{0.04}\text{N}_{0.02}\text{As}_{0.98}$.

where m_e^M is the electron effective mass of the unperturbed nitride-free semiconductor. Thus, the coupling to the localized nitrogen states can only increase the effective mass since the lowest eigenvalue $E_-(0)$ is always less than or equal to $E_M(0)$ and E_N by the variational principle.

Fig. 2.1 shows the influence of the localized nitrogen level on the conduction band dispersion relation for lattice matched $\text{Ga}_{0.96}\text{In}_{0.04}\text{N}_{0.02}\text{As}_{0.98}$. Here, energies are given relative to the valence band maximum of $\text{Ga}_{0.96}\text{In}_{0.04}\text{N}_{0.02}\text{As}_{0.98}$. Since the bands $E_M(k)$ and E_N repel, the conduction band splits into two bands and the bandgap is reduced by 270meV and effective mass is increased by 50% for the lower band.

Any temperature dependence of the two conduction sub-band energies or effective masses is due to $E_M(k)$, which varies according to Equation 2.24. The Luttinger parameters will be affected by the new conduction band wavefunctions since they depend on various $\mathbf{k} \cdot \mathbf{p}$ matrix elements between conduction and valence band states. However, this influence is usually neglected [15] and the linearly interpolated Luttinger parameters are used to find the valence band effective masses according to Equations 2.15 and 2.17.

Table 2.1: Binary alloy material parameters at 0K, except for the lattice constant, which is given at 300K.

Parameter at 0K	InN	InAs	InSb	GaN	GaAs	GaSb
E_g (eV)	0.78	0.417	0.235	3.299	1.519	0.812
α (meV/K)	0.245	0.276	0.32	0.593	0.5405	0.417
β (K)	624	93	170	600	204	140
$a(\text{\AA})$ at 300K	4.98	6.0583	6.4794	4.50	5.65325	6.0959
da/dT (10^{-5} $\text{\AA}/\text{K}$)	...	2.74	3.48	...	3.88	4.72
Δ (eV)	0.005	0.39	0.81	0.017	0.341	0.76
γ_1	3.72	20.0	34.8	2.70	6.98	13.4
γ_2	1.26	8.5	15.5	0.76	2.06	4.7
γ_3	1.63	9.2	16.5	1.11	2.93	6.0
E_p (eV)	17.2	21.5	23.3	25.0	28.8	27.0
F	-2.77	-2.9	-0.23	-0.95	-1.94	-1.63
VBO (eV)	-2.34	-0.59	0	-2.64	-0.8	-0.03
a_c (eV)	-2.65	-5.08	-6.94	-6.71	-7.17	-7.5
a_v (eV)	-0.7	-1.00	-0.36	-0.69	-1.16	-0.8
b (eV)	-1.2	-1.8	-2.0	-2.0	-2.0	-2.0
d (eV)	-9.3	-3.6	-4.7	-3.7	-4.8	-4.7
C_{11} (GPa)	187	83.29	68.47	293	122.1	88.42
C_{12} (GPa)	125	45.26	37.35	159	56.6	40.26
C_{44} (GPa)	86	39.59	31.11	155	60.0	43.22

2.3 Compositional Simulations of the GaInNAsSb Band Structure

The data for the binary alloys and ternary bowing parameters, taken from [15, 48], are listed in Tables 2.1 and 2.2. Typographical corrections to some of the parameters from [48] that were mentioned in the references section of [15] are included in the tables. The errata primarily pertain to the elastic stiffness tensor coefficients C_{ij} . Material parameters for GaInAsSb (nitride-free) and GaInNAsSb (nitride-containing)

Table 2.2: Non-zero bowing parameters for ternary alloys formed from Ga, In, N, As, and Sb.

Parameter	InAsSb	GaAsSb	InGaSb	InGaAs	InGaN
E_g (eV)	0.67	1.43	0.415	0.477	1.40
Δ (eV)	1.2	0.6	0.1	0.15	
E_p (eV)				-1.48	
F			-6.84	1.77	
VBO (eV)		-1.06		-0.38	
a_c (eV)				2.61	

were calculated using the techniques of Section 2.1 and the BAC model of Section 2.2 was then applied to determine the parameters for GaInNAsSb.

Fig. 2.2a shows the strained bandgap map of $\text{Ga}_{1-x}\text{In}_x\text{N}_y\text{As}_{1-y-z}\text{Sb}_z$ alloys on a GaAs substrate for 0-50% In. There are three families of curves corresponding to fixed Sb concentrations of 0% (Black), 2% (Red), and 4% (Green). Each family consists of a long thick line (sloping downward for **increasing** lattice constant) that describes the bandgap for compositions of $\text{Ga}_{1-x}\text{In}_x\text{As}_{1-z}\text{Sb}_z$ (nitride free) with endpoints $\text{GaAs}_{1-z}\text{Sb}_z$ and $\text{Ga}_{0.5}\text{In}_{0.5}\text{As}_{1-z}\text{Sb}_z$. The line for $\text{Ga}_{1-x}\text{In}_x\text{As}$ (Sb=0) is extra thick. The family also consists of a series of six shorter thin lines (sloping downward for **decreasing** lattice constant) that describes the bandgap of $\text{Ga}_{1-x}\text{In}_x\text{N}_y\text{As}_{1-y-z}\text{Sb}_z$ for fixed In concentrations ranging from 0 to 50% in 10% steps as the N concentration is increased continuously from 0 to 4%. The location of the barrier, $\text{GaN}_{0.025}\text{As}_{0.975}$, and quantum well, $\text{Ga}_{0.62}\text{In}_{0.38}\text{N}_{0.023}\text{As}_{0.95}\text{Sb}_{0.027}$, of the lasers to be discussed throughout this thesis are illustrated by a triangle and square, respectively. The calculated barrier bandgap (E-LH) is 1013meV and the QW bandgap (E-HH) is 805meV. In Section 3.3.4, we determine these bandgaps to be 1094meV and 815meV, respectively. The origin of the small 81meV discrepancy in the barrier bandgap may be related to annealing. Good agreement of the bandgaps for other material compositions reported

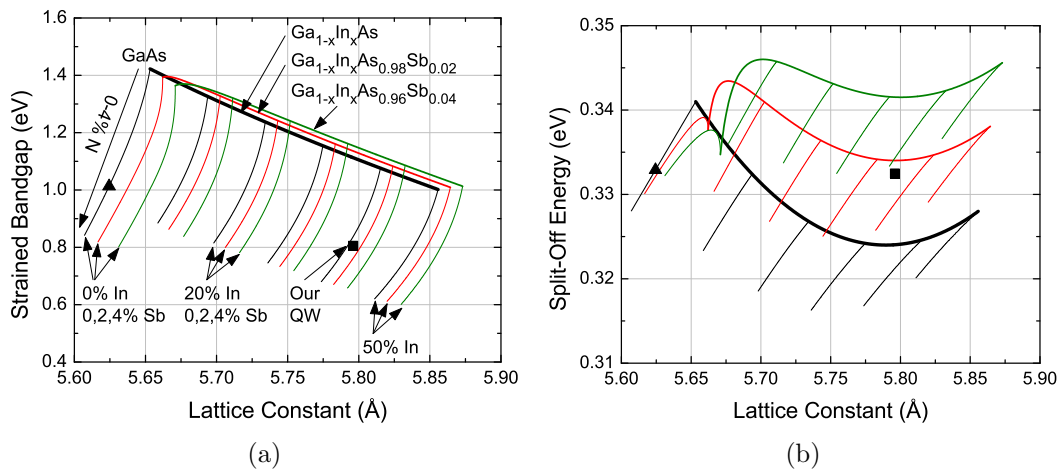


Figure 2.2: (Color) (a) Calculated strained bandgap map of GaInNAsSb alloys on a GaAs substrate. There are three families of curves corresponding to fixed Sb concentrations of 0% (Black), 2% (Red), and 4% (Green). Each family consists of a long thick line ($\text{Ga}_{1-x}\text{In}_x\text{As}$ is extra thick) that describes the bandgap for compositions of $\text{Ga}_{1-x}\text{In}_x\text{As}_{1-z}\text{Sb}_z$ (nitride free) and six shorter thin lines that describes the bandgap of $\text{Ga}_{1-x}\text{In}_x\text{N}_y\text{As}_{1-y-z}\text{Sb}_z$ for fixed In concentrations ranging from 0 to 50% in 10% steps as the N concentration is increased continuously from 0 to 4%. (b) Split-off energy, Δ , using the same legend of curve families.

in the literature is achieved since the dependence of model parameters on material composition was pre-determined experimentally.

With the same legend as Fig. 2.2a, the split-off energy, Δ , is shown in Fig. 2.2b. The direction of the lines in this figure and subsequent figures may be different, but the material composition dependence shown in these plots can be inferred in the same way, i.e. the lattice constant and along which line of the family of curves you move determine approximate material compositions. The extra thick line for $\text{Ga}_{1-x}\text{In}_x\text{As}$ and the triangle marker for the barriers at $\text{GaN}_{0.025}\text{As}_{0.975}$ help identify the family of curves. The value for Δ is roughly constant around 0.33eV and the odd dependence of Δ on In concentration is due to its large bowing parameter.

The conduction, heavy hole, light hole and split-off hole band offsets relative to a standard reference level (the valence band maximum of InSb) are plotted in Figs. 2.3a, 2.3b, 2.3c, and 2.3d, respectively. From the graphs, we calculate that electrons in the QW will have a barrier height of 87meV to the barriers and 393meV to the GaAs waveguide. For heavy holes, the offsets are 163meV and 224meV, respectively. For light holes, the barrier height is -8meV and the waveguide height is 95meV. We expect the light holes might have a type-II line-up in our laser structure. In Section 3.3.4, we determine these barrier heights to be 164meV and 408meV for electrons, 159meV and 201meV for heavy holes and -16meV and 70meV for light holes. Thus, excellent agreement is obtained for the band structure of our QW except for the previously mentioned 81meV difference in the barrier bandgap a 15-20meV difference in the valence band position of the barriers and QW relative to GaAs. The calculated valence band split, $E_{HH}-E_{LH}$, is 129meV in the quantum well and -42meV in the barriers.

The effective masses in the z-direction for the electron, heavy hole, light hole, and split-off hole are shown in Figs. 2.4a, 2.4b, 2.4c, and 2.4d, respectively. The electron effective mass in the z-direction strongly increases with N concentration as expected

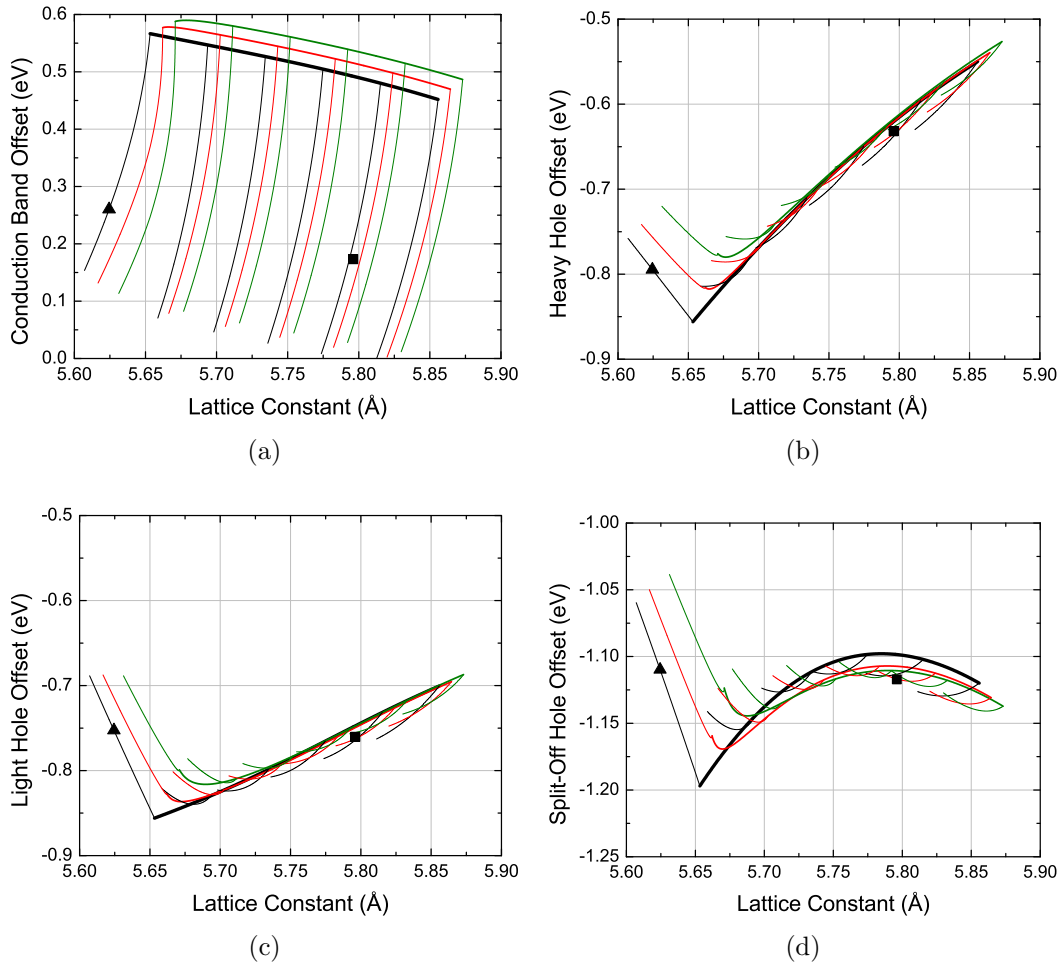


Figure 2.3: (Color) Band offsets for (a) electrons, (b) heavy holes, (c) light holes, and (d) split-off holes relative to valence band maximum of InSb.

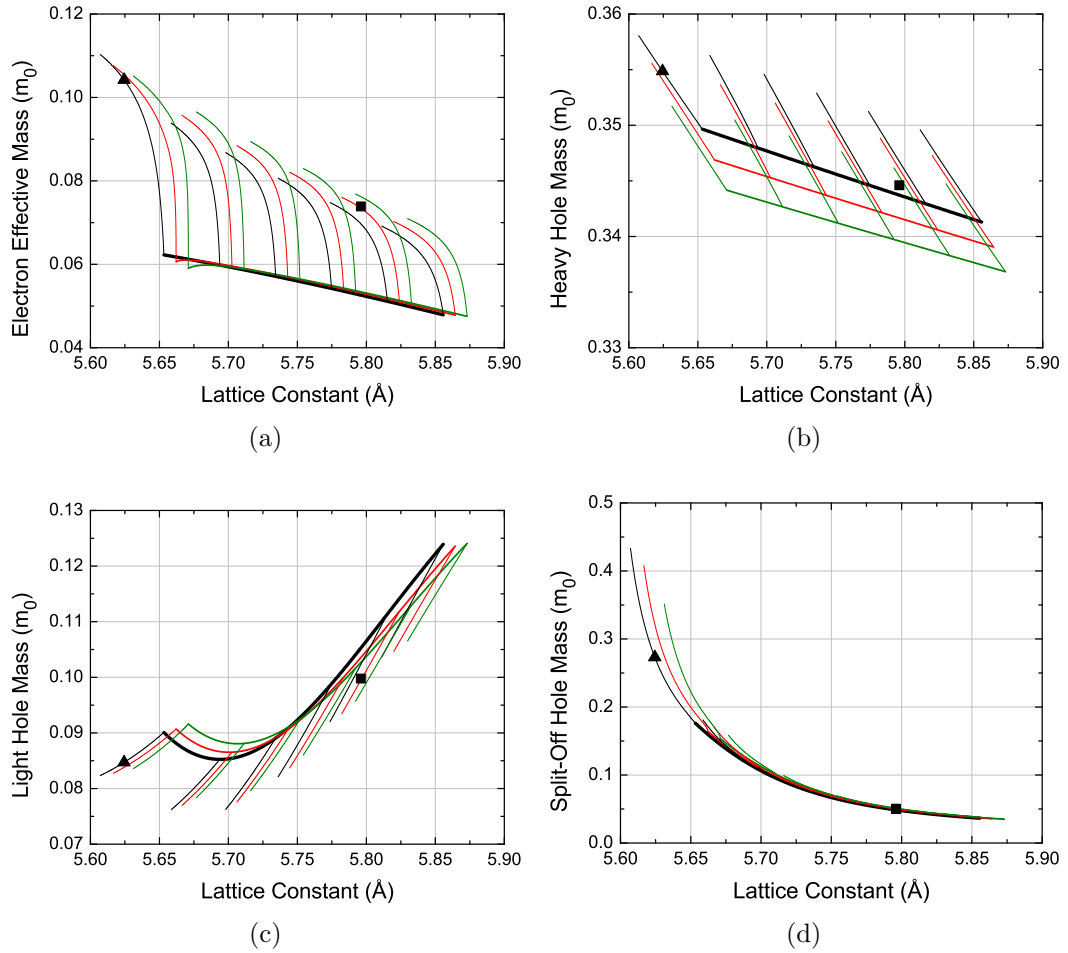


Figure 2.4: (Color) Effective masses in the z-direction for (a) electrons, (b) heavy holes, (c) light holes, and (d) split-off holes.

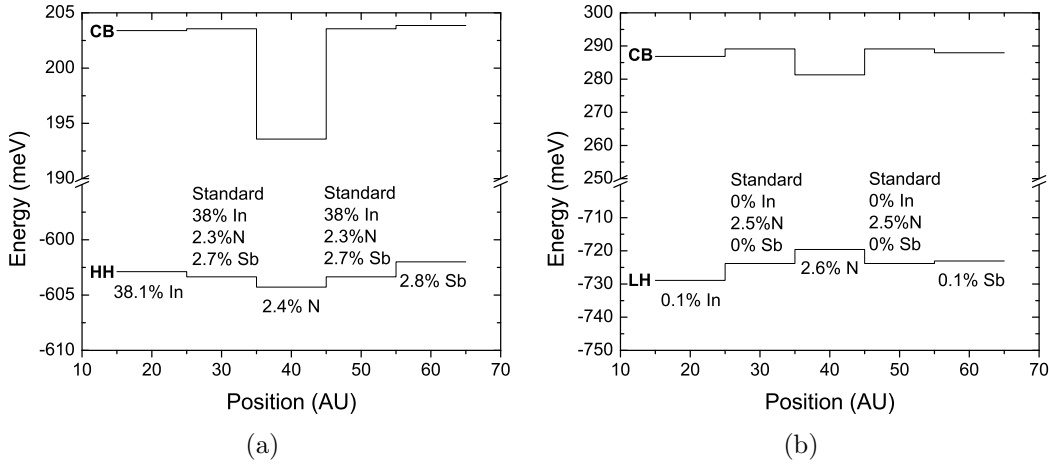


Figure 2.5: (a) QW band offsets for slight perturbations from the standard recipe of $\text{Ga}_{0.62}\text{In}_{0.38}\text{N}_{0.023}\text{As}_{0.95}\text{Sb}_{0.027}$. (b) Barrier band offsets for slight perturbations from the standard recipe of $\text{GaN}_{0.025}\text{As}_{0.975}$.

in the BAC model due to the interaction with the localized N level. The predicted electron mass for the barriers and QW are $0.104m_0$ and $0.074m_0$, respectively. The value for the QW effective mass is within two standard deviations of the experimentally determined value of $0.113 \pm 0.024m_0$ presented in Section 3.3.4. The heavy hole effective mass in the z-direction is relatively independent of composition and ranges from $0.33m_0$ to $0.36m_0$, while the light hole effective mass in the z-direction has an interesting dependence due to strain and valence band mixing effects. The split-off hole effective mass in the z-direction decreases very drastically with In concentration.

The shifts of the conduction band minimum and valence band maximum of the QW and barriers due to slight recipe changes are shown in Figs. 2.5a and 2.5b, respectively. For the QW, increasing the In concentration from 38 to 38.1% reduces the bandgap by 0.64meV (0.17meV lower conduction band, 0.47meV higher heavy hole band). Increasing the N concentration from 2.3 to 2.4% reduces the bandgap by 9.04meV (9.98meV lower conduction band, 0.94meV **lower** heavy hole band).

Overall, the heavy hole band gets pushed down since the strain energy exceeds the chemical valence band offset energy. Increasing the Sb concentration from 2.7 to 2.8% reduces the bandgap by 1.06meV (0.29meV **higher** conduction band, 1.35meV higher heavy hole band). This time, the conduction band gets pushed up due to strain. To summarize, the QW bandgap reduction is 6.4meV, 90.4meV, and 10.6meV per **percent** increase of In, N, and Sb, respectively, from their standard compositions.

In order to achieve optimal laser performance and temperature stability, electrons should be confined in as deep of a quantum well as possible due to their smaller effective mass. In almost all material systems, sacrificing valence band well depth for conduction band well depth is quite desirable. As mentioned previously, the added degree of freedom of the quinary GaInNAsSb alloy compared to a quaternary alloy, e.g. GaInNAs or InGaAsP, enables additional material engineering since the bandgap and lattice constant, i.e. strain, can be held constant while the offset ratio is independently tuned. Changing the In, N, and Sb concentrations by 2.19%, -0.037%, and -1%, respectively, will achieve this balance and push the conduction band down by 2.9meV. Unfortunately, this is a minuscule shift compared to the $\approx 100\text{-}400\text{meV}$ barrier and waveguide heights and it will be difficult to maintain good material quality with over 40% In. Further, it requires that the material compositions be independently and precisely controlled. However, we can achieve larger band offset shifts for a fixed bandgap if we allow for a change in the strain. For example, we can decide to reduce the QW strain from 2.5 to 2.0%, hold the bandgap constant, and push the conduction band down by 31meV by changing the In, N, and Sb concentrations by -8.50%, 0.48%, and 1%, respectively. The flexibility for such detailed device engineering in this quinary material system is unparalleled.

For the barriers, increasing the In concentration from 0 to 0.1% actually increases the bandgap by 2.86meV (2.24meV lower conduction band, 5.10meV **lower** light hole band) due to strain. Increasing the N concentration from 2.5 to 2.6% reduces

the bandgap by 12.03meV (7.80meV lower conduction band, 4.23meV higher light hole band). Increasing the Sb concentration from 0 to 0.1% reduces the bandgap by 1.91meV (1.16meV lower conduction band, 0.75meV higher light hole band). The effect of adding In, N, and Sb is much different for the barriers compared to the QW due to changes in the relative importance of strain, material bandgap reduction, and coupling to the N level. To summarize, the barrier bandgap reduction is -51meV, 120.3meV, and 19.1meV per **percent** increase of In, N, and Sb, respectively, from their standard compositions.

Beginning with $\text{GaN}_{0.025}\text{As}_{0.975}$, there is no adjustment combination of In, N, and Sb concentrations that can maintain a constant bandgap and strain since the In and Sb compositions are both zero initially and the needed adjustments are in opposite directions. If we allow a decrease in strain and keep the In concentration at zero, changing the N and Sb concentrations by -0.16% and 1%, respectively, will maintain a constant bandgap, while pushing the conduction band up by 0.8meV (i.e. increasing the electron QW depth) and decreasing the tensile strain from 0.51% to 0.47%. This is quite negligible and may not lead to any performance advantages if the material quality deteriorates due to these changes. To significantly improve electron confinement, the N concentration can be reduced and the In and Sb compositions kept at zero. This will increase the barrier bandgap and also improve hole confinement; however, strain compensation provided by the barriers will be diminished.

Chapter 3

Semiconductor Optical Processes: A Study Of Recombination, Gain, Band Structure, Efficiency, and Reliability

A large portion of this chapter has been accepted for publication in Journal of Applied Physics [74]. It can be found at <http://jap.aip.org/> after it is published. The dissertation author's role was to write the article and perform the measurement and data analysis of the lasers fabricated by the other authors of the paper.

In this chapter, we present temperature dependent measurements of the local Z-parameter, which reflects the dominant recombination processes. At room temperature, Z increases with current from 1.2 at low bias up to a threshold value, Z_{th} , of only 2.0, demonstrating the existence of significant amounts of monomolecular recombination. At elevated temperatures, Z_{th} rises above 2.5. We calculate the laser's band diagram and estimate 35meV of bandgap renormalization at threshold through polarization resolved measurements of exciton peaks in the absorption spectrum and inflection points of the absorption, spontaneous emission, and gain spectra. The small effective valence band barrier height of 115meV leads to hole leakage due to thermionic emission and carrier spillover into the barriers. This could explain the

increase in Z_{th} at elevated temperatures and decrease in internal quantum efficiency from 57% at 15 °C to 47% at 75 °C. We also analyze the spontaneous emission and gain spectra below and above threshold. The spontaneous emission clamped rather weakly at threshold, which also partially explains the low internal efficiency at room temperature. We present initial reliability measurements of over 100 hours at 10mW continuous wave (CW) power from a single facet. After 50 hours of life testing, the threshold current increased by 79% and the external differential quantum efficiency decreased by 39% of their respective pre-test values. By comparing the local Z-parameter versus current density curves before and after life testing, we have identified an increase in monomolecular recombination as the main source of degraded device performance.

3.1 Laser Growth and Fabrication

The edge-emitting separate confinement heterostructure ridge-waveguide lasers were grown on (100) n-type GaAs substrates by solid source molecular beam epitaxy (MBE) [75, 76]. Reactive nitrogen was supplied by an rf plasma cell operating in the inductively coupled mode with 300W of input power and a gas flow of 0.5 sccm. Deflection plates at the exit aperture, biased at -40V and ground, were used to minimize the ion flux upon the wafer [28, 77]. Nitrogen concentration was controlled directly by the group III growth rate [27, 40, 75, 76]. Antimony was supplied with an unvalved cracking cell, producing almost entirely monomeric antimony. The beam equivalent pressure was $\approx 1 \times 10^{-7}$ Torr and resulted in an antimony mole fraction of 2.7% in the quantum well. GaInNAsSb and GaNAs were grown at 455 °C with 20x and 15x arsenic overpressures, respectively. (Al)GaAs layers were grown at 20 °C above the oxide desorption temperature with 15x arsenic overpressure.

The single QW active region was a 78Å $\text{Ga}_{0.62}\text{In}_{0.38}\text{N}_{0.023}\text{As}_{0.95}\text{Sb}_{0.027}$ well surrounded on either side by 220Å strain compensating $\text{GaN}_{0.025}\text{As}_{0.975}$ barriers. The barriers were surrounded on either side by 2000Å of GaAs waveguide and 1.8μm of $\text{Al}_{0.33}\text{Ga}_{0.67}\text{As}$ cladding layers. The waveguide thickness corresponds to one optical wave, which approximately maximizes the overlap between the optical field and the quantum well according to the simulations discussed in Section 5.4. To minimize free carrier absorption losses, doping of the AlGaAs was kept low close to the GaAs/AlGaAs interface. The outer 9000Å of the n-type cladding layer was doped at $3 \times 10^{18} \text{cm}^{-3}$ and the inner 9000Å doped at $7 \times 10^{17} \text{cm}^{-3}$. The p-type cladding was a similar structure, with the inner 9000Å doped at $5 \times 10^{17} \text{cm}^{-3}$ and the outer 9000Å doped at $3 \times 10^{18} \text{cm}^{-3}$. The structure was capped with a 500Å thick, $\approx 1 \times 10^{20} \text{cm}^{-3}$ p-type GaAs contacting layer. After growth, the sample was *ex situ* annealed under a GaAs proximity cap at 800 °C for one minute in a nitrogen ambient. Ti/Pt/Au Ohmic contacts were patterned with evaporation and lift-off. Ridge widths of 5, 10, and 20μm were defined by a self-aligned dry etch to the top of the GaAs waveguide. The substrate was then thinned to $\approx 120 \mu\text{m}$ and Au/Ge/Ni/Au Ohmic contacts were evaporated onto the substrate side. A contact sinter was performed at 410 °C for one minute.

Devices of varying length were manually cleaved and soldered epi-side up onto a temperature controlled copper heat sink. See Appendices A and B for further details about device mounting. Unless otherwise specified, contact to the top p-metal was made at three locations along the device length with 24μm diameter Tungsten probe tips while contact to the n-metal was through the copper heat sink.

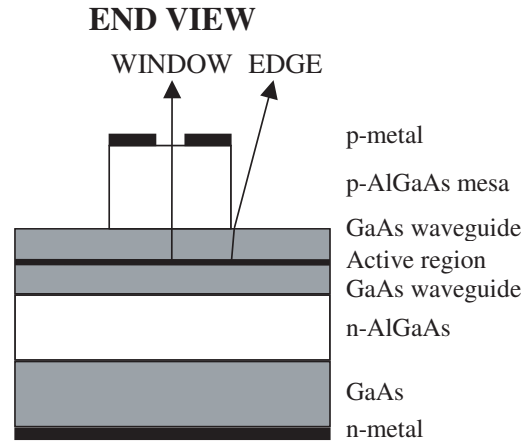


Figure 3.1: WINDOW and EDGE measurement configurations for TSE.

3.2 Spontaneous Emission

3.2.1 Measurement Techniques

A quick and useful method for studying carrier recombination and internal efficiency is measurement of the spontaneous emission spectrum below and above threshold. The vertically emitted, unamplified, true spontaneous emission (TSE) of the laser device was collimated using a lens with a moderate numerical aperture ($NA=0.31$). This limits the collection angle inside the active region to $<5^\circ$ due to refraction from the high index layers to air. The light was focused onto a multi-mode fiber for measurement with an optical spectrum analyzer (OSA). The TSE escaped the device structure vertically around the ridge waveguide metal edges in one setup, labeled EDGE in Fig. 3.1, and through a $5\mu\text{m} \times 10\mu\text{m}$ window that was etched in the top p-metal and slightly into the p-AlGaAs cladding layer using a focused ion beam (FIB) in another setup, labeled WINDOW also shown in Fig. 3.1. In WINDOW mode, some of the EDGE light will also be detected. Unless otherwise mentioned, data pertains

to lasers with a highly reflective (HR) coating ($R=98.7\%$) on one facet and as-cleaved ($R=30\%$) on the other.

By design, the polarization of the collected light in this vertical configuration is transverse electric (TE). Transverse magnetic (TM) can only be emitted in the quantum well (QW) plane. Since the GaInNAsSb quantum well is compressively strained on GaAs at $\approx 2.5\%$, the main interband transition is between the ground states of the electron and heavy hole ($E^1\text{-HH}^1$)_{QW}, which has non-zero transition matrix elements for TE polarization only. Therefore, a fixed fraction of all of the emission of the main transition was collected in this configuration. Since the GaNAs barriers are tensilely strained on GaAs at $\approx 0.5\%$, the lowest interband transition in the barriers is between the continuum of states of the electron and light hole ($E\text{-LH}$)_{Barrier}. Both TE and TM polarized emission exist in-plane, but only the TE portion of the main barrier transition is detected vertically. As we shall see in the absorption section, the compressive strain in the well coupled with the tensile strain in the barrier prevents the light holes from having quantized levels in the QW for our GaInNAsSb/GaNAs compositions. Instead, the QW acts as a small perturbation to the potential of the barrier. The light holes form a continuum, with a quasi-3D density of states since the total width of the barrier plus QW is 51.8nm. However, they may accumulate at the barrier/well interfaces because of the Coulomb attraction to the electrons in the QW.

The small collection angle of $<5^\circ$ produced low signal levels so the data was collected in CW and pulsed ($1\mu\text{s}$ width, 10% duty cycle) modes. Unfortunately, this leads to device heating of about 30°C in CW and 3°C in pulsed mode at $3\text{kA}/\text{cm}^2$. We will denote the stage and active region temperatures by T_s and T_a , respectively. The thermal resistance, R_T , of our devices has been extensively measured [27] and modeled in Section 5.2. For $20\mu\text{m}$ wide devices, the resistance in K/W is well modeled by $R_T=30.3/L$, where L is the device length in millimeters. Some measurements were

made in CW mode to increase the span of the spectra or to improve the accuracy of the applied current. Background subtraction was performed on all raw spectra to further improve measurement sensitivity.

The collection efficiency was wavelength dependent due to the chromatic aberration in the lenses and the wavelength dependence of refraction and Fresnel transmission arising from the dispersion of the refractive index of the active region. However, these effects are estimated to reduce the overall measurement accuracy by $<7\%$. OSA spectra, which measure power within a resolution bandwidth, $\text{ResBW}: P(\lambda) \cdot \text{ResBW}$, were converted to emission rates in photons per second per unit energy by dividing by $E^3 \cdot \text{ResBW}/(h \cdot c)$, where E is the photon energy, h is Planck's constant, and c is the speed of light.

3.2.2 Results and Discussion

The TSE-WINDOW spectra were measured on a $20\mu\text{m} \times 306\mu\text{m}$ device. The short device had high enough mirror loss that CW lasing was not observed. This allowed the application of large current densities in order to observe higher order transitions. However, the short length of the device led to a large thermal resistance of 96K/W . The spectra for 1, 2, and 3kA/cm^2 at $T_a \approx 50^\circ\text{C}$ ($T_s=45, 25, 5^\circ\text{C}$) are plotted in Fig. 3.2a, while the spectra for 3kA/cm^2 at $T_a=50, 90, \text{ and } 120^\circ\text{C}$ ($T_s=5, 45, 85^\circ\text{C}$) are displayed in Fig. 3.2b. A post-measurement, high-frequency, fast Fourier transform (FFT) smoothing filter was applied to the data with a bandwidth that was narrower than the OSA resolution bandwidth to further reduce background noise without sacrificing spectral features.

For comparison with other measurements to be presented in later sections, we will discuss the data for 2kA/cm^2 at $T_a \approx 35^\circ\text{C}$ (not shown in Fig. 3.2, but similar). The peaks at $863 \pm 2\text{meV}$, $942 \pm 3\text{meV}$, and $1022 \pm 7\text{meV}$ are attributed primarily to broad overlapping peaks of the dominant QW transitions from the two electron levels to

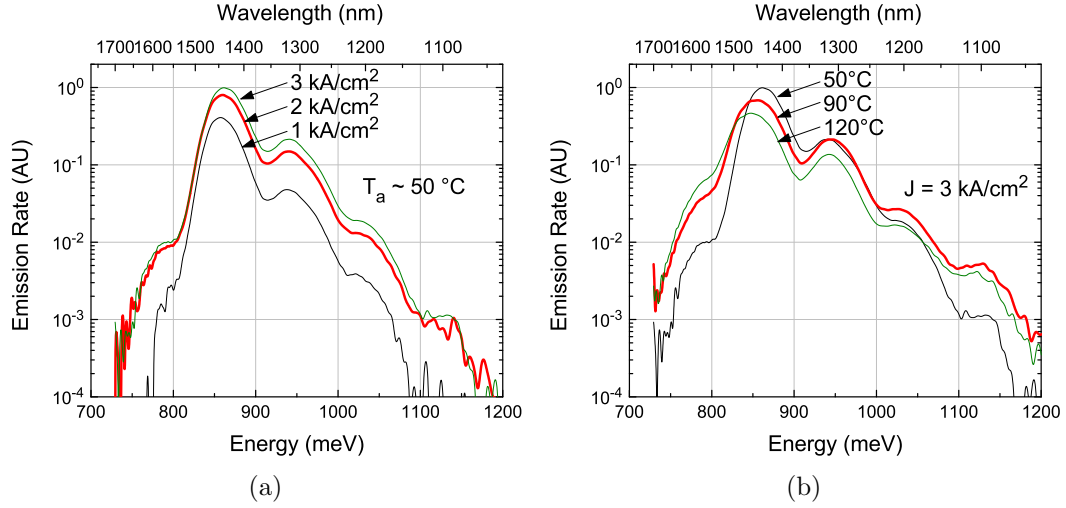


Figure 3.2: (Color) TSE-WINDOW spectra after background subtraction and FFT smoothing for a $20\mu\text{m} \times 306\mu\text{m}$ device. (a) is at $T_a \approx 50^\circ\text{C}$ for $1\text{kA}/\text{cm}^2$ (Black), $2\text{kA}/\text{cm}^2$ (Red), and $3\text{kA}/\text{cm}^2$ (Green) while (b) is at $3\text{kA}/\text{cm}^2$ for $T_a \approx 50^\circ\text{C}$ (Black), 90°C (Red), and 120°C (Green).

the three heavy hole levels: $E^1\text{-HH}^1$, $E^1\text{-HH}^3$, $E^2\text{-HH}^2$, while the peak at $1114 \pm 8\text{meV}$ is attributed to barrier emission, $(E\text{-LH})_{\text{Barrier}}$. From TM spectra, presented in the multi-section emission section, a small portion of the emission on the high energy side of the 942 and 1022meV peaks is due to the transition from electrons in the QW to the continuum of light hole states in the barrier: $E^1\text{-LH}_{\text{Barrier}}$ and $E^2\text{-LH}_{\text{Barrier}}$. Despite a weaker wavefunction overlap, these emission lines are stronger than the 1114meV barrier emission because the electron population is orders of magnitude larger in the QW than the barriers.

The shoulder near 800meV has its peak inside the high energy tail of the main transition. Krispin et. al. previously identified two electron traps in GaNAs caused by split interstitial defects on single As sites: $(\text{N-N})_{\text{As}}$ at $E_v + 800\text{meV}$ and $(\text{As-N})_{\text{As}}$ at $E_v + 1100\text{meV}$ [78]. Thus, one explanation of the sub-bandgap emission is a radiative transition from the $(\text{N-N})_{\text{As}}$ level. However, from new absorption and reliability data,

it is more likely that it corresponds to the exciton peak. Nevertheless, these barrier defects could still be present, but the recombination might be primarily non-radiative.

Thermal linewidth broadening causes the gain and absorption spectra to peak a few meV higher than the true transition edge. The spontaneous emission spectrum peaks $\approx 0.2-0.5k_B T$ even higher than this due to the E^2 density of photon states prefactor [79]. Nevertheless, the transition edge can be accurately determined as the inflection point in any of these three spectra. Since the occupation probability is a maximum at the unbroadened transition edge, convolution with a symmetric lineshape, e.g. Lorentzian, results in a maximal rate of increase at this edge.

Due to the bandgap reduction with temperature, the inflection point for the main QW peak redshifted, however, the shift was only 0.31meV/K (0.41nm/K) at 1kA/cm² compared to the 0.34meV/K (0.60nm/K) redshift of the lasing wavelength. The inflection point shift decreased to 0.23 and 0.20meV/K at 2 and 3kA/cm², respectively. Bandgap renormalization (BGR) is strong in strained devices [80] and is responsible for these differences. At fixed current density, the carrier density of the E^1 and HH^1 levels decreases with temperature due to increased occupation of the higher levels and an increase in carrier leakage and/or Auger recombination. Thus, at fixed current density, the BGR is less at higher temperatures leading to an underestimate in the bandgap redshift with temperature; this measurement artifact becomes more pronounced at higher carrier densities, where BGR is stronger. The peak energy redshifted even less than the inflection point: 0.24, 0.20, and 0.17meV/K at 1, 2, and 3kA/cm², respectively. The E^2 density of photon states prefactor is probably responsible for this additional difference since the value of $k_B T$ blueshifts 0.086meV/K.

The 942 and 1022meV peak locations remained unchanged with temperature. Thermal broadening and increased emission on the high-energy side of these peaks from the $E^1-LH_{Barrier}$ and $E^2-LH_{Barrier}$ transitions, respectively, obscured any signs of the bandgap redshift.

The integrated QW emission rate decreased as expected due to the T^{-1} dependence of the radiative coefficient, B [81]. However, comparing the spectra at 50 and 90 ° C of Fig. 3.2b, the emission rate for the 942, 1022 and 1114meV peaks increased with temperature because of the increase in occupancy of the higher QW levels and of thermionic emission of carriers from the QW into the barrier. Comparing 90 and 120 ° C of Fig. 3.2b, except for the 800meV peak, there was a general rate decrease for all of the transitions, probably due to an increase in leakage or Auger recombination. With increasing temperature, the emission rate for the 800meV peak appears to increase strongly and the emission energy appears to be unchanged. This is counter-intuitive for the behavior of an exciton peak, but since the exciton peak moves rigidly with the bandgap, which redshifts faster than the main QW TSE peak, the exciton peak emerges at high temperature. This led to an incorrect initial conclusion of increased emission at higher temperatures.

3.3 Multi-section Experiments

3.3.1 Measurement Techniques

To study gain and obtain polarization resolved spontaneous emission and absorption spectra, we applied an abbreviated version of the techniques of Thomson et. al. [82]. Two trenches, each $2\mu\text{m}$ wide, were etched using a FIB through the top metal of a $1575\mu\text{m}$ long device with as-cleaved ($R=30\%$) facets. The first two section lengths were $324\mu\text{m}$ long each while the third was $927\mu\text{m}$ long. On-axis amplified spontaneous emission (ASE) spectra were collected with a polarizer inserted between the collection and focusing lenses. The setup is shown in Fig. 3.3 along with the device section layout.

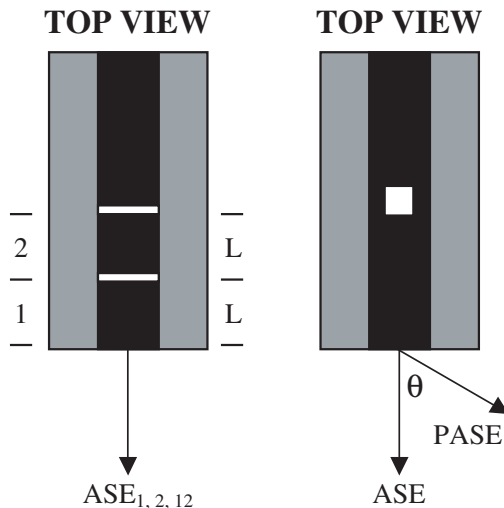


Figure 3.3: Multi-section gain measurement configuration on the left and (partial) amplified spontaneous emission with window configuration on the right.

We omitted the angled facet after the unpumped section to be able to examine whether the FIB trenches affected laser performance. Above the absorption edge of the unpumped section ($\alpha > 12.0 \text{ cm}^{-1}$), the collected ASE experiences a single pass amplification because the round trip loss through the unpumped section is high: $R_R \text{Exp}(-2\alpha L_R) \ll 1$, where $R_R = 30\%$ and $L_R = 927 \mu\text{m}$. This approximation was validated by the lack of Fabry-Pérot fringes at all measured currents. However, below the absorption edge, the internal loss of 7.5 cm^{-1} (presented later) might be insufficient to fully attenuate the reflected light, especially at high injection currents ($> 1.5 \text{ kA/cm}^2$). The correction for sub-bandgap spectra due to multi-pass amplification is small for the absorption and emission measurements, but can reach 10% for the gain measurement. In future experiments, the absorbing region could be made longer and the facet reflectivity reduced while still keeping the mirror loss constant. This should preserve the threshold and efficiency values when all sections are probed, but improve the measurement accuracy at higher current densities. In addition, part of the absorbing

region could be reverse biased to increase the sub-bandgap absorption due to the quantum confined Stark effect (QCSE), which quadratically redshifts the band edge transition energy as a function of the field. Care must be taken to ensure that the current injection of the pumped sections is not modified.

Electrical isolation of the sections is critical for high accuracy. The resistance between the metal contacts of the adjacent sections was measured to be 150Ω . This is much greater than the $3\text{-}4\Omega$ device series resistance, so good electrical isolation was obtained. The effects of any current spreading are expected to be negligible since the carrier diffusion lengths are much smaller than the section lengths. Separate current sources were used to bias the sections rather than using two probes in parallel, because unequal contact resistances could lead to unequal current distribution between the sections.

Extreme care was taken during etching the metal at the edges of the ridge waveguide by decreasing the ion beam strength and angling the beam at 45° to the metal surface, away from the ridge center, in order to minimize damage to the exposed parts of the AlGaAs p-cladding walls and GaAs waveguide underneath. The threshold and external efficiency with all three sections probed were only slightly degraded (4% and 7%, respectively) compared to devices without FIB trenches. It appears that the main effect of the FIB etch was to increase the waveguide scattering loss. The observed degradation of the threshold and efficiency is well accounted for if the internal loss is increased to 3.8cm^{-1} from a value of 3.0cm^{-1} obtained through a previous cavity length study [27] of the same wafer.

Polarization resolved absorption, net gain and TSE spectra were calculated, neglecting the sub-bandgap multi-pass correction, according to [82]:

$$\begin{aligned}\alpha &= -\frac{1}{L}Ln\left(\frac{ASE_2}{ASE_1}\right) \\ \Gamma g - \alpha_i &= \frac{1}{L}Ln\left(\frac{ASE_{12}}{ASE_1} - 1\right) \\ TSE &\propto \frac{1}{L}Ln\left(\frac{ASE_{12}}{ASE_1} - 1\right)\frac{ASE_1^2}{ASE_{12}-2ASE_1}\end{aligned}\quad (3.1)$$

where ASE_1 , ASE_2 , and ASE_{12} are the ASE spectra when pumping section 1 only, section 2 only, and both sections, respectively, and L is the length of each section. The measurements were performed in CW mode to obtain a wider spectrum with high signal-to-noise ratio, but at the cost of device heating; $T_s=15^\circ\text{C}$ and T_a increased from T_s at low bias to 35°C at $2\text{kA}/\text{cm}^2$.

3.3.2 Spontaneous Emission and Gain Results

Figs. 3.4a and 3.4b show the normalized TE and TM TSE spectra at various current densities. From these spectra, we definitively identify two transitions, located at 853meV and 954meV for $2\text{kA}/\text{cm}^2$ as E-HH and E-LH in nature. The two main peaks of the device used in Fig. 3.2a were at 865 and 940meV for $2\text{kA}/\text{cm}^2$ ($T_a=35^\circ\text{C}$). However, Fig. 3.4b shows that at 954meV , the TM peak has only 10% of the amplitude of the TE spectrum in Fig. 3.4a and so the 940meV peak must be mostly due to a TE transition. This transition is obscured by the high energy tail of the 853meV peak in Fig. 3.4a.

Below the bandgap energy, the net gain spectrum asymptotes to the internal loss. We obtained a value for the internal loss of $7.5\pm 0.9\text{cm}^{-1}$ for the TE mode. This value is slightly inconsistent with the estimate of 3.8cm^{-1} based on how the threshold and efficiency for this device compared to the previous cavity length study. Below 900meV , the ASE for the TM mode was so weak that the 1000:1 extinction ratio

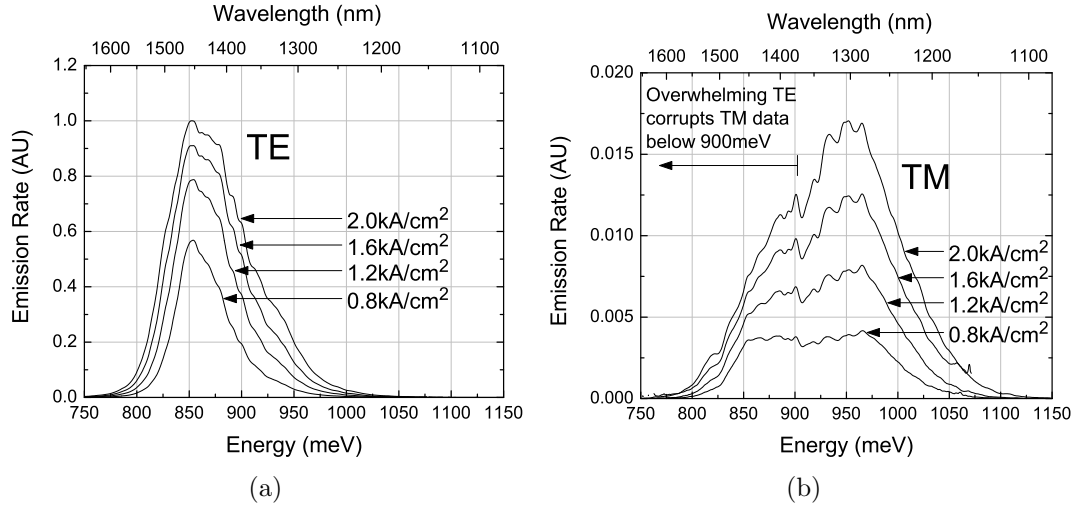


Figure 3.4: Normalized TE and TM spontaneous emission spectra at $T_s=15^\circ\text{C}$ for 0.8, 1.2, 1.6, and 2.0kA/cm^2 . The TE peak is over 50x larger than the TM peak; below 900meV, this ratio increases and the polarizer was unable to fully block the overwhelming TE signal. The ripples are due to an interference effect caused by partial beam clipping.

of the polarizer was insufficient to adequately suppress the overwhelming TE signal. As a result, the data was corrupted by the absorption signal of the TE mode, which pulled down the measured TM gain curve for the low energy region. Thus, we cut the TM data below 900meV, which prevented an accurate estimate of the internal loss for the TM mode. Nevertheless, extrapolating the TM gain spectrum to lower energies, we obtain an internal loss of the TM mode of $8\pm 3\text{cm}^{-1}$.

In calculating the material gain, which is plotted in Figs. 3.5a and 3.5b, we assumed the same internal loss of 7.5cm^{-1} for both modes and a confinement factor, Γ , of 1.4% for TE but 9.2% for TM since the light holes are spread throughout the barriers and QW due to the weak type-II alignment. The TE gain is peaked near 828meV or 1500nm. The peak is almost constant and does not shift to higher energies with current due to BGR and device heating. The TM spectra show absorptive loss at all measured currents due to the low occupancy of the light hole bands. The peak

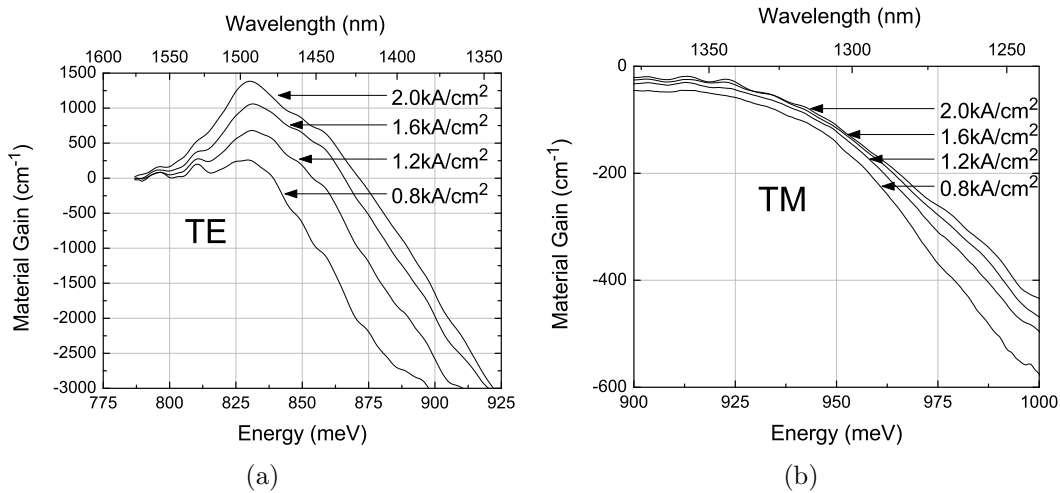


Figure 3.5: Material gain spectra at $T_s=15^\circ\text{C}$ for 0.8, 1.2, 1.6, and 2.0 kA/cm^2 . The TE gain peak remains near 828 meV or 1500 nm rather than shifting to higher energies with current due to BGR and device heating. The TM spectra show absorptive loss at all measured currents due to the low occupancy of the light hole bands.

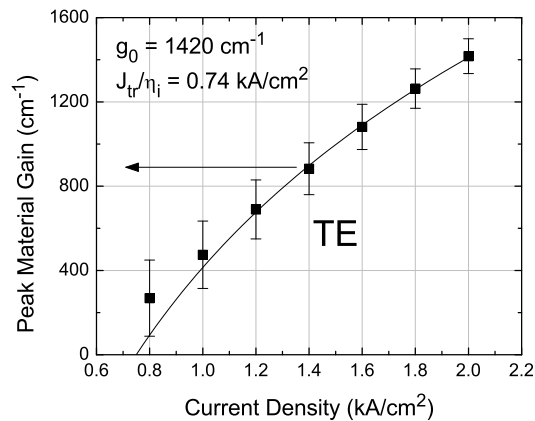


Figure 3.6: Peak TE material gain versus current density. The logarithmic fit to the TE mode's g - J curve was $g=1420 \cdot \text{Ln}(J/0.74)$ where g is in cm^{-1} and J is in kA/cm^2 .

TE material gain is plotted in Fig. 3.6. Above transparency, the fit for the TE peak gain to the empirical formula $g=g_0\text{Ln}(\eta_i J/J_{tr})$, where g_0 is the gain coefficient, η_i is the internal efficiency, and J_{tr} is the transparency current density, is good and we find $g_0=1420\text{cm}^{-1}$ and $J_{tr}=0.37\text{kA/cm}^2$ since $\eta_i=0.49$. Both parameters are slightly different than the values of 1871cm^{-1} and 0.48kA/cm^2 obtained through the pulsed mode cavity length study [27] because of device heating.

3.3.3 Absorption Measurements

In the absorption measurement, the ASE of the second section served as an optical pump source for the unbiased first section [82]. Due to BGR with carrier density, the emission wavelength of the second section was redshifted and provided sufficient optical intensity for an absorption measurement well below the unpumped bandgap. The modal absorption spectrum for the unpumped section for $T_a \approx T_s=35^\circ\text{C}$ is shown in Fig. 3.7. The strong wavelength dependence of the absorption and emission produced ASE spectra with over 40dB amplitude contrast. To improve the measurement accuracy for the weaker part of the spectrum, overlapping spectra were taken with different OSA settings and the data sets were joined at 1300nm (954meV). The TM mode spectra, having a smaller amplitude contrast, overlapped cleanly, but the TE mode spectra showed a 6cm^{-1} discontinuity, consistent with an OSA measurement error of 0.8dB.

From the low energy tail of Fig. 3.7, the internal loss was 7.0cm^{-1} for both the TE and TM modes. Taking into account the multi-pass correction, the exact internal loss was slightly higher, $7.6\pm 0.3\text{cm}^{-1}$. BGR pushed the main emission peak of the TE spectrum to a lower energy. As a fortuitous result, its distance to the unpumped TM absorption edge increased and the accidental collection of the overwhelming TE signal was significantly reduced. Without this systematic error, the internal loss for the TM mode was more accurately determined. Processes such as intervalence

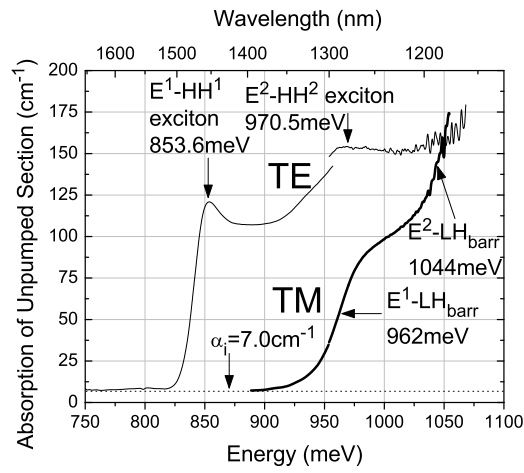


Figure 3.7: Modal absorption spectra of the unpumped section for $T_a \approx T_s = 35^\circ \text{C}$. Data was collected in two sweeps and joined at 1300nm. The low energy tail for both spectra asymptote to the internal loss, $\alpha_i = 7.0 \text{cm}^{-1}$. The TE spectrum has exciton peaks for the $E^1\text{-HH}^1$ and $E^2\text{-HH}^2$ transitions at 853.6 and 970.5meV, respectively. The TM spectrum has no visible exciton peaks. Transition energies for the $E^1\text{-LH}_{Barrier}$ and $E^2\text{-LH}_{Barrier}$ of 962 and 1044meV were found using the inflection points.

band absorption (IVBA) and free carrier absorption (FCA) in the QW and barriers are absent since the section is unpumped and these regions are not intentionally doped. Thus, the internal loss of 7.6cm^{-1} represents the waveguide scattering loss and absorptive loss of the doped cladding layers; the actual internal loss may be higher during laser operation.

3.3.4 Band Structure

Band offsets, bandgaps and effective masses can be calculated through measurements of the inflection points in the absorption and TSE spectra. In some cases, greater accuracy was achieved using the energy difference between peak locations. The determination method of various energy levels and their uncertainties are described in Table 3.1. The TE absorption has an exciton peak for the $E^1\text{-HH}^1$ transition at 853.6meV with a full width half maximum (FWHM) of 14.3meV and a faint exciton peak for the $E^2\text{-HH}^2$ transition at 970.5meV . For the finite QW with 7.8nm thickness, the exciton binding energy is estimated to be significant: $E_b^{Exciton} \approx 16\text{meV}$ due to the large predicted effective mass in the Band Anti-Crossing model [65]. No exciton peak is visible for the $E^1\text{-HH}^3$ transition because the transition is only weakly allowed and may be obscured by the absorption edge of the $E^1\text{-LH}_{Barrier}$ transition. The TM absorption spectrum has no visible exciton peaks because the light hole exciton reduced mass is 50% smaller and the light holes are unconfined and therefore form more of a 3D-like exciton. Both differences lead to a smaller exciton binding energy. The peak would be easily smeared into the main band to band transition.

From high sensitivity TSE data, we were able to observe an extremely weak peak at 1158meV beyond the 1114meV peak described in Fig. 3.2. We believe these correspond to the $(E\text{-HH})_{Barrier}$ and $(E\text{-LH})_{Barrier}$ transitions, respectively. Since the carrier density is small in the barriers, we can assume negligible BGR for the barriers and consider them unpumped. Also, due to the proximity of the two transitions, we

Table 3.1: Energy level separations and their method of determination for our GaInNAsSb SQW inside GaNAs barriers

Index	Transition	Energy (meV)	Determination Method
1	$(E^1 - HH^1)_{Exciton}^{Peak}$	853.6±0.7	TE Absorption Exciton Peak
2	$(E^2 - HH^2)_{Exciton}^{Peak}$	970.5±1.8	TE Absorption Exciton Peak
3	$(E^2 - E^1) + (HH^1 - HH^2)$	117±2	(2) minus (1)
4	$E^1 - LH_{Barrier}$	962±2	TM Absorption Inflection Point
5	$E^2 - LH_{Barrier}$	1044±4	TM Absorption Inflection Point
6	$E^2 - E^1$	82±4	(5) minus (4)
7	$HH^1 - HH^2$	35±5	(3) minus (6)
8	$E_g^{Barrier} = (E - LH)_{Barrier}$	1094±5	TSE Inflection Point
9	$E_{Barrier} - E^1$	132±5	(8) minus (4)
10	$(E - HH)_{Barrier}^{Peak}$	1158±10	TSE Peak
11	$(E - LH)_{Barrier}^{Peak}$	1114±8	TSE Peak
12	$(LH - HH)_{Barrier}$	44±13	(10) minus (11)
13	$(LH - HH)_{Barrier}$	42	Theory – Vegard’s Law
14	$(E - HH)_{Barrier}$	1138±14	(8) plus (12)
15	$(E^1 - HH^1)_{Exciton}$	843±3	TE Absorption Inflection Point
16	$E_b^{Exciton}$	16±5	Theory
17	$E^1 - HH^1$	859±6	(15) plus (16)
18	$E^2 - HH^2$	976±6	(3) plus (17)
19	$HH^1 - LH_{Barrier}$	103±6	(4) minus (17)
20	$HH^1 - HH_{Barrier}$	147±14	(12) plus (19)
21	$(HH - LH)_{QW}$	131	Theory – Vegard’s Law

can assume that the TSE peaks are the same distance from their respective transition edge. Thus, we obtain the strain-induced valence band splitting, $(\text{LH-HH})_{\text{Barrier}}$, of 44meV. Using a linear interpolation (Vegard's law) for the deformation potentials and lattice constants of zinc-blende GaN [15] and GaAs [48], we calculate a strain induced splitting of 42meV for $(\text{HH-LH})_{\text{Barrier}}$, which agrees quite well with the measured value. There have been reports (at 80K) of enhanced valence band splitting in GaNAs/GaAs [83, 84] attributed to non-linear behavior in the deformation potential, b. However, at room temperature, the measured valence band splitting of $\approx 42\text{meV}$ for 2.3% nitrogen in [83] is consistent with our results and interpolation. Lacking any reports in the literature for the quinary GaInNAsSb QW, we can only give a rough estimate for the $(\text{HH-LH})_{\text{QW}}$ strain splitting of 131meV using a linear interpolation of the data for the six binary alloys: GaAs, GaN, GaSb, InAs, InN, and InSb found in [15, 48].

With various level separations experimentally determined, specifically $E_{\text{Barrier}}-E^1$, E^2-E^1 , $E^1-\text{HH}^1$, HH^1-HH^2 , and $\text{HH}^1-\text{HH}_{\text{Barrier}}$ (9, 6, 17, 7, and 20 of Table 3.1), we minimized the weighted least squares fit to finite quantum well theory. The QCSE due to the built-in field of 35kV/cm produces less than a 2meV shift for any of the energy levels. This is small compared to the measurement error and so the QCSE was neglected in these calculations. The barrier effective masses were taken to be $m_e^{\text{Barrier}}=0.072m_0$ [69] and $m_{hh}^{\text{Barrier}}=0.355m_0$ using linear interpolation for the Luttinger parameters in [15]. The quantum well thickness was $L_z=7.8\text{nm}$. The adjustable parameters apply to the QW and were the bandgap E_g^{QW} , the effective masses m_e^{QW} and m_{hh}^{QW} , and the conduction band offset ratio $Q_c^{\text{QW}}=\Delta E_c/\Delta E_g$. The four parameter fit may be rearranged into four non-linear coupled equations that can be solved exactly as follows: given m_e^{Barrier} , m_{hh}^{Barrier} , and L_z , there are unique solutions for (a) m_e^{QW} given $E_{\text{Barrier}}-E^1$ and E^2-E^1 and for (b) m_{hh}^{QW} given $\text{HH}^1-\text{HH}_{\text{Barrier}}$ and HH^1-HH^2 . E_g^{QW} is determined using $E^1-\text{HH}^1$ and the confinement energies calculated

while solving (a) and (b). Finally, Q_c is obtained using the confinement energies and $E_{Barrier}-E^1$ and $HH^1-HH_{Barrier}$. Thus, each parameter can be obtained analytically with high accuracy; however, the least squares fit is preferable, especially if additional level separation data exist, e.g. HH^1-HH^3 , or if the data is to be weighted according to measurement uncertainty.

Table 3.2 summarizes the free and derived fit parameters. From the fit, we find $Q_c^{QW}=50.8\pm 2.1\%$, $E_g^{QW}=815\pm 7\text{meV}$, $m_e^{QW}=0.113\pm 0.024m_0$, and $m_{hh}^{QW}=0.35\pm 0.09m_0$. We also determine the band offsets to be $\Delta E_c=164\pm 5\text{meV}$ and $\Delta E_v^{HH}=159\pm 12\text{meV}$. All of these parameters include the effects of strain and would be significantly different for lattice-matched material. With the barrier heights and effective masses, the flat-band thermionic emission lifetimes for electrons and heavy holes into the barriers are 28 and 40ps, respectively, using the formulas in [85]. However, the effective valence band barrier height, $\Delta E_v^{Effective}$, is only $115\pm 6\text{meV}$ because of light holes. With the smaller effective barrier height, the thermionic emission lifetimes for holes could be less than 7ps if there is efficient scattering from the heavy to light hole bands at the QW interfaces. Also, assuming that the estimated $(HH-LH)_{QW}$ strain splitting of 131meV is correct, then the LH is unconfined in the QW and is type-II by 16meV. At elevated temperatures or currents, there will be a significant concentration of holes in the barriers. The fit predicts two electron and three heavy hole levels with confinement energies of 32 and 114meV for electrons and 12, 47, and 102meV for heavy holes and that there might be a fourth heavy hole level about 1meV from the heavy hole barrier. This possible level will be ignored because of its weak confinement and proximity in energy to the barrier. It is already deep within the continuum of light hole barrier states.

Aside from uncertainty in the measured level separations, errors in quantum well thickness and barrier effective masses are the main sources of uncertainty in the fit parameters. All three uncertainties were included in calculating the error estimates

Table 3.2: Derived band diagram parameters and their method of determination. Note that all values include strain effects.

Index	Parameter (Units)	Value	Determination Method
22	$m_e^{Barrier}(m_0)$	0.072 ± 0.030	Ref. [69]
23	$m_{hh}^{Barrier}(m_0)$	0.355 ± 0.030	Ref. [15] – Vegard’s Law
24	$L_z(nm)$	7.8 ± 0.5	HR-XRD
25	$Q_c^{QW}(\%)$	50.8 ± 2.1	Least Squares Fit – Free Parameter
26	$E_g^{QW}(meV)$	815 ± 7	Least Squares Fit – Free Parameter
27	$m_e^{QW}(m_0)$	0.113 ± 0.024	Least Squares Fit – Free Parameter
28	$m_{hh}^{QW}(m_0)$	0.35 ± 0.09	Least Squares Fit – Free Parameter
29	$E^1 - E_c(meV)$	32 ± 2	Least Squares Fit
30	$E^2 - E_c(meV)$	114 ± 6	Least Squares Fit
31	$E_v - HH^1(meV)$	12 ± 2	Least Squares Fit
32	$E_v - HH^2(meV)$	47 ± 7	Least Squares Fit
33	$E_v - HH^3(meV)$	102 ± 14	Least Squares Fit
34	$E_v - HH^4(meV)$	158 ± 12	Least Squares Fit
35	$\Delta E_c(meV)$	164 ± 5	Multiple: e.g. (9) plus (29)
36	$\Delta E_v^{HH}(meV)$	159 ± 12	Multiple: e.g. (20) plus (31)
37	$\Delta E_v^{Effective}(meV)$	115 ± 6	Multiple: e.g. (19) plus (31)
38	$E_g^{GaAs}(meV)$	1424	Ref. [48]
39	$Q_c^{GaNAs/GaAs}(\%)$	74 ± 5	Ref. [69]
40	$\Delta E_c^{GaNAs/GaAs}(meV)$	244 ± 17	(8), (38), and (39)
41	$m_{so}^{QW}(m_0)$	0.12	Refs. [15, 48] – Vegard’s Law
42	$\Delta_{so}^{QW}(meV)$	360	Refs. [15, 48] – Vegard’s Law
43	$E_{Trap}^{(N-N)As} - E_v^{GaNAs}(meV)$	830	Ref. [78] and $Z_0 \approx 1.3$
44	$E_{Trap}^{(As-N)As} - E_v^{GaNAs}(meV)$	1100	Ref. [78]

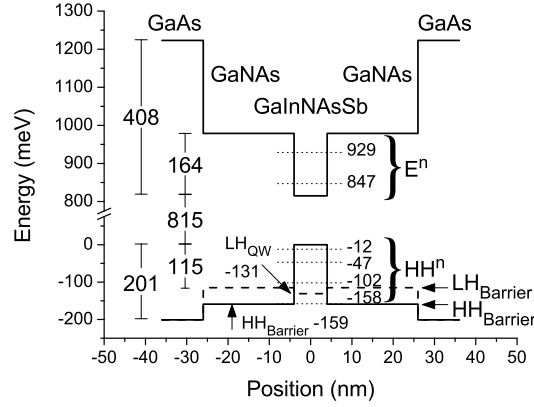


Figure 3.8: Flat-band diagram with confinement energies for our 800 ° C annealed, unpumped, 7.8nm $\text{Ga}_{0.62}\text{In}_{0.38}\text{N}_{0.023}\text{As}_{0.950}\text{Sb}_{0.027}$ SQW inside of 22nm $\text{GaN}_{0.025}\text{As}_{0.975}$ barriers embedded in a GaAs waveguide at $T_a=35^\circ\text{C}$. Energies, in units of meV, are relative to the HH QW valence band maximum. The QW is type-I for the HH band, but type-II for the LH band. There are two electron and three HH confined levels. A fourth, weakly confined, HH level is 1meV from the HH barrier.

of the fit and derived parameters. The latter two primarily affect the effective masses while the former obviously affects all parameters. Some of the derived parameters, most notably the band offsets, can be calculated from the data and fit parameters in multiple ways; using the level separation data and calculated confinement energies instead of (or in addition to) Q_c and the bandgaps can significantly reduce their uncertainties. The overall accuracy of the absorption/TSE technique can be significantly improved by performing a quantum well thickness study using GaAs barriers, whose parameters are more accurately known.

The flat-band diagram at $T_a=35^\circ\text{C}$ for our 7.8nm $\text{Ga}_{0.62}\text{In}_{0.38}\text{N}_{0.023}\text{As}_{0.950}\text{Sb}_{0.027}$ SQW inside 22nm $\text{GaN}_{0.025}\text{As}_{0.975}$ barriers embedded in a GaAs waveguide is shown in Fig. 3.8. Energies, in units of meV, are relative to the quantum well heavy hole valence band maximum. The offsets for GaNAs to GaAs of $\Delta E_c=244\text{meV}$ and $\Delta E_v^{LH}=86\text{meV}$ were approximated using the formulas in [69] to calculate $Q_c^{Barrier}=74\%$, but using

our data for $(E-LH)_{Barrier}=1094\text{meV}$ which is blueshifted by 68meV compared to [69], presumably due to differences in growth and because our sample was annealed.

The GaInNAsSb bandgap, offsets, and effective masses obtained here show excellent agreement with photoreflectance (PR) measurements at room temperature of an unannealed sample grown under the same conditions [86] after accounting for the annealing blueshift. Photoreflectance determined $E_g^{QW}=783\text{meV}$, $m_e=0.12m_0$, $\Delta E_c=144\text{meV}$, and $\Delta E_v^{HH}=127\text{meV}$. Comparing the two measurements, the QW and barrier bandgaps are blueshifted by 32 and 84meV , respectively. Given the measurement uncertainty and separate growths, it is unclear whether the barrier heights increase with annealing.

Absorption measurements were also made for $T_a \approx T_s=15$ and 65°C . Other than a miniscule decrease in the exciton absorption strength, all of the features in the TE and TM absorption curves overlap exactly when the spectra are redshifted 0.36meV/K . Since BGR is nonexistent in the unpumped section, we conclude that 0.36meV/K is the true value for the bandgap redshift with temperature.

3.3.5 Bandgap Renormalization

By comparing the TSE and gain spectra inflection points in Figs. 3.4a and 3.5a of 824 ± 3 and $822\pm 4\text{meV}$ to the unpumped $E^1\text{-HH}^1$ transition energy of $859\pm 6\text{eV}$, we find a bandgap renormalization of $36\pm 7\text{meV}$ for $J=2.0\text{kA/cm}^2$ and $T_a=35^\circ\text{C}$. BGR is a substantial effect, responsible for redshifting the lasing wavelength over 60nm . Unfortunately, this implies that as the threshold carrier density is reduced through growth and processing improvements, the GaInNAs(Sb) compositions will need to be readjusted and growth conditions reoptimized to maintain long wavelength operation.

From the zero crossing of the material gain curves in Fig. 3.5a, we determined the quasi-Fermi level separation for current densities above transparency, shown as the upper curve in Fig. 3.9. At 2.0kA/cm^2 , the quasi-Fermi level separation was 871meV .

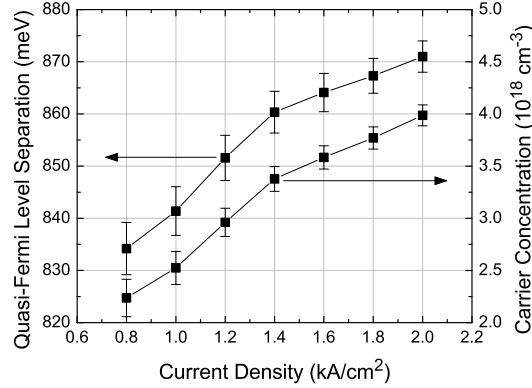


Figure 3.9: Quasi-Fermi level separation (upper curve) and carrier concentration (lower curve) versus current density. The lines serve as guides for the eyes.

Thus, the carrier density was $n=3.99 \times 10^{18} \text{cm}^{-3}$ or $n_{\text{surface}}=3.11 \times 10^{12} \text{cm}^{-2}$, using the inflection data for $E^1\text{-HH}^1=823 \text{meV}$. BGR scales roughly as $c \cdot n_{\text{surface}}^{1/3}$ for a QW structure, where c is a constant of proportionality. Thus, $c=25 \text{meV}/(10^{12} \text{cm}^{-2})^{1/3}$ which is slightly smaller than the values given in [87] for a GaAs/AlGaAs QW. With all three sections pumped, the device lased at $J_{th}=1.6 \text{kA/cm}^2$ ($n_{th} \approx 3.6 \times 10^{18} \text{cm}^{-3}$) and $T_a=35^\circ \text{C}$; thus, we calculate $35 \pm 7 \text{meV}$ bandgap renormalization at threshold. We were unsuccessful in using the crossing of the TE and TM net modal gain curves to verify the quasi-Fermi level separations as described in [82]. As mentioned previously, the slight presence of the TE signal was enough to affect the TM curve for energies below 900meV .

3.3.6 Carrier Density

Invoking charge neutrality, neglecting the QCSE, accounting for device heating and BGR, and using the band structure of Fig. 3.8 and measured quasi-Fermi level separations, we calculated the dependence of carrier concentration on applied current density in the lower curve of Fig. 3.9. Typically, BGR is neglected and the bandgap

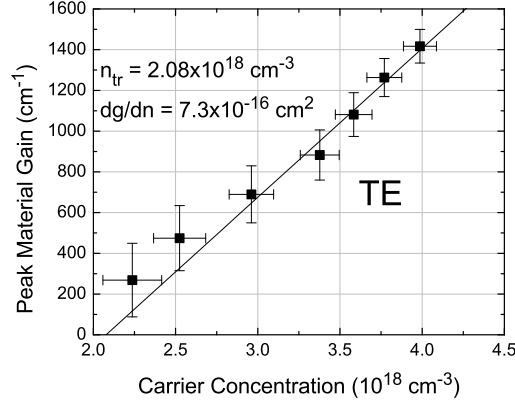


Figure 3.10: Peak TE gain versus carrier concentration and its linear fit. The differential gain was $7.3 \times 10^{-16} \text{ cm}^2$ and the transparency concentration was $2.08 \times 10^{18} \text{ cm}^{-3}$.

is assumed to be constant and equal to the lasing energy for all biases when calculating the carrier concentration versus current using quasi-Fermi level separation data. However, the increase in renormalization from transparency to 2.0 kA/cm^2 is almost 20% as large as the increase in quasi-Fermi level separation. Neglecting BGR leads to a 10% overestimate of the carrier concentrations at transparency. Even when BGR is included, there still remain some uncertainties in the n-J curve because the exact distribution of the BGR energy is difficult to calculate. For simplicity, we assumed a 50/50 split of the BGR energy between conduction and valence bands and that each confined level experiences an equal renormalization.

The material gain is plotted versus carrier density in Fig. 3.10. The gain fits well to a linear relationship having a differential gain of $dg/dn = 7.3 \times 10^{-16} \text{ cm}^2$ and a transparency of $n_{tr} = 2.08 \times 10^{18} \text{ cm}^{-3}$. A logarithmic relationship also works well for the g-n curve due to the limited range of measured carrier densities. The fitted transparency carrier concentration agrees excellently with a band structure calculation of $n_{tr} = 2.09 \times 10^{18} \text{ cm}^{-3}$ for $T_a = 20^\circ \text{ C}$. However, the differential gain is significantly less

than the value of $1.2 \times 10^{-15} \text{cm}^2$ at $T_a \approx 20^\circ \text{C}$ for a $10 \mu\text{m} \times 750 \mu\text{m}$ HR/cleaved device from the same wafer reported in [88] obtained through a relative intensity noise measurement. We attribute the discrepancy to wafer uniformity and device heating. The other laser was inherently better, possessing a 20% lower threshold for the same T_a . Also, the differential gain measured from Fig. 3.10 is significantly underestimated due to device heating. The transparency concentration increases and the differential gain decreases with temperature, leading to a sharp reduction in gain at fixed carrier concentration. Applying the gain formulas in [89] to our band structure, we calculate that the measured differential gain would have been $8.9 \times 10^{-16} \text{cm}^2$ if T_a were held constant at 20°C instead of increasing from 20°C at transparency to 35°C at $4 \times 10^{18} \text{cm}^{-3}$.

3.4 Internal Efficiency and Pinning of TSE

In pulsed mode, $T_s = 15^\circ \text{C}$, the TSE-EDGE spectra were collected for various current densities for a $20 \mu\text{m} \times 533 \mu\text{m}$ device. Lasing occurred at 851meV and $1.7 \text{kA}/\text{cm}^2$. The lasing energy is blueshifted compared to previous data due to the lower T_a in pulsed mode. The emission rate at evenly spaced energies was extracted and a few are plotted versus the current in Figs. 3.11a and 3.11b. The vertical axis in Fig. 3.11b is one-fifth that of Fig. 3.11a. In both figures, the spontaneous emission rate for each of the energies continued to increase above threshold. The increase in the 851meV curve at threshold is due to scattered laser light.

Above threshold, the Fermi levels and carrier concentrations are expected to pin strongly because stimulated emission should consume every additional injected carrier [90]. The spontaneous emission should saturate for wavelengths close to lasing wavelength. However, Fig. 3.11a shows that the spontaneous emission is only weakly clamped. For energies near 851meV, but outside the lasing spectrum (not shown

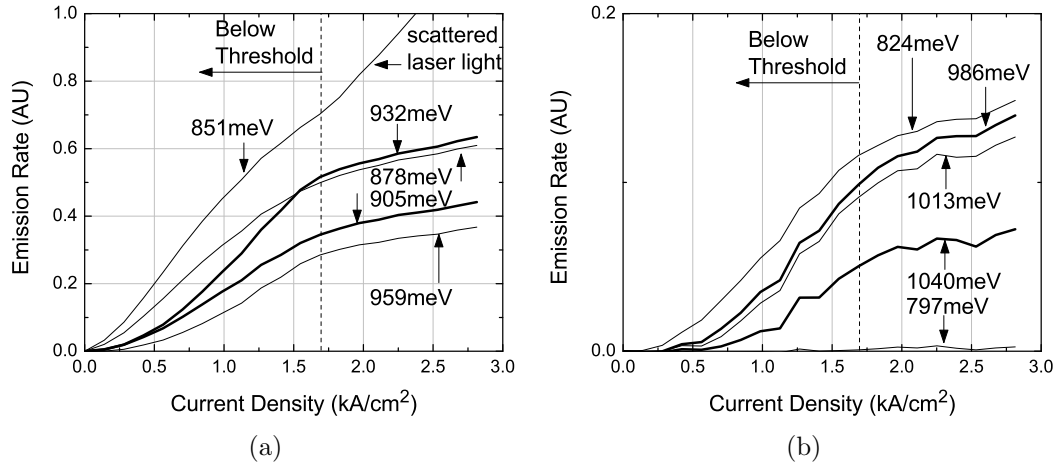


Figure 3.11: TSE-EDGE spectra at 15 °C at uniformly spaced energies versus current density in pulsed mode. Lasing occurred for this $20\mu\text{m} \times 533\mu\text{m}$ device at 851meV and $1.7\text{kA}/\text{cm}^2$. (a) shows this scattered laser emission plus four other emission energies, while (b) is a zoomed view of the five weaker emission energies. Above threshold, emission from the energies close to the lasing transition is only weakly clamped. The clamping is even weaker for transitions not involving the main levels E^1 and HH^1 .

in Fig. 3.11), the emission efficiency (slope) above threshold is still about 22% of the below threshold value, indicating that the carrier concentrations are not pinned throughout the entire structure. The emission efficiency ratio was also 22% near the 940meV TSE peak (E^1 -HH³, E^1 -LH_{Barrier}), but it increased to 34% near the 1022meV TSE peak (E^2 -HH², E^2 -LH_{Barrier}) and was close to 100% near the 1114meV peak (E -LH)_{Barrier}. If carriers do not rapidly scatter from excited bands, less pinning would be expected for transitions not involving the main levels E^1 and HH¹.

Partially amplified spontaneous emission (PASE) spectra, in the QW plane at $\theta=50^\circ$ relative to the optical axis were also collected. We call it PASE because spontaneous emission emitted at an angle of 12° relative to the optical axis can traverse as much as $100\mu\text{m}$ inside the $20\mu\text{m}$ wide device and still be collected, and in addition some on-axis ASE might be scattered into the collection assembly. Nevertheless, PASE primarily consists of the unamplified spontaneous emission at the facet. As a result, the PASE peak wavelength and other spectral features are between that of the TSE and ASE. The emission efficiency ratio was 16% near 851meV and 14% near 940meV, but ratios for the other peaks could not be computed because of insufficient signal strength in pulsed mode.

The optics in the EDGE configuration primarily image the section of the active region near the ridge waveguide edge where lateral current/carrier spreading provide fewer carriers and the optical field is weaker than in the direct center of the ridge. There would be lower gain and weaker stimulated emission at the edge and this could explain the continued spontaneous emission above threshold. Since the optics in the PASE spectra image an entire waveguide cross-section, whose emission is dominated by the ridge center, the PASE spectra should clamp more strongly than the EDGE spectra, which it did, 16% versus 22%. Another carrier spreading effect is non-uniform injection along the cavity length because the top metal contact was only 2000\AA thick.

This longitudinal non-uniformity was partially alleviated by probing the sample every $250\mu\text{m}$ along the length.

These two non-uniform spreading effects would reduce the device's quantum efficiency by η_s^d , the current spreading efficiency factor, described in [90, 91]. From the PASE measurement, we calculate $(\eta_s^d)_{lateral}=84\%$ for lateral spreading. For longitudinal spreading, we measured the external differential quantum efficiency and threshold with various probe separations. The values improved as the probe separation was reduced, but the improvements saturated for separations less than $400\mu\text{m}$. Thus, $(\eta_s^d)_{longitudinal} \approx 100\%$ for our experiments. Therefore, non-uniform spreading only partially explains the device's low internal efficiency of 45-55%.

Another explanation of the low efficiency and its temperature dependence is poor injection efficiency, η_i^d , also described in [90, 91]. We suspect that carriers, even those near the ridge center, can continue to recombine non-radiatively above threshold through traps in the barriers because the barrier populations do not clamp strongly at threshold [92]. The $(\text{N-N})_{As}$ and $(\text{As-N})_{As}$ split interstitial defects are formed during barrier growth as a means to partially compensate tensile strain [78]. Provided that the traps are accessible to electrons, the trap recombination rate will be limited by hole capture, which is proportional to the density of holes in the barrier. Thus, recombination in the p-side barrier should be larger than in the n-side barrier. Electrons can reach p-side barrier traps in three ways: traversing the QW during injection, tunneling from the QW to defects near the QW/barrier interface, or after thermionic emission from the QW into the barriers. The $(\text{As-N})_{As}$ defect easily captures electrons during injection since it is at the same energy as the GaNAs barrier conduction band minimum. This direct capture process obviously reduces η_i^d . The $(\text{N-N})_{As}$ defect is located $\approx 100\text{meV}$ below the QW conduction band edge and so capture after thermionic emission is more likely for this trap, especially at elevated temperatures

or carrier densities. Phonon-assisted tunneling from the QW to the $(N-N)_{As}$ trap becomes easier as the electron levels of the QW become more resonant with the defect level at high temperatures or carrier densities due to bandgap redshifting and BGR, respectively. The presence of these traps and their effect on threshold current density will be explored subsequently through Z-parameter measurements.

3.5 Local Z-parameter

3.5.1 Theory

Analysis of radiative and non-radiative recombination can be made by measurements of the local Z-parameter. The Z-parameter describes the dominant process for recombination in semiconductor lasers [41, 42, 93]. The injected current balances the net recombination in steady state. Assuming Boltzmann statistics, charge neutrality $n=p$ in the undoped QW, and neglecting stimulated emission, this balance is expressed according to:

$$\begin{aligned} I_{Tot} &= eV_a R(n) \\ R(n) &= An + Bn^2 + Cn^3 \end{aligned} \tag{3.2}$$

where I_{Tot} is the total current, e is the electronic charge, V_a is the active volume, $R(n)$ is the net recombination rate, and A , B , and C are the monomolecular, radiative, and Auger coefficients, respectively. The total spontaneous emission rate is proportional to the radiative current, I_{Rad} ,

$$\begin{aligned} I_{Rad} &= eV_a Bn^2 \\ TSE &\propto I_{Rad} \propto n^2 \end{aligned} \tag{3.3}$$

If one of the recombination processes dominates the current, Equation 3.2 can be approximated by,

$$I \propto n^Z \quad (3.4)$$

where Z can range from 1 to 3 if the current is dominated by monomolecular ($Z \approx 1$), radiative ($Z \approx 2$), or Auger recombination ($Z \approx 3$). This interpretation is valid for a limited current range. From Equations 3.3 and 3.4, Z can be solved for as the derivative (slope) of the $\text{Ln}(I)$ versus $\text{Ln}(TSE^{1/2})$ relationship. Defining the local Z -parameter as this instantaneous derivative, and assuming that A , B , and C are independent of n , Equations 3.2 and 3.3 yield [94],

$$Z \equiv \frac{d(\text{Ln}(I))}{d(\text{Ln}(TSE^{1/2}))} = 1 \frac{I_{Mono}}{I_{Tot}} + 2 \frac{I_{Rad}}{I_{Tot}} + 3 \frac{I_{Aug}}{I_{Tot}} \quad (3.5)$$

where I_{Mono} and I_{Aug} are the monomolecular and Auger current. This extends the previous interpretation of Z to range continuously as an average of the Z -parameters for the various processes weighted by their fractional contribution to the total current. Z is bounded between 1 and 3 where monomolecular and Auger dominate. Any departure from $Z=2$ indicates the presence of non-radiative recombination, but $Z=2$ can also occur with equal amounts of monomolecular and Auger recombination since Z can be re-expressed as:

$$Z = 2 + \frac{I_{Aug} - I_{Mono}}{I_{Tot}} \quad (3.6)$$

by using $I_{Rad} = I_{Tot} - I_{Aug} - I_{Mono}$. A value of Z below 1.5 indicates that at least 50% of the current is monomolecular.

In real devices, two non-ideal effects complicate the Z -parameter analysis. First, there can be significant carrier leakage into the barriers or separate confinement heterostructure (SCH) waveguide at high injection levels. Using the band structure data of Fig. 3.8 and assuming parabolic bands, we calculate that the electron and hole

barrier populations increase superlinearly with the quantum well carrier density as n^r . For electrons, this exponent r increases from 1.0 to 2.1 as n increases from zero to $2.5 \cdot N_c$, where $N_c = 1.6 \times 10^{18} \text{cm}^{-3}$ is the effective conduction band density of states. For holes, it only increases from 1.0 to 1.2 over the same carrier densities. The exponent r increases more rapidly when the band is degenerate and is about 3% larger in the SCH waveguide due to the increased barrier height. Therefore, carrier leakage can vary anywhere from n^1 to $n^{2.1}$ for monomolecular barrier recombination, n^2 to $n^{3.3}$ for radiative barrier recombination, n^1 to $n^{2.2}$ for diffusive leakage into the SCH cladding, and n^2 to $n^{5.2}$ for drift leakage. Thus, $Z > 3$ would seem to be good evidence of carrier leakage. Drift leakage is proportional to the SCH carrier density and also the injected current [95], so the exponent can be much larger and vary more depending on whether the injected current is dominated by monomolecular, radiative or Auger recombination. However, drift and diffusive leakage into the SCH cladding were calculated to be negligible in our devices [92] because of the high electrical conductivity in the AlGaAs cladding layers and large AlGaAs/GaAs hetero-barriers [96]. Further, the TSE measurements of Figs. 3.2a and 3.2b show that radiative barrier recombination is negligible. Auger recombination in the barriers is also negligible due to the lower carrier concentrations and larger bandgap.

Second, and more importantly, Fermi-Dirac statistics must be used for the high injection levels encountered during typical laser operation. Assuming that electrons become degenerate first ($m_{hh} > m_e$), the electron Fermi occupation factor of the ground state, f_e^{GS} , asymptotes to unity while the hole occupation factor, f_h^{GS} , remains proportional to p . In this degenerate limit, the radiative rate for the $E^1\text{-HH}^1$ transition is no longer proportional to n^2 , but rather asymptotes to being proportional to n . By the same argument, the dominant channel for CHCC (C=conduction, H=heavy hole) Auger recombination will asymptote to being proportional to n , while CHHS

(S=split-off) recombination will asymptote to n^2 [97]. However, the number of carriers capable of satisfying both energy and momentum conservation for these Auger processes increases superlinearly. Numerically integrating the formulas in [98], we find that CHCC increases from n^3 to $n^{3.8}$ and CHHS increases from n^3 to $n^{3.1}$ as n increases from zero to $2.5 \cdot N_c$. Thus, Z will exceed 3 for both CHCC and CHHS processes. The dependence of Auger recombination on carrier density is quite sensitive to the bandgap, effective masses, and whether the process is phonon-assisted [99]. Z will remain constant at 2 for radiative recombination, but increase from 1 to 2 for monomolecular recombination in the QW and will be larger for monomolecular barrier recombination. Although the first electron band becomes degenerate, the second band, 82meV higher, remains non-degenerate and so these degeneracy effects are less pronounced here than in the case of a QW with only 1 confined electron and hole level.

To expand the Z -parameter analysis to the degenerate case, we begin by expressing the total current as a summation over all recombination currents:

$$I = \sum_{AllProcesses} f_{Process}(n) \quad (3.7)$$

and allow for arbitrary dependencies on carrier density. We define an effective Z -parameter for each process using its logarithmic derivative definition:

$$Z_{Process}^{Effective} \equiv \frac{d(\text{Ln}(f_{Process}))}{d(\text{Ln}(TSE^{1/2}))} \quad (3.8)$$

If the current is completely dominated by a particular recombination mechanism, it is the effective Z -parameter of that process that would be measured experimentally.

Fig. 3.12 is a simulation of the behavior of the effective Z -parameter versus carrier density at 35 °C if the current is dominated by various recombination mechanisms

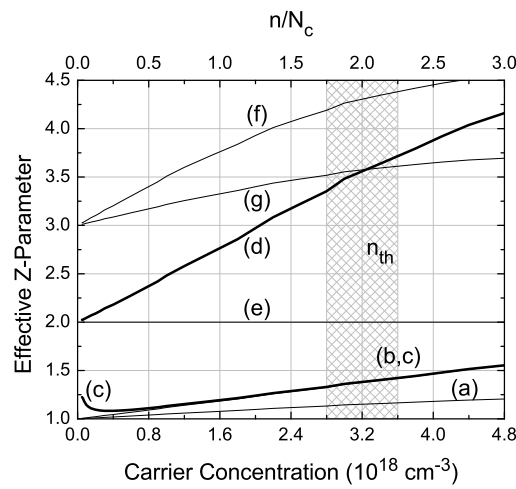


Figure 3.12: Simulation of the behavior of the Z-parameter versus carrier density for the band structure of Fig. 3.8 for cases where the current is dominated by a particular recombination mechanism: (a) mid-level QW traps, (b) mid-level barrier traps, (c) $(N-N)_{As}$ barrier electron traps, (d) $(As-N)_{As}$ barrier electron traps, (e) radiative, (f) CHCC, and (g) CHHS. Curves (a) and (b) begin together but separate since the barrier population increases superlinearly. Incomplete trap filling in curve (c) can cause $Z_0 > 1$ and Z to initially decrease. As the traps fill, curve (c) asymptotes to (b). Curve (e) has a constant value of 2.

that might exist in our device: (a) mid-level QW traps, i.e. ideal monomolecular, (b) mid-level barrier traps, (c) (N-N)_{As} barrier electron traps, (d) (As-N)_{As} barrier electron traps, (e) radiative, (f) Auger CHCC, and (g) Auger CHHS. Some additional parameters used in the simulation were listed at the end of Table 3.2. The range of threshold carrier densities for different length devices is shaded in Fig. 3.12. Z increases for processes (a) through (d) because of degeneracy and for (f) and (g) because of the increase of carriers that can conserve energy and momentum. A quick calculation shows that if all recombination processes are considered (i.e. Equation 3.7) then the measured Z -parameter equals the average effective Z -parameter of the constituent recombination processes weighted according to their proportion of the total current:

$$Z = \sum_{AllProcesses} Z_{Effective} \frac{I_{Process}}{I_{Tot}} \quad (3.9)$$

This generalizes the weighted average formulation in the second half of Equation 3.5 to the degenerate regime and to handle carrier leakage and other non-ideal recombination processes. Since $Z_{Process}^{Effective} \geq 2$ for every process except monomolecular recombination from midlevel QW traps and (N-N)_{As} traps near the conduction band edge, a measurement of $Z < 1.5$ indicates that at least 50% of the current must be due to these traps.

Due to the small density of states ratio $\mu = N_c/N_v = m_e/m_{hh} = 0.32$, the conduction band quickly becomes degenerate at low injection levels. The electron quasi-Fermi level crosses the first confined electron level at $n = 1.2 \times 10^{18} \text{cm}^{-3}$ ($n/N_c = 0.75$ or $J \approx 0.4 \text{kA/cm}^2$). Above that point, Equation 3.9 should be used instead of Equations 3.5 and 3.6.

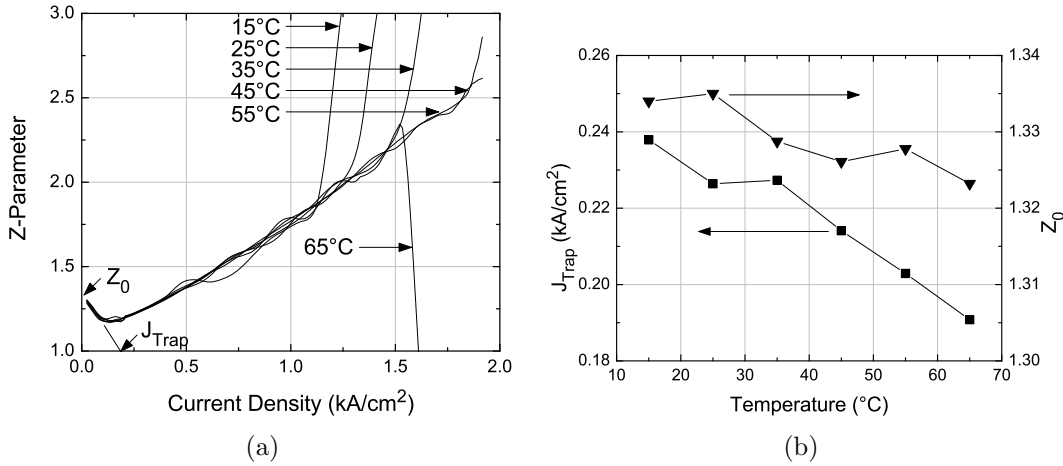


Figure 3.13: (a) Measured Z-Parameter for $T_s=15-65$ °C versus current density for a $10\mu\text{m} \times 750\mu\text{m}$ device using WINDOW configuration in CW mode ($J_{th}^{CW}=1.0\text{kA}/\text{cm}^2$ at $T_s=15$ °C). The kink in the Z-J curve is also a good indicator of threshold. (b) J_{Trap} and Z_0 versus stage temperature. The lines serve as a guide for the eyes in (b).

3.5.2 Experiment

To measure the Z-parameter at various currents and temperatures in a reasonable amount of time, the integrated TSE was measured with an InGaAs P-I-N detector instead of collecting the spectra with the OSA and integrating numerically. Since the integrated TSE rate is the desired quantity, the InGaAs detector will perform the integration electrically provided that the detector's quantum efficiency is independent of wavelength. The detector used had a quantum efficiency that was flat to within 6% over the 300nm range of the two dominant emission peaks of Figs. 3.2a and 3.2b and so the overall accuracy was only slightly deteriorated using this shortcut.

The WINDOW configuration in CW mode, with 1mA current steps, was used on a $10\mu\text{m} \times 750\mu\text{m}$ HR/cleaved device ($J_{th}^{CW}=1.1\text{kA}/\text{cm}^2$ at $T_s=15$ °C) to obtain the local Z-parameter at various temperatures. The data, plotted in Fig. 3.13a, was collected in CW mode to improve the accuracy of the applied current. The device

failed suddenly during the $T_s=65^\circ\text{C}$ measurement, indicated by the abrupt drop of Z . At low current density but above J_{Trap} (to be discussed later), the Z -parameter appears to be independent of temperature and increases almost linearly with current density. At threshold, the TSE weakly clamps and the Z -parameter diverges to $+\infty$. The sudden rise in Z provides a surprisingly good indicator of lasing threshold. At room temperature, $T_s=25^\circ\text{C}$, Z increases gradually from 1.2 to above 2.0 just below threshold. At low currents, the device is clearly dominated by monomolecular recombination. Near threshold, Z is rising and $Z_{th} \approx 2$ indicating comparable and sizable amounts of monomolecular and leakage or Auger recombination. A possible distribution of the threshold current at room temperature that is consistent with Equations 3.5 and 3.6 is 40% monomolecular, 20% radiative, and 40% Auger. However, due to high injection at threshold and possible leakage, a 70% barrier and QW trap recombination, 20% radiative, and 10% Auger distribution is more consistent with our band structure measurements and Equation 3.9. This device has a thermal resistance of 45K/W. In CW mode, this produces a slight temperature rise in T_a of 6-13 $^\circ\text{C}$ when the threshold increases from 1 to 2kA/cm², which obscures the exact dependence of Z_{th} on temperature.

A peculiarity of our GaInNAsSb lasers with GaNAs barriers, not seen in GaInNAs lasers with GaAs barriers [42], is that at very low current densities, Z does not asymptote to 1 but rather has a minimum and increases to $Z_0 > 1$ as J approaches zero. It was suggested [100] that the density of traps is so large that they are not completely filled at low currents. We believe that this might be the case, especially if the trap levels are located close to the QW conduction band edge, e.g. the $(N-N)_{As}$ split interstitial trap. The electron's quasi-Fermi level would be below the trap level at low biases, leading to only partial occupation of the electron trap. Instead of the recombination rate being proportional to the hole density, p , and the trap density, N_t , it would be proportional to p and some function of the electron density, e.g. $n^{1/3}$,

since the number of occupied traps would increase sublinearly with electron concentration. This would lead to a value for Z_0 of 1.33. We define a quantity, J_{Trap} , as the current density at which the lowest region of the Z-J curve extrapolates to $Z=1$ (see Fig. 3.13a). It approximates the current density required to fill the trap levels. These two features were investigated in the Fig. 3.12 simulation. $Z_0 \approx 1.3$ if the electron traps are located inside the bandgap, 100meV from the QW band edges, and N_t is small compared to N_c . Z_0 decreases from 2 to 1 and J_{Trap} decreases to zero as either the trap level location moves from the band edges to mid-bandgap or the trap density decreases. The traps in curve (c) can be considered filled when curves (b) and (c) begin to overlap. From Fig. 3.12, we see that this occurs at approximately the same carrier density as the extrapolation of curve (c) to $Z=1$.

From the temperature dependent Z-parameter data, we plot both Z_0 and J_{Trap} versus T_s in Fig. 3.13b. From $T_s=15$ to 65°C , Z_0 decreases slightly from 1.334 to 1.323 and J_{Trap} decreases from 238 to 190A/cm². At higher temperatures, the trap occupancy increases due to the broader Fermi-Dirac distribution and therefore both Z_0 and J_{Trap} are expected to decrease. A reduced trap level concentration for GaAs compared to GaNAs might explain why $Z_0=1$ for GaInNAs devices with GaAs barriers while $Z_0 > 1$ in our devices.

As the temperature is increased, the threshold density increases exponentially. At threshold, Z_{th} increases from 1.90 to 2.05 to 2.25 to 2.50 as T_s is increased from 15 to 45°C in 10°C steps. For comparison, Fehse et. al. [42] report that Z_{th} increases from 2.1 to 2.4 in GaInNAs/GaAs at $1.3\mu\text{m}$ and is roughly saturated at 2.9 in InGaAs/InP at $1.3\mu\text{m}$ over the same 15 to 45°C temperature range.

The temperature dependence of the recombination coefficients A, B, and C is expected to be [42, 81, 101],

$$\begin{aligned} A &\propto T^{1/2} \\ B &\propto T^{-1} \\ C &\propto \text{Exp}\left(-\frac{E_a}{k_B T}\right) \end{aligned} \quad (3.10)$$

where E_a is the activation energy for the Auger process. C is a rapidly varying function of temperature; it is nearly zero but increases swiftly for $k_B T \ll E_a$ before saturating for $k_B T \gg E_a$. Near room temperature, the monomolecular coefficient A, was observed to saturate in GaInNAs at $1.3 \mu\text{m}$ [42], due to the saturation of the thermal velocity, so we will assume that A is approximately constant for GaInNAsSb at $1.5 \mu\text{m}$ as well.

At low carrier densities, monomolecular and radiative recombination dominate, and since A is temperature insensitive and B decreases by $<15\%$ over the limited temperature range of the measurement, the low current density Z-J curves in Fig. 3.13a agree with this prediction of a temperature insensitive relationship. At and above $T_s = 35^\circ \text{C}$, where the threshold current density is above $1.5 \text{kA}/\text{cm}^2$ and Z_{th} exceeds 2.25, leakage and/or Auger recombination begin to dominate and the high current density portion of the Z-J curves should begin to separate with temperature due to the strong temperature dependence of these processes. This predicted feature is not visible in Fig. 3.13a, because the data in this region is limited to a small temperature range $\Delta T = 20^\circ \text{C}$. A device with low thermal resistance and two anti-reflective coated facets to prevent heating and lasing, respectively, is needed to investigate this prediction further. Although Z should continue to increase with J above $1.5 \text{kA}/\text{cm}^2$ at low temperature, the rate of increase should be less than at high temperature.

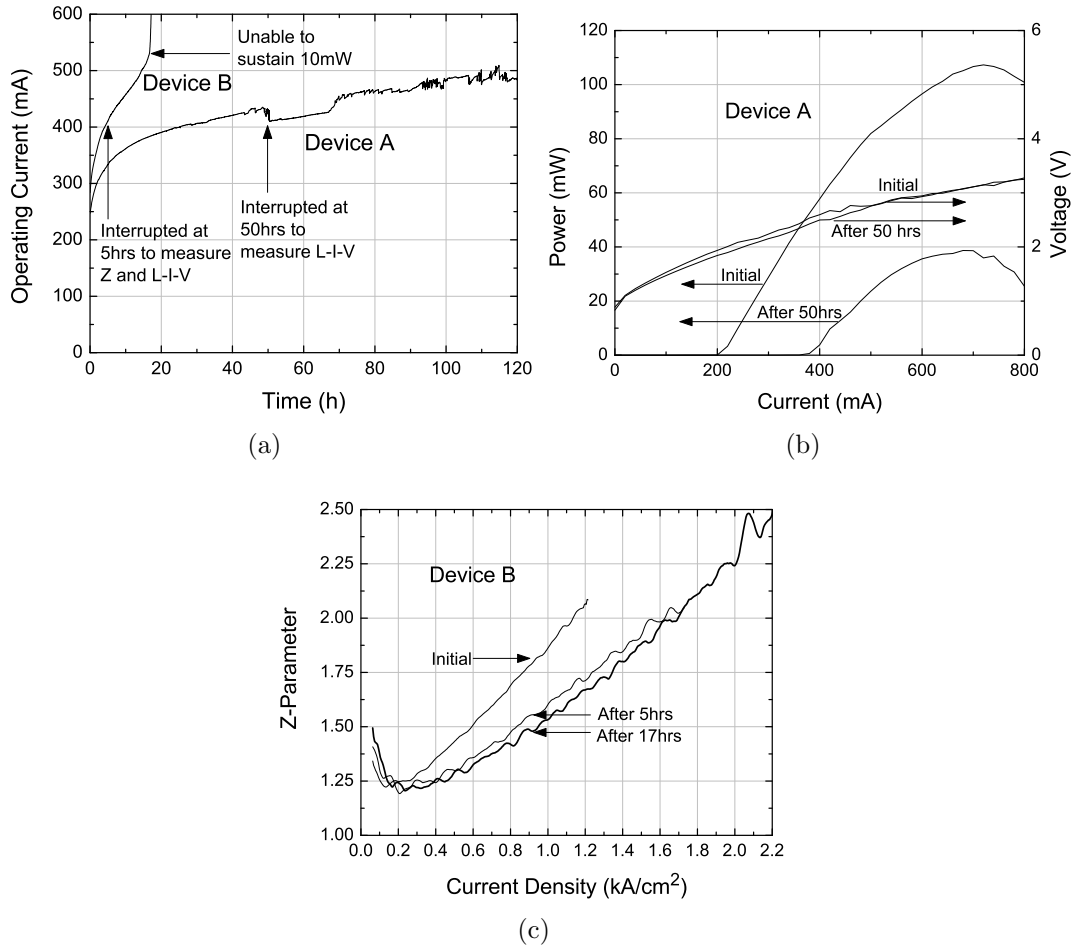


Figure 3.14: (a) Operation current versus time for two $20\mu\text{m} \times 1000\mu\text{m}$ devices at 10mW CW. Device A, which had a better pre-test performance, survived over 120 hours of operation at $T_s=15^\circ\text{C}$, while device B device only lasted 17 hours at $T_s=20^\circ\text{C}$. (b) CW L-I-V curves before life testing and after 50 hours for device A. (c) Z-J curves for device B. During life testing, the Z-parameter at fixed J is reduced and Z_0 and J_{Trap} both increase. These three changes indicate an increase in the trap density during life testing.

Table 3.3: Performance metrics during life testing for two $20\mu\text{m} \times 1000\mu\text{m}$ devices at 10mW CW. Device A had $T_s=15^\circ\text{C}$; device B had $T_s=20^\circ\text{C}$. After 50 hours, the CW threshold current increased by 79% and external differential quantum efficiency decreased by 39% of their respective pre-test values for device A. Device B showed a 90% threshold increase and 69% efficiency decrease in CW mode after only 17 hours, but it had only a 55% threshold increase and 24% efficiency decrease in pulsed mode. Z_0 and J_{Trap} both increase during life testing.

Device	Time (h)	J_{10mW} (kA/cm ²)	T_a (°C)	J_{th}^{CW} (kA/cm ²)	η_e^{CW} (%)	P_{max}^{CW} (mW)	J_{th}^{PUL} (kA/cm ²)	η_e^{PUL} (%)	Z_{th}	Z_0	J_{Trap} (kA/cm ²)
A	0	1.25	30	1.05	38	107
A	50	2.12	48	1.88	23	39
A	120	2.43	50
B	0	1.43	36	1.18	35	67	0.97	41	2.05	1.48	0.212
B	5	2.05	48	1.79	22	26	1.34	35	2.05	1.57	0.233
B	17	2.63	59	2.24	11	4.5	1.50	31	2.53	1.63	0.254

3.6 Reliability

A $20\mu\text{m} \times 1000\mu\text{m}$ laser, labeled device A, was operated at $T_s=15^\circ\text{C}$ at 10mW CW output power for 120 hours. The time evolution of the operating current, I_{op} , is the lower curve of Fig. 3.14a. Notice the sharp increase in current during the first 10 hours, followed by a slower gradual increase. Part of the current increase is due to device heating. After 50 hours, life testing was interrupted to remeasure the CW light-current-voltage (L-I-V) curves, which are plotted in Fig. 3.14b. Device performance metrics are listed in Table 3.3. Both the threshold and efficiency were degraded and the thermal rollover current was reduced slightly. The V-I curve did not change significantly. After 122 hours of life testing, one of the probes accidentally lost contact and scratched the sample and we were unable to obtain reliable L-I-V measurements after the life test.

The high levels of monomolecular recombination, observed in the Z-parameter measurements, provide thermal energy that enhances defect propagation. The active

region and barriers are expected to have numerous point defects since they are highly strained metastable alloys, grown at low temperatures. During life testing, these point defects can diffuse and nucleate extended defects that can propagate. This further accelerates device failure by increasing the number of non-radiative recombination sites. Since the defects relieve strain, the defect creation rate might be large initially but decrease over time leading to a slower gradual increase in I_{op} .

To investigate this further, life testing was conducted on a similar $20\mu\text{m} \times 1000\mu\text{m}$ laser, device B, also operated at 10mW CW output power, but at $T_s=20^\circ\text{C}$ and a Z-parameter measurement and pulsed and CW L-I-V measurements were conducted before and during life testing. Device B had a slightly worse pre-test threshold and efficiency than device A and was also operated at $T_s=20^\circ\text{C}$ instead of 15°C (See Table 3.3). It was only able to sustain 10mW CW for 17 hours, as shown in the upper curve of Fig. 3.14a. Again, a sharp increase in current was observed during the first 10 hours, but because of the higher T_a and I_{op} , the device failed before the slower gradual increase was observed. The changes to the CW L-I-V curves during life testing were similar to those for device A, but occurred more rapidly. The degradation to the pulsed mode L-I-V curves was less noticeable.

The Z-J curves for device B before life testing, after 5 hours, and after 17 hours are displayed in Fig. 3.14c. At a fixed current density, the Z-parameter is reduced over time and the Z-J curve remains closer to $Z=1$, indicating an increase in the monomolecular recombination current. The value of Z_{th} increases over time from 2.05 to 2.58 after 17 hours due to the increase in T_a at threshold from 33 to 50°C . From the Z-J curves, we estimate that the monomolecular current density increased by approximately $0.45\text{kA}/\text{cm}^2$ at threshold over 17 hours. This agrees with the observed $0.53\text{kA}/\text{cm}^2$ increase in the total pulsed threshold density. Thus, additional device heating causes the other half of the $1.06\text{kA}/\text{cm}^2$ increase in CW threshold.

Z_0 and J_{Trap} both increased during life testing. The rise of Z_0 indicates a reduction in the trap occupation probability and the rise in J_{trap} indicates that higher currents are needed to fill the traps. These two changes can be caused by three things: (1) an increase in the $(N-N)_{As}$ trap density, (2) an increase in the trap energy position relative to the QW band edge, or (3) an increase in the $(As-N)_{As}$ trap recombination. However, only the first case would lead to the Z-J curve remaining closer to $Z=1$. Thus, we conclude that the primary source of device degradation is an increase in $(N-N)_{As}$ trap recombination and that the degradation is more pronounced in CW operation because of device heating.

On a similar device, C, the TSE spectrum at constant density of $3\text{kA}/\text{cm}^2$ at $T_s=70^\circ\text{C}$ ($T_a=115^\circ\text{C}$) was collected for 6 hours. The emission rate for the $E^1\text{-HH}^1$, $E^1\text{-HH}^3$, $E^2\text{-HH}^2$, and $(E\text{-LH})_{Barrier}$ and 800meV transitions decreased by 6%, 9%, 11%, 16%, and 9%, respectively. The extra reduction in the higher order transitions indicates a lower overall carrier density at fixed current. Pre/post Z-parameter measurements again show increased monomolecular recombination. Since the 800meV emission peak did not increase in strength, we conclude that the peak is not caused by a radiative transition from the $(N-N)_{As}$ trap level as was initially suspected, but is instead the exciton peak.

There is a heating induced feedback that drastically increases operation current and device degradation during constant power CW operation. An increase in non-radiative recombination elevates T_a due to the electrical and thermal resistance. Increased T_a reduces gain and thus increases the threshold current, which is already mostly non-radiative. This increases T_a again and the new steady state operating current is much higher than indicated by the simple small increase in non-radiative current. Further, the trap creation rate increases due to the increases in T_a and non-radiative current.

It is believed that the device's accelerated failure rate, AF, increases rapidly with current density and temperature according to [102]:

$$AF = \left(\frac{J_a}{J_u}\right)^n \text{Exp}\left(\frac{E_a}{k_B T}\right) \quad (3.11)$$

where J_a is the applied current density, J_u is a reference current density, and E_a is the activation energy for the degradation process, and $n \approx 2$ is an empirical factor. The operation at higher overall current causes a quadratic increase in the device damage rate. Also, operation at higher temperature activates more device degradation mechanisms.

By mounting the devices epi-side down, the thermal resistance can easily be reduced by two to three-fold for ridge waveguide devices and four to six-fold for broad area ($>50\mu\text{m}$ wide) devices as discussed in Section 5.2. Combined with a lower series resistance design, this avalanche effect can be mitigated. Also, by reducing non-radiative recombination from barrier traps, i.e. using GaAs barriers, improving the material quality of GaNAs barriers, or increasing the barrier height, device lifetimes comparable to the 1000 hours at 1.5W of CW power in $1.3\mu\text{m}$ GaInNAs [45] can be expected for GaInNAsSb at $1.5\mu\text{m}$.

Chapter 4

Characterization and Comparative Measurements of High Performance Lasers

A large portion of this chapter has been accepted for publication in the Proceedings of the SPIE [88]. It can be found at <http://spiedl.aip.org/> after it is published. The dissertation author's role was to write the article and perform the measurement and data analysis of the lasers fabricated by the other authors of the paper.

In this chapter, high performance lasers are characterized through standard and advanced techniques. Throughout this chapter, we will present results about devices labeled 2^{nd} generation in Fig. 1.5, and compare the results to the previously reported results for 1^{st} generation devices [27, 74, 92] and discussed in Chapter 3. The main difference in the generations arises from improvements in the post-growth processing techniques.

We will start by discussing standard room temperature characteristics of the 2^{nd} generation lasers in Section 4.1. A typical $20 \times 1222 \mu\text{m}$ device, tested epitaxial-side up at room temperature, has a threshold density below $600 \text{A}/\text{cm}^2$, external quantum efficiency above 50%, and an output power exceeding 200mW from both facets. In

pulsed mode, $450\text{A}/\text{cm}^2$, 50%, and 1100mW were realized. Longer devices yielded over 425mW of total CW power and thresholds below $450\text{A}/\text{cm}^2$.

The advanced characterization begins in Section 4.2 with Z-parameter measurements, which track the dominant sources of recombination as discussed in Section 3.5. The analysis is used to identify the source(s) of these improvements in the performance metrics of approximately 40-60% over 1st generation devices. In Section 4.3, we apply the method of Tansu and coworkers [103], which measures laser performance as a function of temperature and cavity length. The method determines the characteristic temperature of intrinsic laser parameters, such as: g_0 , J_{tr} , η_i , and α_i and was previously applied to 1st generation devices [92]. In Section 4.4, we analyze the relative intensity noise (RIN) spectra and present additional intrinsic laser parameters, such as the differential and nonlinear gain coefficients. The temperature dependence of these parameters is also discussed as well as their implication regarding the suitability of GaInNAsSb in directly modulated laser applications. Finally, in Section 4.5, we present reliability measurements under high power operation.

Testing was done under both CW and pulsed ($1\mu\text{s}$ width, 1% duty cycle) conditions. The temperature dependent cavity length study (Section 4.3) was conducted in pulsed mode to avoid heating. However, the Z-parameter (Section 4.2) and RIN (Section 4.4) measurements were taken in CW mode to improve the measurement signal-to-noise and the accuracy of the applied current at the expense of about 5-10 °C of device heating at threshold. We will denote the stage and active region temperatures by T_s and T_a , respectively and room temperature (RT) is 20 °C. The thermal resistance, R_{th} , of our devices has been extensively measured and is modeled in Section 5.2. For $20\mu\text{m}$ wide devices, the resistance in K/W is approximately given by $R_{th}=30.3/L$, where L is the device length in millimeters.

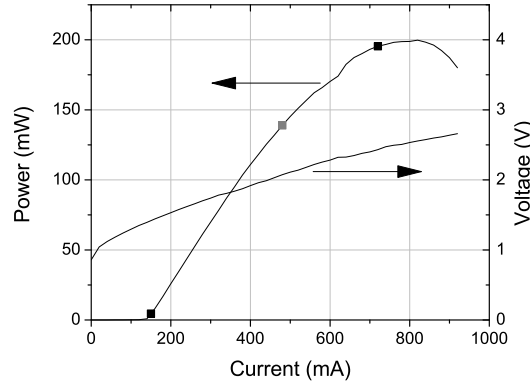


Figure 4.1: CW L-I-V curve for a $20 \times 1222 \mu\text{m}$ 2^{nd} generation laser at 20°C .

4.1 Room Temperature Characterization

By reducing ion-related damage during active layer growth [77] and minimizing defects by optimizing the rapid thermal annealing (RTA) process, we have significantly reduced monomolecular recombination, the previous cause of high thresholds. At room temperature, lasing occurred for 1^{st} generation devices at $1.46\text{-}1.49 \mu\text{m}$ and $1.1\text{-}1.5 \text{kA}/\text{cm}^2$, depending on device size and location on the wafer. Despite the reduction in threshold density achieved by 1^{st} generation devices of 3x compared to previous world records for $1.5 \mu\text{m}$ GaAs based lasers, the high density has remained unsatisfactory for commercial applications. The 2^{nd} generation devices were annealed at 740°C for one minute compared to the 1^{st} generation devices, which were annealed at 800°C . By optimizing the annealing process, the typical threshold densities were reduced to $450\text{-}700 \text{A}/\text{cm}^2$ for 2^{nd} generation devices. Lasing occurred at $1.46\text{-}1.48 \mu\text{m}$.

Fig. 4.1 shows typical room temperature L-I-V curves for a $20 \times 1222 \mu\text{m}$ 2^{nd} generation device. The threshold density was $580 \text{A}/\text{cm}^2$ and the external quantum efficiency was 53%. The maximum power from both facets was 200mW and limited by heating, due to 1.6Ω series resistance and high thermal resistance, $24 \text{K}/\text{W}$, from mounting

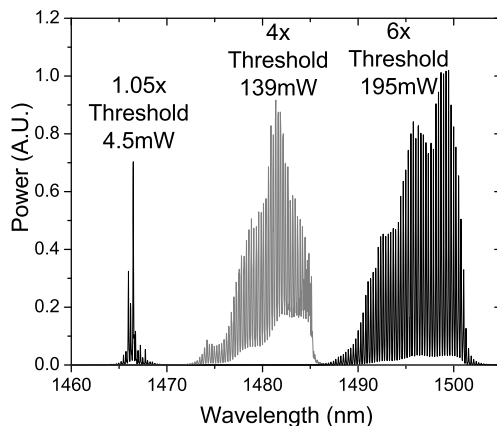


Figure 4.2: Optical spectra at various operation points for the laser of Fig. 4.1.

epi-side up. The series resistance, R_s , was about 0.4Ω lower than in comparable 1st generation devices, while the thermal resistance was about the same.

Fig. 4.2 is the optical spectra at three operation points marked in Fig. 4.1. The device lased at $1.465\mu\text{m}$ at threshold and at $1.50\mu\text{m}$ at maximum output power due to the 0.34meV/K bandgap reduction (0.58nm/K redshift) with temperature. The peak in the optical spectra at 6x threshold is only 40% greater than at 1.05x threshold despite the total output power being more than forty times larger. The peak intensity quickly saturates because of the large nonlinear gain compression coefficient ε , discussed in Section 4.4.

Fig. 4.3 is the pulsed (400ns width, 0.1% duty cycle) L-I-V curve at RT for the same device. The threshold density was 450A/cm^2 , the external quantum efficiency was 52%, and the maximum power was 1142mW from both facets. Peak pulsed output power was limited due to the 3A limit of the current driver.

To increase the maximum CW output power, P_{max} , improving the thermal and series resistance were investigated. There exists an optimal device length since the thermal conductance increases while the external efficiency decreases with length.

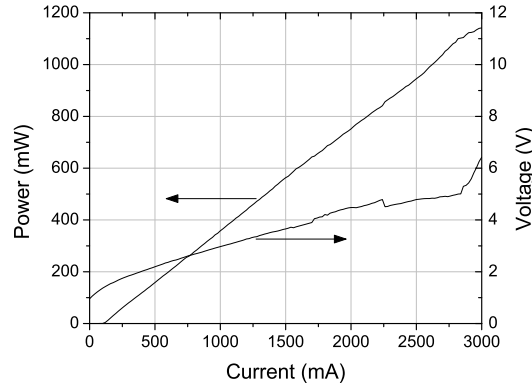


Figure 4.3: Pulsed L-I-V curve for a $20 \times 1222 \mu\text{m}$ 2^{nd} generation laser at 20°C .

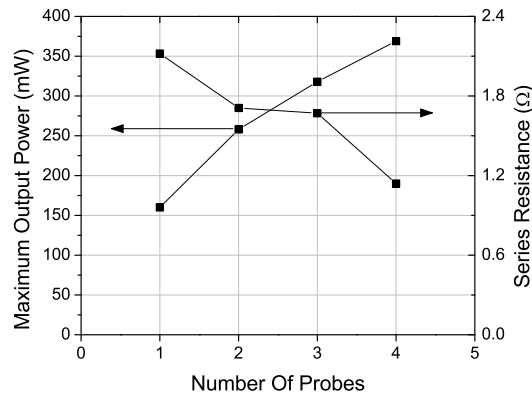


Figure 4.4: Dependence of P_{max} and R_s on number of probes.

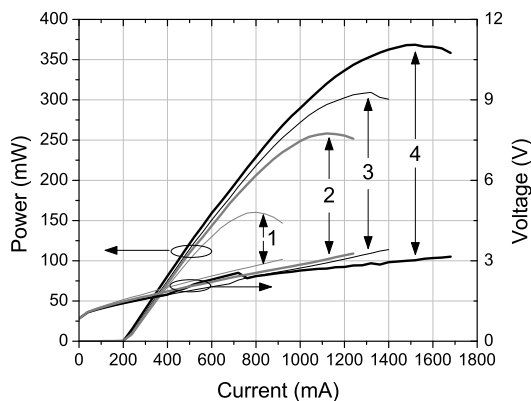


Figure 4.5: CW L-I-V curves for a $20 \times 2150 \mu\text{m}$ 2nd generation laser at 15°C versus number of probe contacts.

Modeling the length dependence of the device parameters determined in Section 4.3 indicated that this optimal length is around $1900\text{-}2600 \mu\text{m}$ for epi-up mounting. Devices with a size of $20 \times 2150 \mu\text{m}$ were processed. More detailed statistical simulations, presented in Chapter 5, indicate that the optimal length is more likely to be in the range of $3000\text{-}4000 \mu\text{m}$.

The contact resistance between the Tungsten probe tips and the Ti/Pt/Au p-metal as well as the longitudinal current spreading resistance of the ridge significantly affect the total series resistance. As illustrated in Fig. 4.4, increasing the number of probe contact points along the device length from 1 to 4 cut the device series resistance in half and more than doubled the output power. A contact resistance per probe value of $R_c = 1.06 \pm 0.39 \Omega$ was determined.

Fig. 4.5 shows a CW L-I-V curve ($T_s = 15^\circ\text{C}$) for the $20 \times 2150 \mu\text{m}$ laser as the number of probe contact points is increased. The threshold density improved from 510 to $480 \text{A}/\text{cm}^2$ and the external quantum efficiency from 45 to 49% with increasing number of probes due to the slight reduction in device heating near threshold and more uniform current injection. However, the most striking effect was the increase in

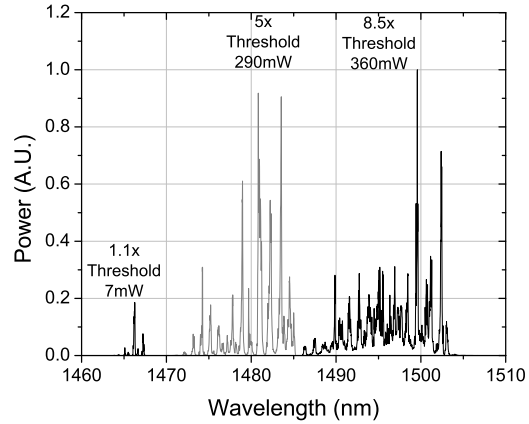


Figure 4.6: Optical spectra at various operation points for the laser of Fig. 4.5.

power from 160 to 369mW as a result of the reduced series resistance. Fig. 4.6 is the optical spectra at three operation points along the 4 probe contact L-I-V curve. The lasing wavelength and its thermal broadening and redshift are similar to Fig. 4.2.

Fig. 4.7 shows a CW L-I-V curve ($T_s=15^\circ\text{C}$) of a nearby $20\times 2150\mu\text{m}$ laser with 5 probe contacts. The device was slightly better than the previous one, but was damaged a little (see kink in I-V curve) before a probe contact study could be performed. The device had a $440\text{A}/\text{cm}^2$ threshold density at 1.32V and an external efficiency of 51%. A maximum of 431mW of power was obtained because R_s was reduced to 1.0Ω with the addition of the fifth probe. Output powers exceeding 500mW seem achievable if the number of contacts can be increased indefinitely, e.g. by using bond wire.

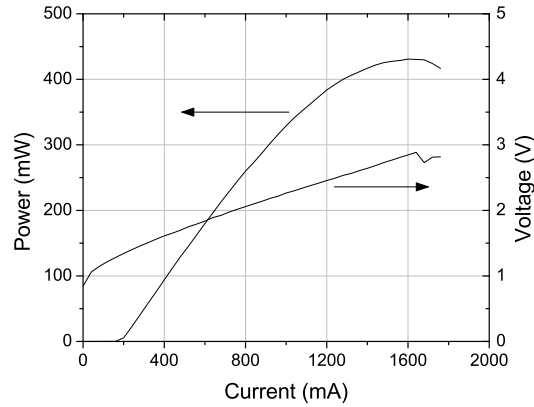


Figure 4.7: CW L-I-V curves for a $20 \times 2150 \mu\text{m}$ 2^{nd} generation laser with 5 probes at 15°C .

4.2 Z-Parameter Comparison

As described in Chapter 3, the Z -parameter can be used to analyze the dominant process for recombination in semiconductor lasers. Fig. 4.8 shows the Z -parameter versus current density, J , at 20°C and 55°C , for a 1^{st} and 2^{nd} generation sample. At threshold, the spontaneous emission clamps and the Z -parameter diverges to $+\infty$. The sharp kink in Z indicates threshold. The threshold densities are given in Table 4.1. Both samples lased at $1.46 \mu\text{m}$ at 20°C .

Table 4.1: Z -parameter and current distribution at threshold.

Operation Temperature	20°C		55°C	
	1^{st}	2^{nd}	1^{st}	2^{nd}
Generation				
Z_{th}	1.8	2.4	2.4	3.3
Monomolecular (A/cm^2)	620	150	750	160
Radiative (A/cm^2)	120	120	150	140
Leakage and/or Auger (A/cm^2)	360	360	850	800
Threshold (A/cm^2)	1100	630	1750	1100

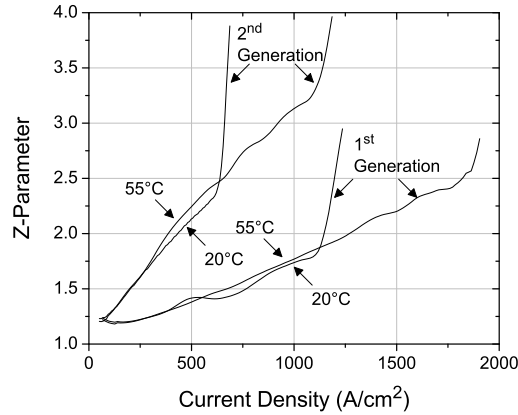


Figure 4.8: Z -parameter versus current density for 1st and 2nd generation samples at 20 °C and 55 °C.

Below 200A/cm², both devices at both operating temperatures are dominated by monomolecular recombination, however Z for the 1st generation sample remained below 1.5 beyond 650A/cm². At 20 °C, the threshold Z -parameter, Z_{th} , was 1.8 and 2.4 for the 1st and 2nd generation samples, respectively.

Carrier leakage in the form of recombination through barrier traps is highly temperature dependent. At 55 °C, the 2nd generation sample had $Z_{th}=3.3$, a clear indication that leakage or Auger recombination has become dominant, whereas the 1st generation sample had a lower value, $Z_{th}=2.4$, due to the larger amount of temperature-insensitive monomolecular recombination. As a result, the characteristic temperatures for threshold current, T_0 , and for efficiency, T_1 , were only 64K and 81K, respectively for the 2nd generation sample compared to 106K and 208K for the 1st generation sample.

For both samples, leakage causes Z to increase more rapidly with J at 55 °C compared to 20 °C. This change in slope of the Z - J curve is less pronounced for the 1st generation sample, again due to the larger amount of monomolecular recombination.

Table 4.1 also lists the approximate distribution of the threshold current at 20 ° C and 55 ° C, estimated from a qualitative comparison of the Z-J curve with the effective Z-parameter analysis in Chapter 3, the value of Z_{th} , and the temperature dependence of the recombination processes, described further in [93] and [95]. Both generations were found to have approximately the same threshold carrier density n_{th} (to be presented later in the RIN results in Section 4.4) and are therefore expected to have the same radiative and leakage/Auger current. We assume that the effective Z-parameter for leakage increases from 3.2 at 20 ° C to 3.9 at 55 ° C. From the analysis, we conclude that the great improvement in J_{th} and slight improvement in η_i for 2nd generation devices should be attributed to a reduction of monomolecular recombination.

4.3 Characteristic Temperatures

The method of characteristic temperatures utilizes a temperature dependent cavity length study to characterize the behavior of internal laser parameters. The method begins with the following laser equations, whose derivation is discussed more fully in [92, 103]:

$$g = g_0 L n \left(\frac{\eta_i J}{J_{tr}} \right) \quad (4.1)$$

$$J_{th} = \frac{J_{tr}}{\eta_i} \cdot \text{Exp} \left(\frac{\alpha_i + \alpha_m}{\Gamma \cdot g_0} \right) \quad (4.2)$$

$$\eta_e = \eta_i \cdot \frac{\alpha_m}{\alpha_i + \alpha_m} \quad (4.3)$$

where $\Gamma=1.4\%$ is the optical confinement factor, $\alpha_m=1/L \text{ Ln}(1/R)$ is the mirror loss, L is the cavity length, $R=30\%$ is the mirror reflectivity, g is the laser gain, J is the applied current density and the other parameters are defined in Table 4.2.

Table 4.2: Cavity length study parameters. The upper 2 parameters are extrinsic parameters since they depend on device size, whereas the lower 5 are intrinsic laser parameters.

Parameter	Description
J_{th}	Threshold Current Density
η_e	External Quantum Efficiency
g_0	Gain Coefficient
J_{tr}	Transparency Current Density
J_{th}^∞	Infinite Cavity Length Threshold
η_i	Internal Quantum Efficiency
α_i	Internal Loss

The temperature dependence of each parameter, x , in Table 4.2 is modeled by a local Arrhenius relation:

$$x(T) = x_0 \text{Exp} \left(\frac{\pm(T - T_{ref})}{T_x} \right) \quad (4.4)$$

where T is the temperature, T_{ref} is a reference temperature, and T_x and x_0 are the parameter's characteristic temperature and value at the reference temperature, respectively.

Low duty cycle pulsed L-I-V curves at $T_s=15-75^\circ\text{C}$ in 5°C steps were collected for $20\mu\text{m}$ wide 2^{nd} generation devices with three cavity lengths: 1050 , 1222 , and $2150\mu\text{m}$. Fig. 4.9 shows a set of L-I curves for a $2150\mu\text{m}$ device. For each temperature and cavity length, J_{th} and η_e were calculated from the L-I curve in the range of $4-12\text{mW}$. To reduce the effect of variance in these measured parameters on the derived values for g_0 , J_{tr} , J_{th}^∞ , η_i , and α_i , the measured parameters were first fitted to local Arrhenius relations. The fitted values were then used in the cavity length calculations, i.e. fitting Equations 4.2 and 4.3, at each temperature. Fig. 4.10 shows such a fit for the device

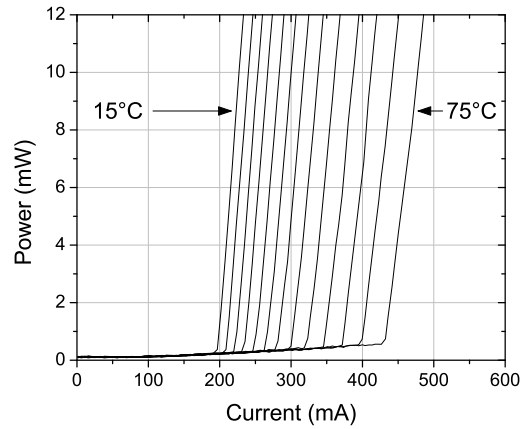


Figure 4.9: Pulsed L-I curves for a 2nd generation 20x2150 μ m laser at various temperatures.

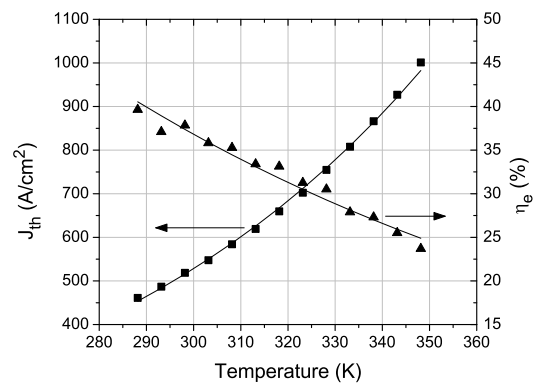
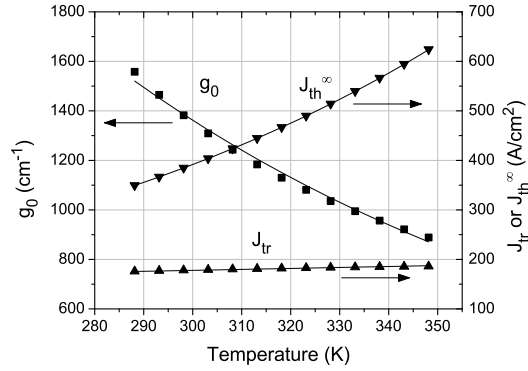
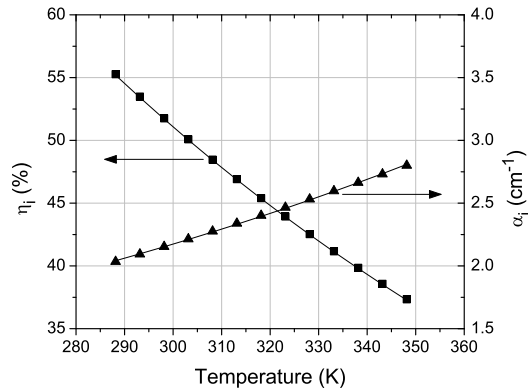


Figure 4.10: Temperature dependence of J_{th} and η_e for the laser of Fig. 4.9.

Figure 4.11: Temperature dependence of g_0 , J_{tr} , and J_{th}^{∞} .Figure 4.12: Temperature dependence of η_i and α_i .

depicted in Fig. 4.9. Both parameters are well modeled by their Arrhenius fit over the entire 60K temperature range.

Figs. 4.11 and 4.12 show the calculated values for g_0 , J_{tr} , J_{th}^{∞} , η_i , and α_i versus temperature and their corresponding Arrhenius fits. The Arrhenius parameters are tabulated in Table 4.3. The rapid decrease in g_0 is partly due to thermal broadening of the gain spectrum and increased occupation of higher quantized levels and contributes to the rapid rise in J_{th}^{∞} . Carrier leakage and/or Auger recombination can also affect

Table 4.3: Material and device parameters results for 2nd generation devices.

Parameter	Value at RT	Characteristic Temperature
g_0	$1440 \pm 40 \text{ cm}^{-1}$	$110 \pm 6 \text{ K}$
J_{tr}	$177 \pm 8 \text{ A/cm}^2$	$1000 \pm 800 \text{ K}$
J_{th}^∞	$366 \pm 9 \text{ A/cm}^2$	$104 \pm 5 \text{ K}$
η_i	$54 \pm 3 \%$	$153 \pm 15 \text{ K}$
α_i	$2.1 \pm 0.4 \text{ cm}^{-1}$	$188 \pm 80 \text{ K}$

g_0 . The increase in α_i is indicative of intervalence band absorption (IVBA) while the decrease in η_i is likely due to leakage/Auger recombination.

Measurement over a narrow 60K temperature range is insufficient to precisely determine the characteristic temperatures of weakly varying parameters, e.g. J_{tr} ; the error bars increase rapidly with the value. Nevertheless, using the data in Table 4.3, the cavity length dependence of the characteristic temperatures for J_{th} and η_e (T_0 and T_1 , respectively) can be accurately predicted according to [103]:

$$\frac{1}{T_0} = \frac{1}{T_{tr}} + \frac{\alpha_i}{\Gamma \cdot g_0} \frac{1}{T_{\alpha_i}} + \frac{\alpha_i + \alpha_m}{\Gamma \cdot g_0} \frac{1}{T_{g_0}} + \frac{1}{T_{\eta_i}} \quad (4.5)$$

$$\frac{1}{T_1} = \frac{\alpha_i}{\alpha_i + \alpha_m} \frac{1}{T_{\alpha_i}} + \frac{1}{T_{\eta_i}} \quad (4.6)$$

The terms on the right hand side of Equations 4.5 and 4.6 have been arranged in order of increasing influence on the temperature sensitivity of J_{th} and η_e . The temperature sensitivity of η_i is responsible for low values of T_0 and T_1 . In Fig. 4.7, the maximum CW output power occurred around 8.5x threshold. At this high bias, maintaining high efficiency as the device heats is critically important. If carrier leakage/Auger recombination can be reduced such that T_1 increases from 123K to 160K, P_{max} should increase by another 16% to over 500mW. The poor temperature performance of the

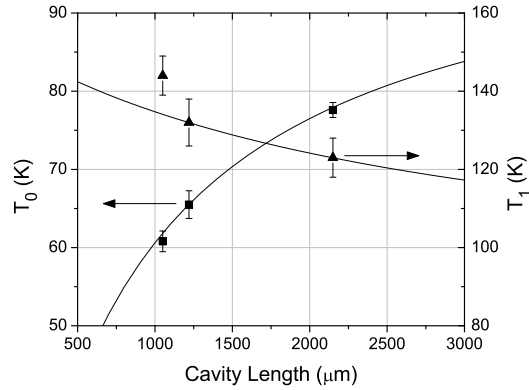


Figure 4.13: Cavity length dependence of T_0 and T_1 .

gain coefficient g_0 also limits T_0 . Values of T_0 around 85-90K are expected simply by applying an HR coating to the back facet of the $20 \times 2150 \mu\text{m}$ device. For comparison, typical values from the literature for T_0 are between 50-80K for InGaAsP lasers [43, 104] due to the relatively small conduction band offsets in that system.

The parameters T_0 and T_1 are expected to decrease slightly with temperature because of the temperature dependence of g_0 and α_i . The best prediction accuracy for T_0 and T_1 is obtained if the values for g_0 and α_i at the temperature midpoint of 45°C are used. Fig. 4.13 shows T_0 and T_1 and their predicted values as a function of cavity length.

4.4 Relative Intensity Noise (RIN)

4.4.1 Definition of RIN

Many intrinsic laser properties can be investigated through measurement of the relative intensity noise (RIN). The definition of laser RIN is the ratio of the mean square optical intensity deviation, in a 1 Hz frequency bandwidth, at a specified frequency f

and average optical power P_{avg} to the square of the average optical power,

$$RIN(dB/Hz) \equiv \frac{\langle \Delta P^2 \rangle}{P_{avg}^2} \quad (4.7)$$

Detector noise, such as thermal, shot or amplifier noise, is not included in the definition of laser RIN.

Low RIN is needed for a high signal-to-noise ratio for data transceivers. The signal-to-noise ratio at the detector is inversely proportional to the amount of noise in the detector bandwidth. The signal-to-noise ratio is given approximately by [105]:

$$\begin{aligned} SNR_{detector} &= \frac{m^2}{2B} \frac{1}{RIN} \\ m &\equiv \frac{P_{on} - P_{off}}{P_{on} + P_{off}} \end{aligned} \quad (4.8)$$

where m is the on-off modulation index, B is the detector bandwidth, the RIN is expressed in linear units per Hz, and P_{on} and P_{off} are the high and low optical power levels. Optical communications network usually require lasers with a RIN < 140dB/Hz.

4.4.2 RIN Analysis Theory

Gain versus carrier density is modeled by a linear relationship with nonlinear gain compression that reduces the gain as the cavity photon density, N , is increased:

$$g(n) = \frac{dg}{dn} \frac{(n - n_{tr})}{1 + \varepsilon N} \quad (4.9)$$

Under this assumption, the RIN spectrum can be derived from the carrier and photon rate equations, with Langevin noise sources [106], and expressed in the following form [107]:

$$RIN(W/Hz) = \frac{4}{\pi} \delta f_{ST} \frac{f^2 + (\gamma^*/2\pi)^2}{(f_r^2 - f^2)^2 + f^2(\gamma/2\pi)^2} \quad (4.10)$$

Table 4.4: Relative intensity noise study parameters. The upper 6 parameters are extrinsic parameters; the lower 5 are intrinsic parameters.

Parameter	Description
f_r	Resonance Frequency
γ	Damping Coefficient
P	Front Facet Output Power
D	Slope of f_r versus \sqrt{P}
K	Slope of γ versus f_r^2
n_{th}	Threshold Carrier Density
n_{tr}	Transparency Carrier Density
dg/dn	Differential Gain
γ_0	Threshold Damping Coefficient
τ_e^{th}	Threshold Differential Lifetime
ε	Nonlinear Gain Compression

where δf_{ST} is the Schawlow-Townes linewidth, f_r is the resonance frequency, γ is the damping factor, while γ^* in the numerator is the exact damping factor including the non-linear gain. The RIN spectrum is roughly centered at the resonance frequency, the damping coefficient γ affects the width, and Schawlow-Townes linewidth sets the amplitude. These parameters and other parameters characterized in the RIN analysis are listed in Table 4.4. Of the four intrinsic parameters extracted by Equation 4.10, the least accurately determined is γ^* because of its weak effect on the RIN spectrum.

The overall RIN level decreases and the frequency and width of the RIN peak increases with current or output power. The resonance frequency increases linearly with the square root of the output optical power and the D parameter is defined as the slope of this relationship [106, 108]

$$f_r = D\sqrt{P}$$

$$D^2 = \frac{\Gamma \frac{dg}{dn} v_g}{4\pi^2 V_a(h\nu)} \frac{\alpha_i + \alpha_m}{\alpha_m} \left[1 + \left(\frac{1-R_r}{1-R_f} \right) \sqrt{\frac{R_f}{R_r}} \right] \quad (4.11)$$

where P is the front facet output power, Γ is the optical confinement factor, dg/dn is the differential gain, v_g is the group velocity, V_a is the active volume, $h\nu$ is the photon energy, α_i and α_m are the internal and mirror losses, R_r and R_f are the rear and front mirror reflectivities. The term in brackets represents the ratio of the total power to the front facet power and has a value of 2 for uncoated devices and is approximately 1 for our cleaved/HR devices. Large D values are desired for high-speed devices; however, it is the differential gain that is a more important figure of merit since it is an intrinsic material parameter. The differential gain can be solved for in terms of D by inverting 4.11.

Two other parameters that can be extracted from the RIN analysis are the K factor and the threshold damping coefficient γ_0 . The damping coefficient γ increases with a square of the resonance frequency; the K factor and γ_0 are defined as [106].

$$\gamma = K f_r^2 + \gamma_0 \quad (4.12)$$

The maximum modulation 3dB (optical) laser bandwidth is inversely proportional to K [106].

$$f_{3dB,max}^o = \sqrt{2} \frac{2\pi}{K} \approx \frac{8.9}{K} \quad (4.13)$$

Thus, high-speed transceivers require small values of K . Since the electrical signal is proportional to the square of the optical intensity, this 3dB optical bandwidth corresponds to a 6dB electrical bandwidth at the detector. The K factor increases with the average photon lifetime in the cavity τ_p :

$$K = 4\pi^2 \tau_p \left(1 - \Gamma \frac{dg}{dN} / \frac{dg}{dn}\right) = 4\pi^2 \left(\tau_p + \frac{\varepsilon}{v_g \frac{dg}{dn}}\right) \quad (4.14)$$

$$\tau_p = \frac{1}{v_g(\alpha_i + \alpha_m)}$$

where N is the photon density, dg/dN is the nonlinear gain, and ε is the nonlinear gain compression coefficient. Using a device with a short photon lifetime, i.e. a short cavity with an AR coated output facet, in a material system with a high differential gain to nonlinear gain compression ratio can reduce K and increase the modulation bandwidth.

The threshold damping coefficient γ_0 in Equation 4.12 is given by [95, 106]:

$$\begin{aligned}\gamma_0 &= \frac{\Gamma R_{sp}}{V_a N} + \frac{d}{dn} R(n) \\ \frac{1}{\tau_e} &= \frac{dR}{dn}\end{aligned}\tag{4.15}$$

where R_{sp} is the spontaneous emission rate, n is the carrier concentration, and τ_e is the differential carrier lifetime. Typically, the portion of the linear fit used to obtain K and γ_0 is sufficiently above threshold that we can neglect spontaneous emission and so $\tau_e \approx 1/\gamma_0$.

4.4.3 Measurement of RIN

The RIN measurement setup details are discussed in Appendix C. The RIN spectra at several currents of an uncoated $10 \times 1222 \mu\text{m}$ 2nd generation device were measured at various temperatures for comparison with a previous room temperature report of a cleaved/HR $10 \times 750 \mu\text{m}$ 1st generation device [94]. Since the device geometry and facet coating is different, comparisons should only be made regarding intrinsic parameters. Fig. 4.14 shows a room temperature RIN spectrum on a linear scale and its theoretical fit. The fit determines f_r and γ at each current and temperature. Fig. 4.15 displays the RIN spectra at various currents on a log scale.

The f_r versus \sqrt{P} and γ versus f_r^2 plots for two temperatures are displayed in Figs. 4.16 and 4.17. Notice that the one parameter linear fit in Fig. 4.16 must pass through the origin. The D-parameter decreases from 0.74 to 0.59 GHz/mW^{0.5} as the

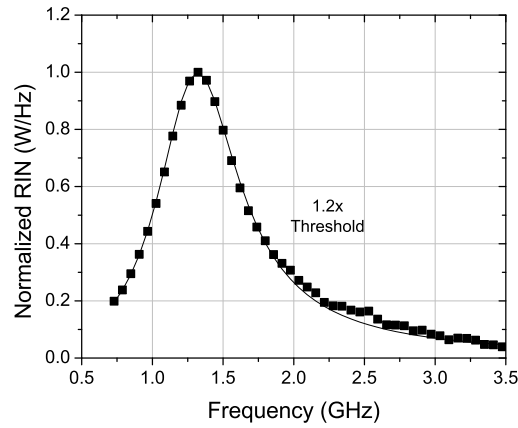


Figure 4.14: RIN spectrum (linear-scale) and its fit for a 2^{nd} generation $10 \times 1222 \mu\text{m}$ laser at $1.2xI_{th}$ at room temperature.

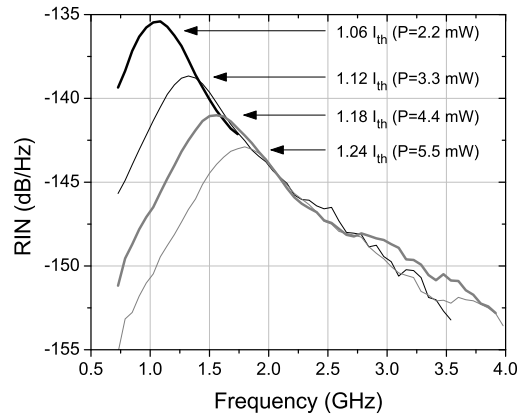


Figure 4.15: RIN spectrum (log-scale) for various currents for the laser of Fig. 4.14.

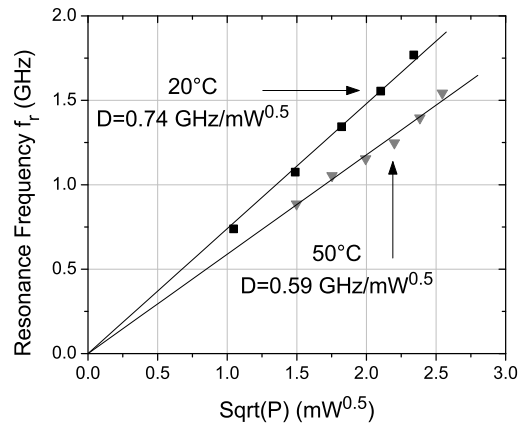


Figure 4.16: Resonance frequency vs square root of optical power for the laser of Fig. 4.14.

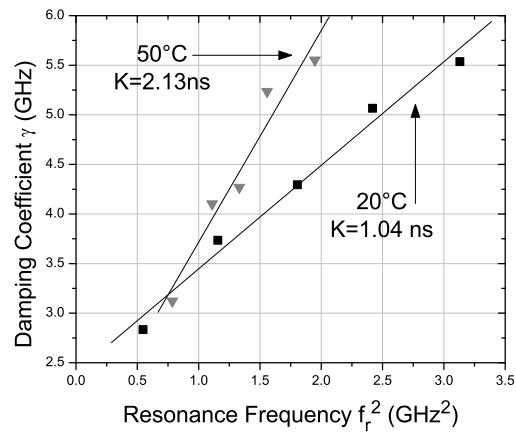


Figure 4.17: Damping coefficient vs resonance frequency squared for the laser of Fig. 4.14.

temperature is increased from RT to 50 ° C, while the K-parameter increases from 1.04 to 2.13ns, which causes the maximum 3dB modulation bandwidth to decrease from 8.5 to 4.2GHz. These values are unsatisfactory for direct modulation applications in most of today's optical communication networks. However, they are still pretty good considering the large device size.

At RT, we determined $dg/dn=9.2 \times 10^{-16} \text{cm}^2$, $\varepsilon=1.4 \times 10^{-16} \text{cm}^3$, and $\tau_e^{th}=0.4 \pm 0.1 \text{ns}$ for 2nd generation devices from the D and K parameters. The results for 1st generation devices were $dg/dn=1.2 \times 10^{-15} \text{cm}^2$, $\varepsilon=1.2 \times 10^{-16} \text{cm}^3$, and $\tau_e^{th}=3 \pm 2 \text{ns}$. The intrinsic material parameters, dg/dn and ε are quite similar in the two generations of devices. Inaccuracy in determining γ_0 , and therefore τ_e^{th} , was too large in the 1st generation of devices to be able to compare the threshold differential carrier lifetimes of the two device generations.

Large differential gain is a crucial element in achieving low threshold, high T_0 , and high power lasers. For equal confinement factors and total losses, threshold can be obtained at lower values of carrier concentration. This reduces Auger recombination, which scales as n^3 , and may reduce the temperature sensitivity of the threshold current. Or, a larger waveguide with a smaller optical confinement factor Γ , but the same total gain can be fabricated. This increases the power limitations of catastrophic optical mirror damage (COMD) and thereby allows higher output powers.

The GaInNAsSb/GaAs value at RT for dg/dn at $1.5 \mu\text{m}$ is comparable to the value of $1.06 \times 10^{-15} \text{cm}^2$ in GaInNAsSb/GaAs lasers at $1.26 \mu\text{m}$ [109] and is significantly higher than $5-7 \times 10^{-16} \text{cm}^2$ and $2-8 \times 10^{-16} \text{cm}^2$ for multiple quantum well (MQW) InGaAsP/InP lasers at $1.3 \mu\text{m}$ [107] and $1.55 \mu\text{m}$ [106]. It is approaching the enormous gain observed in non-gain-saturated, InGaAs/GaAs multiple quantum multiple quantum well lasers at $0.9-1.1 \mu\text{m}$ [110]. The huge value for GaInNAsSb at $1.5 \mu\text{m}$ is attributed to the increased compressive strain ($\approx 2.5\%$) in the QW. At RT,

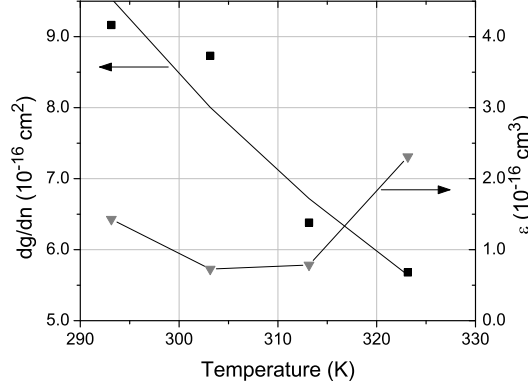


Figure 4.18: Temperature dependence of dg/dn and ϵ for the laser of Fig. 4.14.

$n_{tr}=2.1 \times 10^{18} \text{ cm}^{-3}$ was measured and also calculated from the device band structure [74]. Equating gain to total loss at threshold, we obtain $n_{th} \approx 2.8\text{-}3.6 \times 10^{18} \text{ cm}^{-3}$ for both generations of devices, depending on the exact device length.

The temperature dependence of dg/dn and ϵ for 2nd generation devices are plotted in Fig. 4.18. Except for dg/dn , the factors on the right side of Equation 4.11 have very weak temperature dependence. The characteristic temperature of dg/dn was 57K, which was very close to the measured T_0 of 64K. The temperature dependence of the differential gain dictates the temperature dependence of the threshold carrier density and thereby limits the characteristic temperature for current density, T_0 .

Due to the uncertainties in the fit parameters, especially γ , the temperature dependence of ϵ was unclear; however, its room temperature value of $1.4 \times 10^{-16} \text{ cm}^{-3}$ is about 2x larger than for MQW $\text{In}_{0.35}\text{Ga}_{0.65}\text{As}$ lasers at 1080nm [110]. This large non-linear gain compression coefficient is probably due to strong inhomogeneous broadening, i.e. spectral hole burning within the energy bands, and greatly restricts additional stimulated emission at a given wavelength. As additional current is injected, the power increases in adjacent longitudinal modes where the gain is less saturated, thereby broadening the spectrum at higher power. Previously, we observed that the peak

intensity saturated quickly and the spectrum broadened significantly with bias in Fig. 4.2.

The strong spectral hole burning may be related to the previously observed weak clamping of the carrier density above threshold discussed in Section 3.4. If injected carriers can scatter rapidly into the portions of the bands that are getting depleted by the main lasing modes, spectral hole burning would be mitigated. As a result, ε would be reduced and the carrier density would clamp strongly at threshold.

4.5 Reliability of High Power Lasers

A reliability study at high power operation for 2nd generation devices was conducted for comparison with the 1st generation results presented in Section 3.6. An unpackaged 20x2150 μ m device operated at a constant CW output power of 200mW for nearly 500 hours with less than a 13% increase in operation current, I_{op} . See Fig. 4.19. The small jumps in operation correspond to changes in the ambient lab environment during the workday. The stage is cooled to $T_s=0^\circ\text{C}$ so that the active region temperature is close to RT during operation and the sample is probed at five locations.

The reliability of 2nd generation devices is greatly enhanced compared to 1st generation devices, where I_{op} increased by 70% after only 50 hours of operation at 10mW and $T_s=15^\circ\text{C}$ ($T_a \approx 30^\circ\text{C}$). It was argued [74] that high levels of monomolecular recombination might enhance defect propagation by providing thermal energy during life testing. Also, through Z -parameter measurements, it was concluded that the primary source of device degradation of 1st generation devices was an increase in recombination through defects, especially the (N-N)_{As} split interstitial. Thus, the vast improvement in reliability is also attributed to reduced monomolecular recombination.

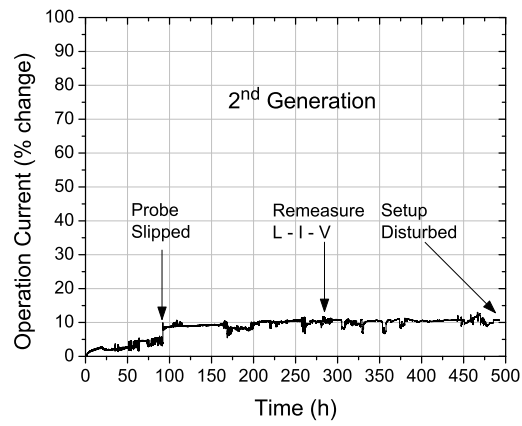


Figure 4.19: Time evolution of I_{op} and V_{op} at 200mW CW output from a $20 \times 2150 \mu\text{m}$ 2nd generation laser.

Chapter 5

Laser Modeling

5.1 Current-Voltage Characteristics

Significantly more attention is paid to L-I compared to I-V characteristics in laser measurements. However, dissipated electrical power is an important design consideration. Appropriate doping profiles must be chosen to maximize the tradeoff between the free carrier absorption and series resistance of the cladding and waveguide layers. Also, the I-V characteristics need to be modeled as a function of device geometry and temperature to minimize device heating.

The current flowing through the laser, I , as a function of the applied voltage, V , is given by the ideal diode equation modified for series resistance and non-ideality:

$$I = I_0 \left[\text{Exp} \left(\frac{q(V - IR_s)}{nk_B T_a} \right) - 1 \right] \quad (5.1)$$

where I_0 is the reverse bias saturation current, k_B is Boltzmann's constant, T_a is the active region temperature, $n \approx 1-2$ is the ideality factor and R_s is the series resistance. The transcendental equation for the current can be inverted to express the voltage as a function of current:

$$V = IR_s + \frac{nk_B T_a}{q} \text{Ln} \left(1 + \frac{I}{I_0} \right) \quad (5.2)$$

In forward bias, $I \gg I_0$ and Equation 5.2 becomes:

$$V \approx IR_s + \frac{nk_B T_a}{q} \ln(I) + V_0 \quad (5.3)$$

$$V_0 = -\frac{nk_B T_a}{q} \ln(I_0) \quad (5.4)$$

By making this separation, the value of V_0 and its interpretation depends on the units of the current and so we take the convention that the current is expressed in Amps. According to this definition, V_0 represents the voltage drop across the junction ($R_s=0$) for 1A of current. This voltage should equal the quasi-Fermi level separation at that bias.

A linear plot of $I \cdot dV/dI$ versus $1/I$ can be used to extract the series resistance and the ideality factor:

$$I \frac{dV}{dI} = R_s + \frac{nk_B T_a}{q} \frac{1}{I} \quad (5.5)$$

with the caveat that data for $I=0$ needs to be removed first. The value of V_0 can be solved for as the average residual:

$$V_0 = V - IR_s - \frac{nk_B T_a}{q} \ln(I) \quad (5.6)$$

Slight improvements to the overall fit of Equation 5.3 can be made with non-linear curve fitting using these determined values as the initial fit parameters. Since T_a appears in these equations, heating effects need to be minimized for accurate interpretation of the results. Pulsed measurements generally have too many transients in the I-V waveforms and so the best results arise from analysis of the low bias region of CW I-V curves where $T_a \approx T_s$.

The values of n , R_s , and V_0 were measured as a function of temperature and device size for 1st and 2nd generation devices, but we will focus primarily on 2nd

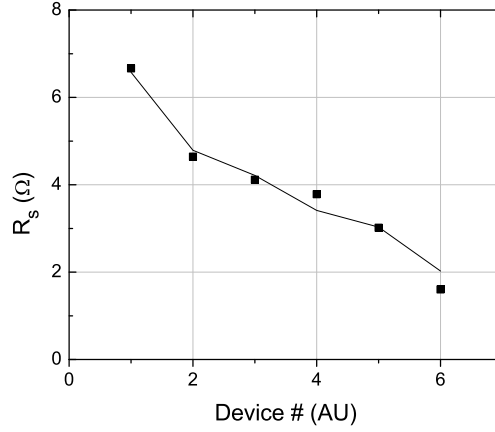


Figure 5.1: Series resistances for six devices of varying length and width and the fitted series resistance of Equation 5.7. The line serves as a guide for the eyes.

generation devices. No trend was observed in the ideality factor with device area or temperature. An average value of $n=1.8\pm 0.2$ was determined. The other two parameters were found to depend on both temperature and size.

The measured series resistance is composed of contact resistance, mesa resistance, layer resistances and cable resistance. The layer resistances include the un-doped waveguide, n-AlGaAs cladding layer below, substrate, and solder resistances, each of which are assumed to be inversely proportional to device length, L , but roughly independent of device mesa width, w . The dependence of R_s on device geometry and number of probe contacts, n_c , is modeled by:

$$R_s = \frac{R_c}{n_c} + R_{mesa} \frac{L_{ref} w_{ref}}{Lw} + R_{layer} \frac{L_{ref}}{L} + R_{cable} \quad (5.7)$$

where R_c is the contact resistance per probe, $L_{ref}=1000\mu\text{m}$ is the reference length, $w_{ref}=10\mu\text{m}$ is the reference width, R_{mesa} is the mesa resistance for a $10\times 1000\mu\text{m}$ device, R_{layer} is the effective layer resistance for a $1000\mu\text{m}$ long device, and R_{cable} is the cable resistance. A value of $R_c=1.06\pm 0.39\Omega$ was previously determined in Section 4.1

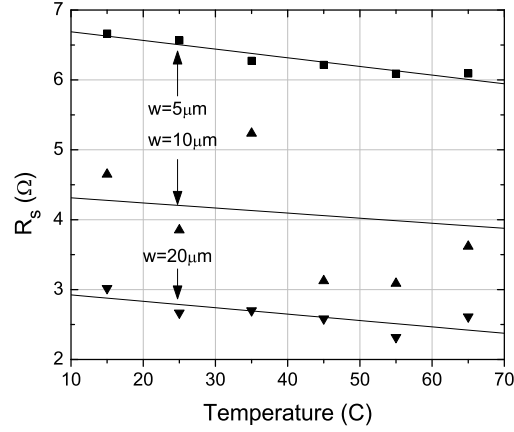


Figure 5.2: Series resistances versus temperature for a 5, 10, and $20\mu\text{m}$ wide stripe of length $1222\mu\text{m}$.

by measuring R_s while varying the number of contact probes for a $20\times 2150\mu\text{m}$ device. Note that different probes may produce different values of R_c due to variations in the angle of contact and cleanliness of the tip. A value of $R_{cable}=0.35\pm 0.13\Omega$ was determined by measuring the resistance with the probes shorted to the copper heatsink. By performing a two-parameter regression to the residual after the contact and cable resistances are subtracted, we determined $R_{mesa}=2.89\pm 0.28\Omega$ and $R_{layer}=1.41\pm 0.30\Omega$ at 15°C . Fig. 5.1 shows the series resistance for devices with six different combinations of length and width and the calculated series resistance of Equation 5.7. Reasonably good agreement is achieved.

Fig. 5.2 shows R_s versus temperature for a 5, 10, and $20\mu\text{m}$ wide stripe of length $1222\mu\text{m}$. The weak temperature dependence of R_s appears to be independent of mesa width and an average value of $dR_s/dT=-11.0\pm 1.6\text{m}\Omega/\text{K}$ is determined. We will attribute this temperature dependence to R_{layer} ($dR_{layer}/dT=13.4\pm 2.0\text{m}\Omega/\text{K}$) although there is no a priori reason that R_{mesa} should not also be affected. In summary, the

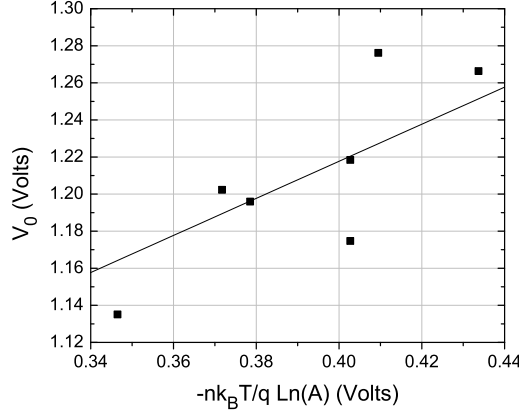


Figure 5.3: V_0 versus $-nk_B T/q \cdot \ln(A)$ at 15 ° C.

series resistance in Ohms is given by:

$$R_s = \frac{1.06}{n_c} + \frac{2.89 \cdot 10^4}{Lw} + \frac{(1.41 - 0.0134 \cdot (T_a - 15^\circ C)) \cdot 10^3}{L} + 0.35 \quad (5.8)$$

for R_s in ohms, L and w in μm , and T_a in degrees Celsius. The first three terms will cause junction heating, whereas, the cable acts as a resistor in series with the laser that only serves to add to the measured voltage.

The voltage V_0 is important for determining the temperature dependence of the I-V characteristics. The increase of I_0 with temperature is sufficiently rapid that V_0 decreases. This decrease of V_0 can also be understood by arguing that the quasi-Fermi level separation needed to maintain a fixed current decreases with temperature. To characterize V_0 , we begin by analyzing the dependence on device area. Since I_0 is proportional to area, we re-express V_0 as:

$$V_0 = -\frac{nk_B T_a}{q} \ln(J_0 A) = -\frac{nk_B T_a}{q} \ln(J_0) - \frac{nk_B T_a}{q} \ln(A) \quad (5.9)$$

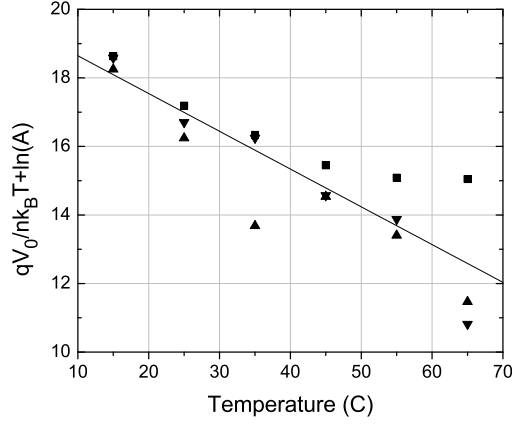


Figure 5.4: $qV_0/nk_B T + \ln(A)$ versus temperature for the 5, 10, and $20\mu\text{m}$ wide stripe of length $1222\mu\text{m}$.

where J_0 is the reverse bias saturation current density in units of A/cm^2 , since A has units of cm^2 . Fig. 5.3 is a graph of V_0 versus $-nk_B T/q \cdot \ln(A)$ at 15°C . The linear fit has a fixed slope of unity and only the offset is adjustable. The value for the offset was $0.818 \pm 0.012\text{V}$, which implies a value of $J_0 = 11 \pm 18\text{nA}/\text{cm}^2$ at 15°C . The enormous error bars arise from exponentiation of a large negative number that has reasonably sized error bars due to the uncertainty in the ideality factor. Thus, we shall perform fits for V_0 or $\ln(J_0)$ rather than J_0 directly. Rearranging Equation 5.9, we have:

$$-\ln(J_0) = \frac{qV_0}{nk_B T_a} + \ln(A) \quad (5.10)$$

The right hand side of Equation 5.10, for the 5, 10, and $20\mu\text{m}$ wide stripes of length $1222\mu\text{m}$ from Fig. 5.2, is plotted as a function of stage temperature in Fig. 5.4. It is approximated by a linear relationship with intercept 18.09 ± 0.42 and slope 0.11 ± 0.01 :

$$-\ln(J_0) = 18.09 - 0.11 \cdot (T_a - 15^\circ\text{C}) \quad (5.11)$$

Unlike Equation 5.8, we use T_a here instead of T_s , since the saturation current density should depend on active region temperature. Using Equations 5.3, 5.8, 5.9 and 5.11, we can calculate the temperature and device geometry dependence of the applied voltage; however we can only expect valid results when T_a ranges between 15 and 75 °C.

5.2 Thermal Resistance

Accurate measurements of the thermal resistance, R_{th} , of the laser are needed to model device heating and CW laser performance. A simple and accurate technique to determine the active region temperature is to measure the bandgap redshift with temperature. The peak wavelength, λ_p , and the center (average) of the half-maximum wavelengths, λ_c , of the amplified spontaneous emission are used as markers. The spectra are collected for a variety of currents in pulsed mode (1 μ s, 1% duty cycle to prevent heating) from 15-75 °C stage temperature in 5 °C steps. The redshift of each marker wavelength, usually about 0.58nm/K (0.34meV/K), is recorded for each bias. Next, the CW spectra are collected at the same current levels. Using the marker data of the CW spectra, the active region temperature is interpolated by inverting the temperature dependence of the pulsed marker data at that bias. The thermal resistance can then be calculated by dividing the temperature rise by the dissipated electrical power in the device. The dissipated power is equal to the total power ($I \cdot V$) minus the optical power and the electrical power dissipated in the solder and cables. Measurement accuracy is improved by averaging the resistances calculated at the various bias levels and for both marker datasets. Below threshold, λ_p is a less stable thermometer than λ_c due to the flat gain peak. However, above threshold, λ_c is not used because it cannot be defined for multimode spectra. Interestingly, λ_p becomes

very accurate above threshold, except in some cases where mode hopping ($\approx 1-3\text{nm}$) produces variation in the calculated temperature (2-5K).

This procedure was repeated for CW spectra from 15 to 45 °C in 5 °C steps for the 5, 10, and 20 μm wide stripes for a 983 μm long 1st generation HR coated sample, with a wafer thickness of 120 μm , to obtain the temperature dependence of R_{th} . Any temperature dependence was hidden in the measurement noise. The thermal resistances for the three stripe widths were $R_{th}=41.5\pm 1.8$, 37.8 ± 1.4 , and $30.8\pm 0.6\text{K/W}$, respectively. It is very important to remember that these are the thermal resistances from the active region to the thermistor. The heat must traverse the 38 μm thick solder (See Appendix B) and about 2mm in the copper heatsink to reach the thermistor. Thus, R_{th} also includes a small, but non-negligible contribution due to the thermal resistance of the solder and copper heatsink.

The results of two models for the thermal resistance of a line source of length, L , and width, w , on a much wider substrate with thickness, t , and thermal conductivity, κ , are [111]:

$$R_{th} \approx \frac{Ln(4t/w)}{\pi\kappa L} \quad (5.12)$$

which is only valid for $w \ll t$ and [112]:

$$R_{th} = \int_0^t \frac{dz}{\kappa L(w + 2zTan(\alpha))} = \frac{1}{2Tan(\alpha)\kappa L} Ln\left(\frac{w_f}{w}\right) \quad (5.13)$$

$$w_f = w + 2tTan(\alpha) \quad (5.14)$$

which uses the constant heat spreading angle assumption. Typically, the heat spreading is assumed to be isotropic ($\alpha=45^\circ$). Both models assume that the heat can spread in the lateral and vertical directions and that device geometry precludes significant spreading in the longitudinal direction. For $w \ll t$, the models have a similar logarithmic dependence on device width and inverse proportionality to device length, but

are slightly inconsistent no matter what value of α is used due to the difference in the constants. The model of Equation 5.13 is more general and reproduces the simple 1-d columnar heat flow result:

$$R_{th} = \frac{1}{2Tan(\alpha)\kappa L} Ln\left(1 + \frac{2tTan(\alpha)}{w}\right) \approx \frac{t}{\kappa Lw} \quad (5.15)$$

in the limit that $t \ll w$. It also gives a better fit to our empirical data after including the thermal resistance of the solder and copper. Let $t_{sub}=120\mu\text{m}$, $\kappa_{sub}=0.55\text{W}/(\text{cm K})$, $t_{solder}=38\mu\text{m}$, and $\kappa_{solder}=0.34\text{W}/(\text{cm K})$ denote the substrate thickness and conductivity and solder thickness and conductivity, respectively. Let $t_c=2\text{mm}$ and $\kappa_c=3.98\text{W}/(\text{cm K})$ denote the distance in the copper to the thermistor and the copper heatsink conductivity. Fix $\alpha=45^\circ$, i.e. no remaining free fit parameters. Noting that $w_f=w+2t_{sub}$ at the substrate/solder interface, $w_f=w+2t_{sub}+2t_{solder}$ at the solder/heatsink interface, and $w_f=w+2t_{sub}+2t_{solder}+2t_c$ at the heatsink/thermistor interface, we find:

$$R_{th} = \frac{1}{2\kappa_{sub}L} Ln\left(\frac{w+2t_{sub}}{w}\right) + \frac{1}{2\kappa_{solder}L} Ln\left(\frac{w+2t_{sub}+2t_{solder}}{w+2t_{sub}}\right) + \frac{1}{2\kappa_cL} Ln\left(\frac{w+2t_{sub}+2t_{solder}+2t_c}{w+2t_{sub}+2t_{solder}}\right) \quad (5.16)$$

Fig. 5.5 is a plot of the width dependence of the thermal resistance for the $983\mu\text{m}$ sample and the graph of Equation 5.16. Excellent agreement is observed without any free parameters, validating the theoretical model. The temperature dependence of R_{th} , if any, can be modeled, provided that the temperature dependence of the thermal conductivities of the three materials are known.

Fig. 5.6 shows the individual contributions of the substrate, solder, and heatsink to the total thermal resistance on a logarithmic scale. The thermal resistance of the substrate is about 10x larger than that of the solder or heatsink and determines the width dependence of R_{th} . The solder and heatsink thermal resistances are around

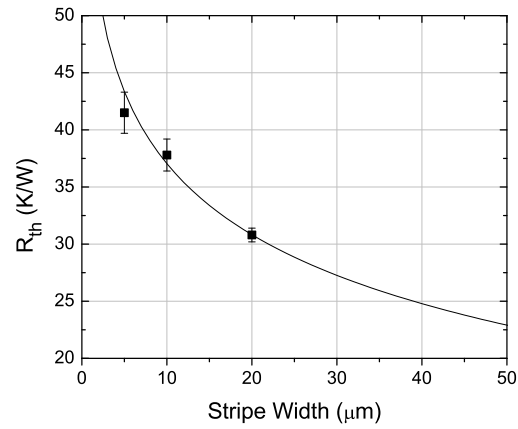


Figure 5.5: R_{th} versus mesa stripe width and the theoretical prediction (no free fit parameters) of Equation 5.16 for a $983\mu\text{m}$ long sample.

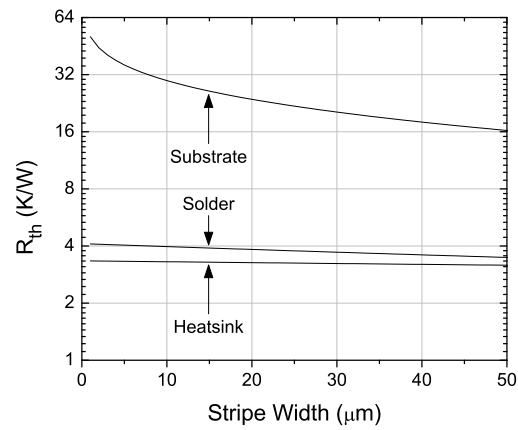


Figure 5.6: Individual contributions of the substrate, solder, and heatsink to R_{th} (log-scale) versus mesa stripe width for a $983\mu\text{m}$ long sample.

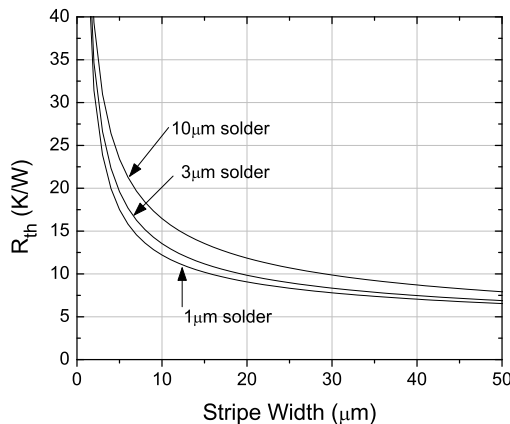


Figure 5.7: Simulation of R_{th} versus mesa stripe width for a $983\mu\text{m}$ long sample mounted epi-down to a copper heatsink for 1, 5, and $10\mu\text{m}$ thicknesses of ^{100}In solder.

3-4K/W each. After traversing the substrate, the heat spreading width ($\approx 120\mu\text{m}$) is much larger than the device width and so the subsequent thermal resistances, i.e. for the solder and the heatsink, become relatively independent of the initial stripe width.

Fig. 5.7 is a simulation of the width dependence of R_{th} for the $983\mu\text{m}$ sample if the device were mounted epitaxial side down to a copper heatsink using ^{100}In solder ($\kappa_{solder}=0.86\text{W}/(\text{cm K})$) of 1, 5, and $10\mu\text{m}$ thicknesses. We ignore the small effect of the change in conductivity for the AlGaAs cladding and instead use the value for GaAs throughout and continued to assume that $t_c=2\text{mm}$. There is a 2-3x reduction in R_{th} for epi-down compared to epi-up mounting. The improvement is less pronounced for very narrow widths. The width dependence saturates more quickly because of the change in width dependence for 1-d compared to 2-d heat flow. The thermal resistance is not significantly affected by the solder thickness. In epi-down mounting, 1-d columnar flow must be used for the mesa, which has height $2\mu\text{m}$, and the width can only spread in the solder and heatsink. Reduced R_{th} can be achieved by planarizing the mesas with high conductivity material, enabling immediate 2-d heat flow. However, readily available dielectric planarization materials have poor thermal

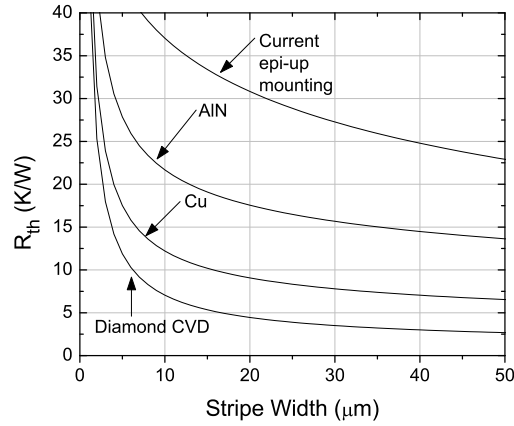


Figure 5.8: Simulation of R_{th} versus mesa stripe width for a $983\mu\text{m}$ long sample for our current epi-up mounting and for epi-down mounting to AlN, Cu, and diamond CVD heatsinks using a $1\mu\text{m}$ thickness of ^{100}In solder.

conductivities, e.g. BCB ($\kappa=0.007\text{W}/(\text{cm K})$). Novel materials, such as diamond filled polyimide may enable more significant gains. Also, increasing the cavity length will lower R_{th} even further since they are inversely proportional.

Fig. 5.8 is a comparison of the thermal resistance of our current epi-up mounting to that of epi-down mounting using a $1\mu\text{m}$ thick ^{100}In solder for three heatsink materials: AlN ($\kappa_c=1.75\text{W}/(\text{cm K})$), Copper ($\kappa_c=3.98\text{W}/(\text{cm K})$), and polycrystalline diamond ($\kappa_c=13\text{W}/(\text{cm K})$) grown by chemical vapor deposition (CVD). Note that it will not actually be possible to bond epi-down to a copper heatsink and still be able to individually address laser stripes since copper is electrically conducting. Significant reductions in R_{th} of another factor of 2 compared to copper are possible by using CVD diamond heatsinks. These heatsinks are not so incredibly expensive; only \$20 for an un-patterned $400\mu\text{m}$ thick, $3.2\times 3.2\text{mm}$ square sample polished to $<300\text{\AA}$, which can be laser diced into sixteen squares of size $800\times 800\mu\text{m}$ resulting in an individual laser heatsink cost of \$1.25. Lower R_{th} will significantly increase P_{max}^{CW} , the maximum CW output power, and improve the thermal stability allowing uncooled operation

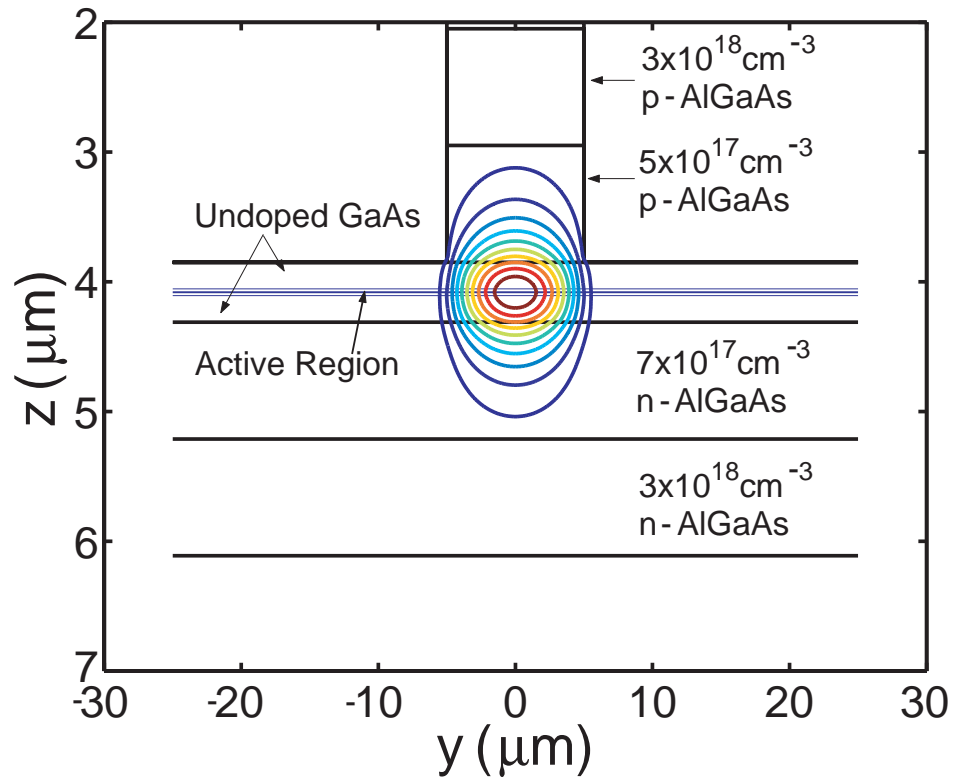
and possibly justifying the added cost. Epi-down bonding to the CVD diamond plus substrate bonding to copper would only be slightly more expensive and would further reduce R_{th} by creating heat flow paths in opposite directions that act in parallel.

5.3 Waveguide Simulations

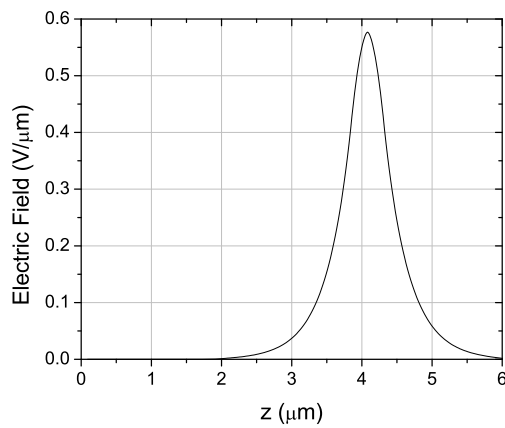
The optical confinement factor and the electric field profile for the ridge waveguide separate confinement heterostructure were calculated in Matlab using mode solver written by V. Sabnis and modified by L. Scaccabarozzi. Fig. 5.9a shows the contours of constant E-field magnitude in 10% steps for a $10\mu\text{m}$ wide stripe. The $1/e^2$ diameter for the intensity ($1/e$ for the E-field) is $0.937\mu\text{m}$ vertically and $8.25\mu\text{m}$ horizontally as shown in the cross-sectional views of Figs. 5.9b and 5.9c, respectively. The optical confinement factor for the 8nm SQW was 1.43% and the effective mode index is $n_e=3.30$. Since the fundamental mode has an anti-node, i.e. is flat, at the active region, the optical confinement factor increases linearly with thickness at a rate of $0.18\%/nm$ for small active region thicknesses ($<40nm$).

From the simulations, we determined that multiple modes would be supported if the GaAs waveguide thickness, d , exceeds $0.75\mu\text{m}$ or the ridge width, w , exceeds $1.9\mu\text{m}$. However, in practice higher order horizontal modes suffer larger diffractive loss and the second order vertical mode has a node at the active region and so single transverse mode operation still occurs in much larger waveguides. Multiple Fabry-Pérot peaks corresponding to longitudinal modes are visible in the spectra.

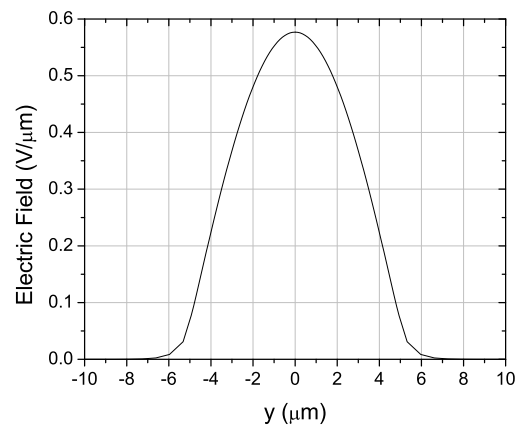
Three new additions to the program are that the free carrier absorption (FCA), electrical series resistance of the mesa, and thermal resistances can be calculated if the doping profile is loaded along with the layer composition profile. For the $10\times 1000\mu\text{m}$ sample, we calculated $\alpha_{FCA}=1.0\text{cm}^{-1}$, $R_{mesa}=2.4\Omega$, and $R_{th}=41\text{K/W}$. The FCA loss



(a)



(b)



(c)

Figure 5.9: (Color) Waveguide simulations for a $10\mu\text{m}$ wide ridge. (a) Contours of constant E-field magnitude in 10% steps. (b) and (c) cross-sectional views of the E-field profile.

and mesa resistance are consistent with the cavity length measurements for the internal loss and the best-fit value of $R_{mesa}=2.89\Omega$ from Section 5.1. The simulated thermal resistance is a bit higher than the 37K/W predicted by Equation 5.16 because the decrease in thermal conductivity of $Al_{0.3}Ga_{0.7}As$ compared to GaAs was included here. The series resistance in the p-side GaAs waveguide dominates the mesa resistance since this region is un-doped and the mobility of holes is less than that of electrons. With increasing bias, R_{mesa} is expected to decrease as excess free carriers reduce the waveguide resistivity.

Future research in these simulations should include modeling of the carrier densities throughout the structure (especially in the waveguide region) as a function of injected current density. Also, optimization of the doping profile and layer thickness to minimize resistances without increasing the free carrier absorption and decreasing the optical confinement factor should be studied.

5.4 Macroscopic Modeling

With the intrinsic electrical and optical parameters and their temperature dependence characterized, simulations of device performance for various geometries can be simulated. Fig. 5.10a shows a simulation of the L-I-V curves and typical experimental data for a $10\times 1222\mu m$ device at $15^\circ C$. There is excellent agreement between the data and the simulation. Fig. 5.10b shows a simulation of the L-I-V curves and experimental data from the best performing $20\times 1222\mu m$ device at $20^\circ C$. There is decent agreement between the data and the simulation with regards to threshold current and to a lesser extent for external quantum efficiency, however the curves generally do not agree far above threshold. It appears that this device had about 0.5Ω less series resistance than typical devices its size, possibly in part due to reduced contact resistance. Also, the external efficiency was a few percent better. For a fixed device

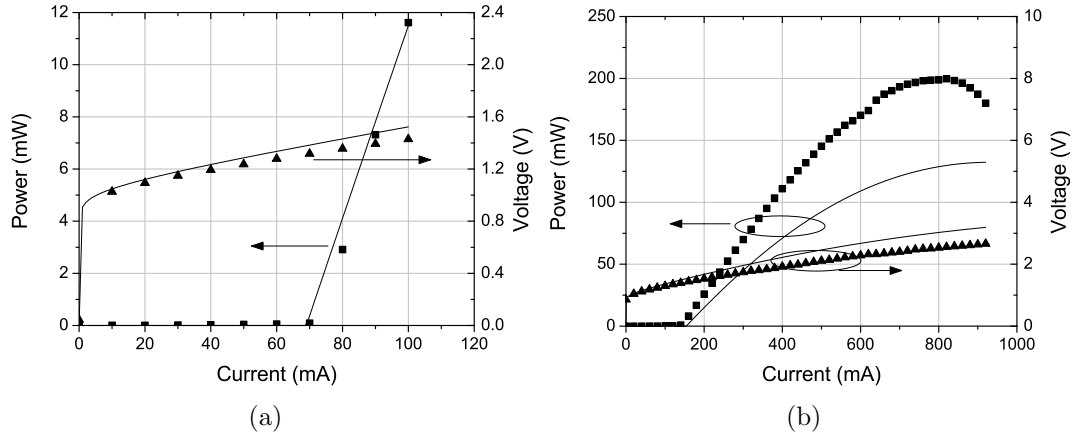


Figure 5.10: L-I-V simulations. (a) Simulation (solid lines) and experimental data (squares) for a typical $10 \times 1222 \mu\text{m}$ device at 15°C and (b) for an outstanding $20 \times 1222 \mu\text{m}$ device at 20°C .

size, the measured threshold density and external quantum efficiency are relatively constant across a laser bar. Thus, these figures of merit can be reliably generated through simulation. However, since the thermal rollover can occur as high as $7-10I_{th}$, P_{max}^{CW} is inherently harder to simulate due to its sensitivity to slight variation in the input parameters. Not surprisingly, therefore, its experimental value has differed by as much as 50% for devices of the same size from the same laser bar tested under identical conditions. This explains why these simulations are sometimes inaccurate at high biases.

To investigate the sensitivity of these figures of merit, a statistical analysis was performed in which the simulation was repeated for various input model parameters. The input parameters were given independent Gaussian distributions; the means and standard deviations are set to be the experimentally determined values for the parameters and their uncertainties, respectively. Figs. 5.11a through 5.11d are the resulting box plot simulations for the cavity length dependence of the CW threshold current, threshold density, external efficiency, and maximum CW output power, of a

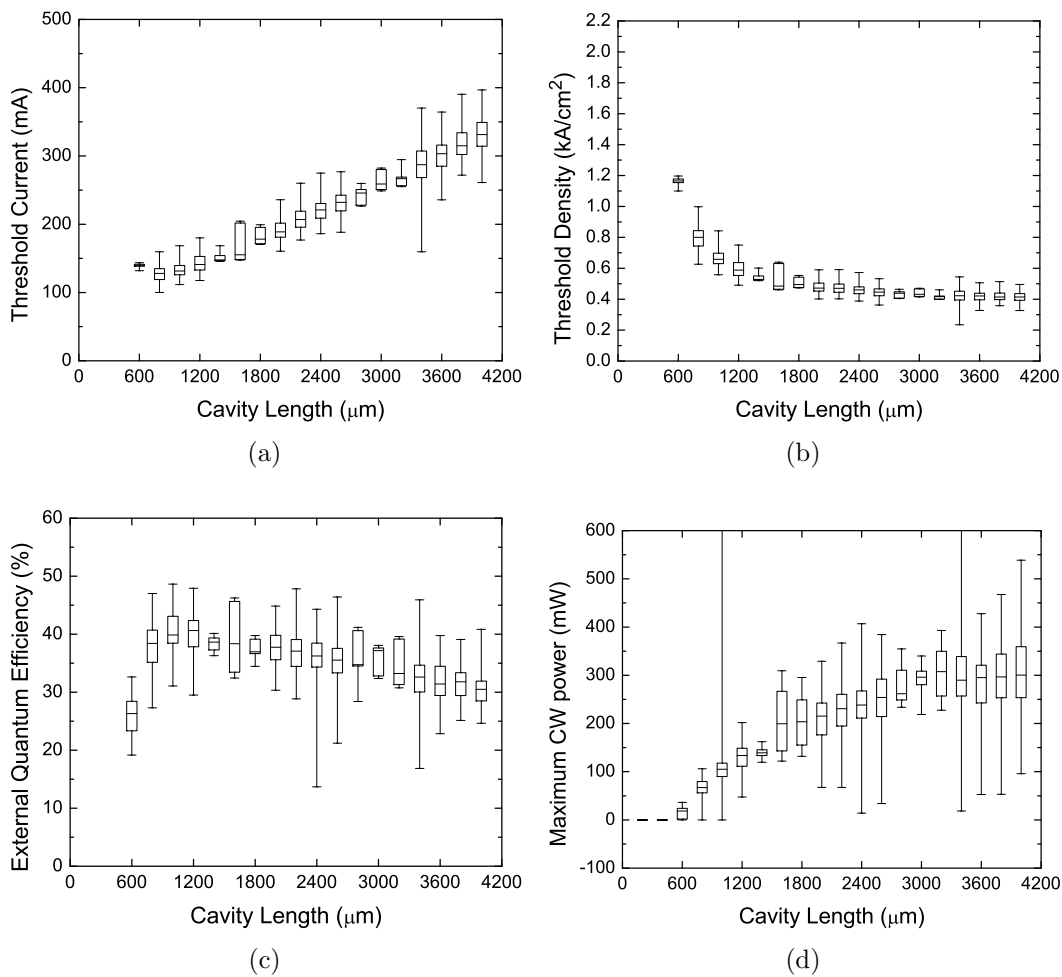


Figure 5.11: Epi-up standard mounting; box plot simulations of a $20\mu\text{m}$ wide SQW laser versus cavity length under CW operation. (a) threshold current, (b) threshold density, (c) external efficiency, and (d) maximum output power. Each data symbol has: (1) vertical line caps for the range, (2) box boundaries for the 25 and 75 percentiles, and (3) a line in the middle of the box for the median.

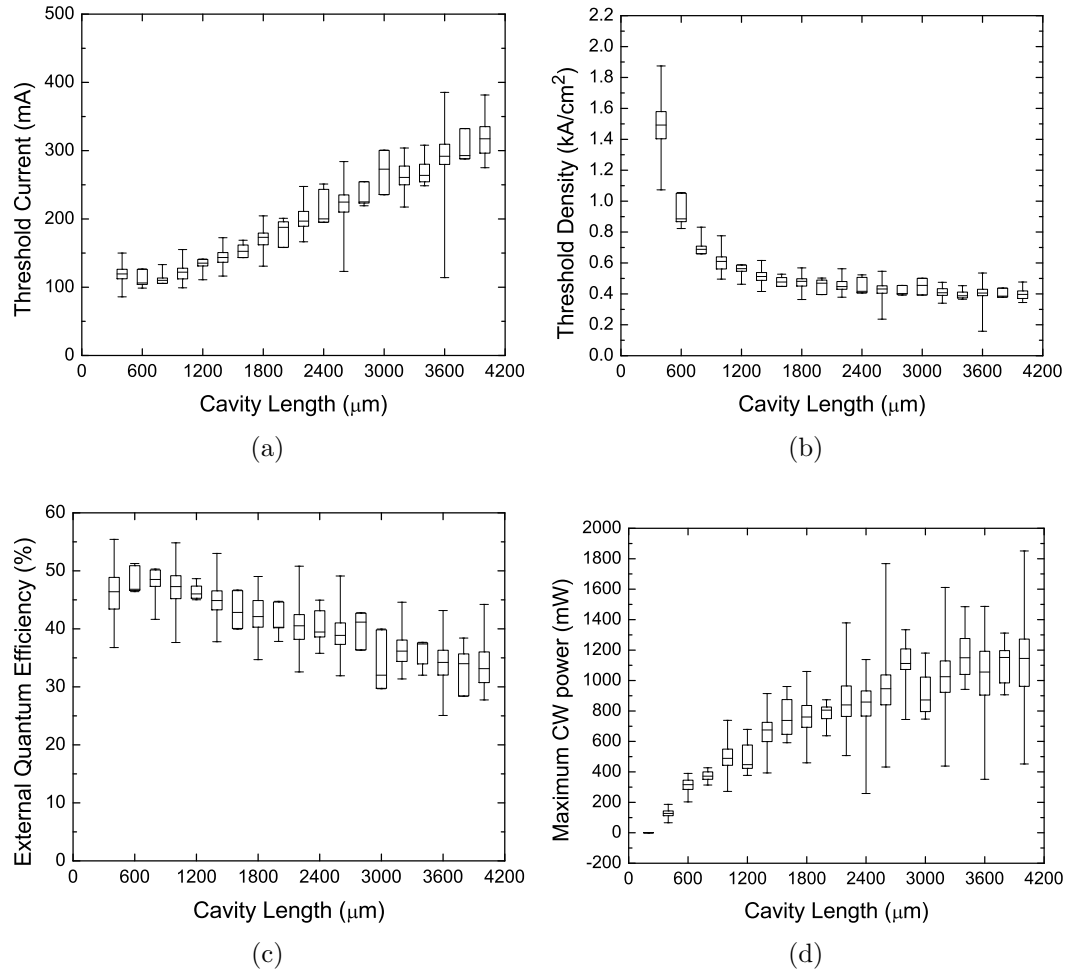


Figure 5.12: Epi-down mounting to diamond; box plot simulations of a 20 μm wide SQW laser versus cavity length for comparison with epi-up mounting in Fig. 5.11.

20 μm wide laser at $T_s=15^\circ\text{C}$ with three probe contacts. For each length, 100 lasers were simulated and the cavity lengths simulated range from 200 to 4000 μm in 200 μm increments. Each data point of the box-plot shows: (1) the range of the data denoted by the caps at the end of the vertical line, (2) the 25 and 75 percentiles denoted by the lower and upper boundaries of the box, and (3) the median denoted by the line in the middle of the box.

The dependencies of Figs. 5.11a and 5.11b are well understood: J_{th} decreases monotonically with length since the mirror loss is being reduced; whereas I_{th} has a minimum at some cavity length since the active area increases with length. The minimum I_{th} occurs near 800 μm cavity length. The device is unable to lase in CW mode for the 200 and 400 μm lengths. The external quantum efficiency, which is known to decrease with length, shows an interesting rise for small cavity lengths. Since the internal efficiency is very temperature sensitive, the external efficiency is low for short cavities due to device heating. From the Fig. 5.11d, we see that the optimum device length to maximize the CW output power is around 3000-4000 μm . In this length range, the mirror loss is becoming comparable to the internal loss and the reduction in the thermal resistance with length is becoming outweighed by the decrease in efficiency. As mentioned previously, P_{max}^{CW} is more sensitive to input parameters and so extrapolation to device lengths this far outside the range of our previously conducted experiments (500-2150 μm) may lead to inaccuracies in the prediction of P_{max}^{CW} . Also, the simulation failed to converge to reasonable values at a two device lengths as shown by the vertical lines that extend beyond the top of Fig. 5.11d.

The simulations are repeated in Figs. 5.12a through 5.12d for the case of epi-down mounting to a diamond CVD heatsink with 1 μm of ^{100}In solder. Under these conditions, the general trends are similar with slightly better threshold currents and external efficiencies. The major difference is in P_{max}^{CW} , where the optimum cavity length appears to be larger than 4000 μm and output powers exceeding 1W seem typical. This

optimum operation point and predicted performance is strongly affected by the exact thermal and series resistance that can be achieved through epi-down mounting. It is likely that the series resistance will actually be much lower and the performance better than the simulated case, which used the I-V characteristics for epi-up mounting.

Figs. 5.13a and 5.13b show the output facet reflectivity dependence of the threshold density and maximum CW output power, of a $20 \times 1000 \mu\text{m}$ laser with an HR coated facet ($R=100\%$); Figs. 5.13c and 5.13d are the corresponding simulations for epi-down mounting to a diamond CVD heatsink. The maximum CW output power simulations failed to converge at a few points for some reflectivities under epi-up mounting and so the data here may be slightly biased. In any case, the threshold density decreases as the output facet reflectivity increases as expected. For this $20 \times 1000 \mu\text{m}$ size device, the optimum reflectivity for P_{max}^{CW} appears to be between 20-40% for the epi-up mounting and slightly less for epi-down mounting. Due to the flat response of P_{max}^{CW} with respect to reflectivity, the single facet power of an HR coated device is predicted to be quite similar to the total output power from two cleaved facets. The rest of the simulations in this section will be for as cleaved facets.

Figs. 5.14a and 5.14b show the ridge width dependence of the threshold density and maximum CW output power, of a $1000 \mu\text{m}$ long laser with standard epi-up mounting; Figs. 5.14c and 5.14d are the corresponding simulations for epi-down mounting to a diamond CVD heatsink. The simulations failed to converge at a few points of the $5 \mu\text{m}$ stripe width and a few of the $10 \mu\text{m}$ widths. Comparing Figs. 5.14a and 5.14c, we observe that the threshold density is roughly constant for short ridge widths (5- $20 \mu\text{m}$), but there is a slight increase with ridge width for standard mounting that is not present for epi-down mounting and so we conclude this is caused by heating. From Figs. 5.14b and 5.14d, we conclude that for this cavity length of $1000 \mu\text{m}$, the narrow ridge widths (5- $20 \mu\text{m}$) are better than the large ridge widths (50- $100 \mu\text{m}$) in

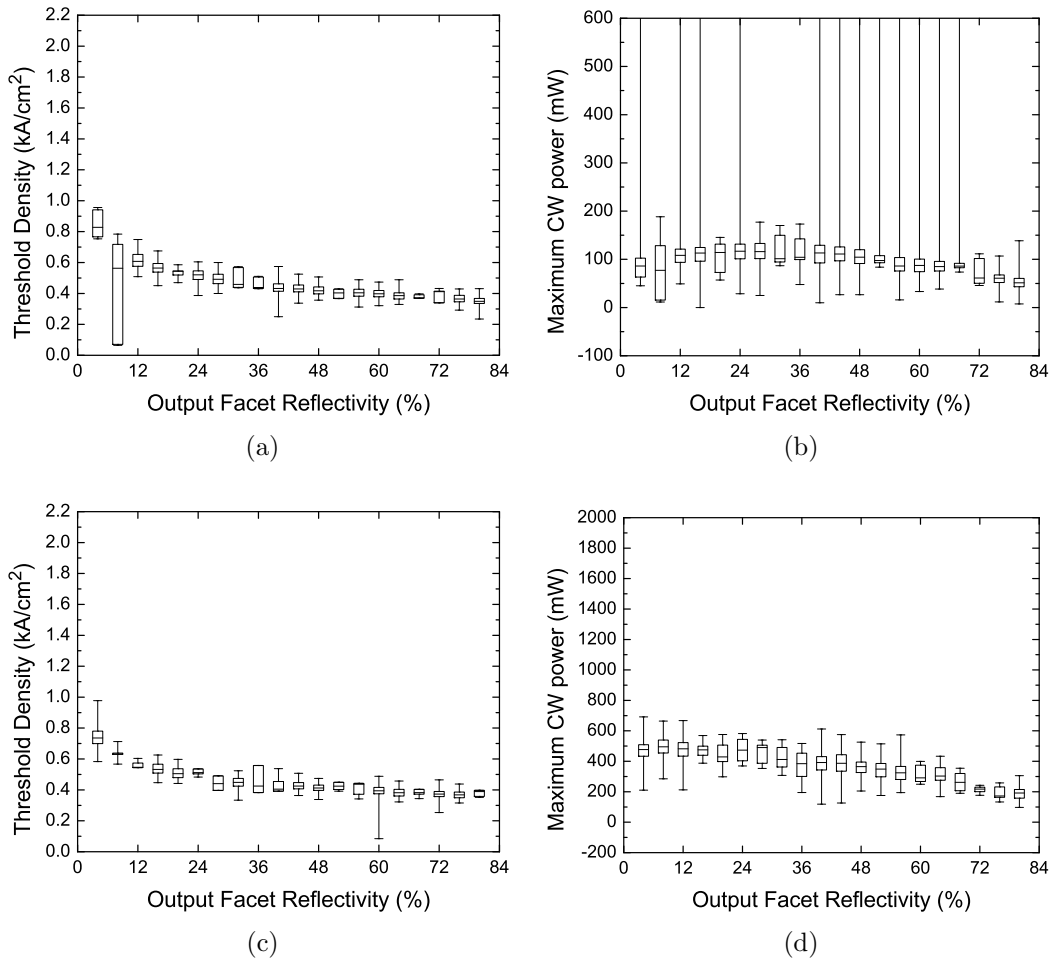


Figure 5.13: Epi-up standard mounting (a) and (b) and Epi-down mounting to diamond (c) and (d); box plot simulations of a $20 \times 1000 \mu\text{m}$ HR coated SQW laser versus output facet reflectivity.

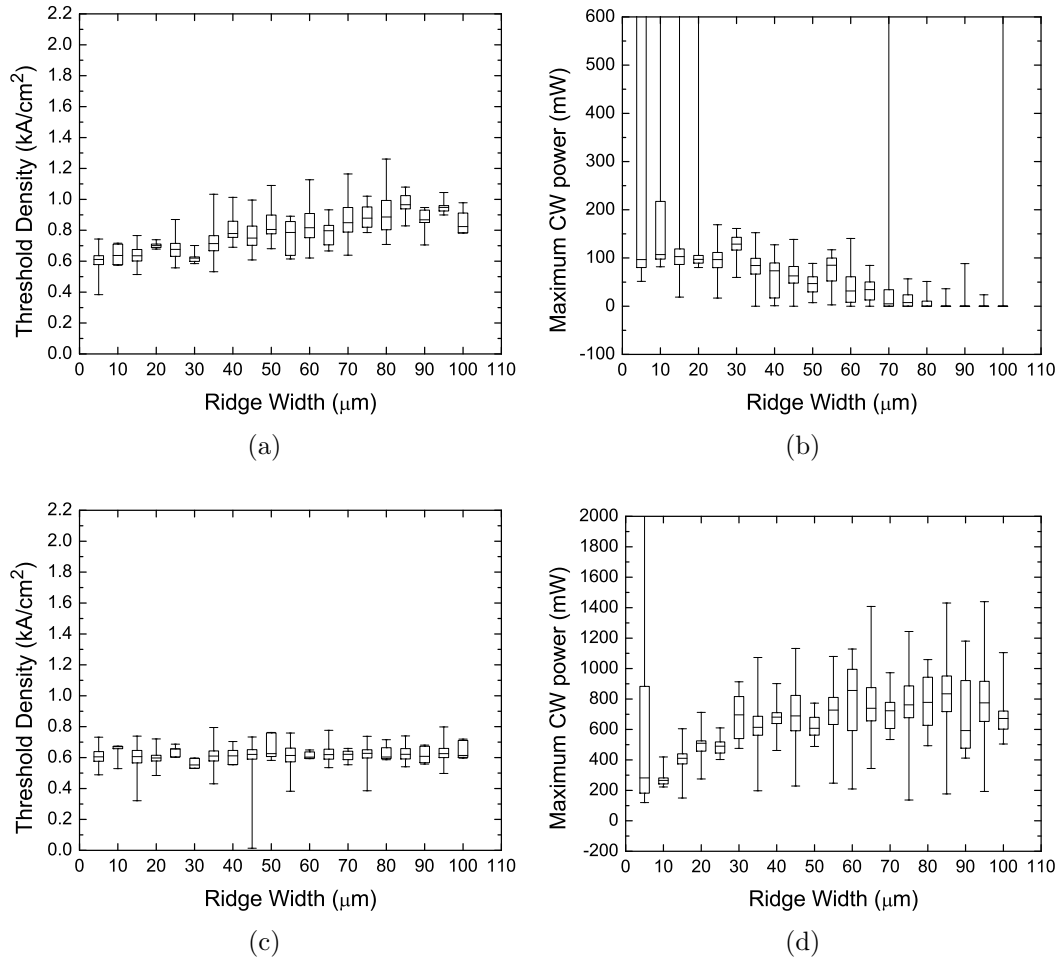


Figure 5.14: Epi-up standard mounting (a) and (b) and Epi-down mounting to diamond (c) and (d); box plot simulations of a $1000\mu\text{m}$ long SQW laser versus ridge width.

standard mounting whereas the trend is reversed for epi-down mounting. Simulations of $100\mu\text{m}$ wide by $4000\mu\text{m}$ laser mounted epi-down indicate a median value for P_{max}^{CW} of 4.5W.

To many in the field, it is surprising that powers exceeding 425mW have been demonstrated from a SQW device. It has been suggested that switching to a multiple quantum well (MQW) structure, as is common in InGaAsP lasers, could greatly increase P_{max}^{CW} . For a MQW laser, the only change to the model is that modal gain scales with the number of quantum wells n_{QW} according to:

$$\Gamma g = n_{QW} \Gamma_0 g_0 L n \left(\frac{\eta_i J / n_{QW}}{J_{tr}} \right) \quad (5.17)$$

under the assumption that the optical confinement factor scales linearly with the number of wells and that the material gain is the same for a fixed current density per well. Since modal gain equals total loss at threshold, J_{th} for a MQW laser is given by:

$$J_{th} = n_{QW} J_{tr} \text{Exp} \left(\frac{\alpha_i + \alpha_m}{n_{QW} \Gamma_0 g_0} \right) \quad (5.18)$$

Straightforward minimization of J_{th} shows that the optimal number of wells:

$$n_{QW}^{th} = \frac{\alpha_i + \alpha_m}{\Gamma_0 g_0} \quad (5.19)$$

This value will depend on temperature and device length due to the strong temperature sensitivity of g_0 and cavity length dependence of α_m . Equation 5.19 can be used to estimate the optimal number of wells, but will not be exactly correct since the number of wells is integer valued. No simple formula can be derived for the optimal number of wells to maximize CW output power.

Figs. 5.15a and 5.15b show the cavity length dependence of the threshold density and maximum CW output power, of a double quantum well (DQW) $20\mu\text{m}$ wide laser

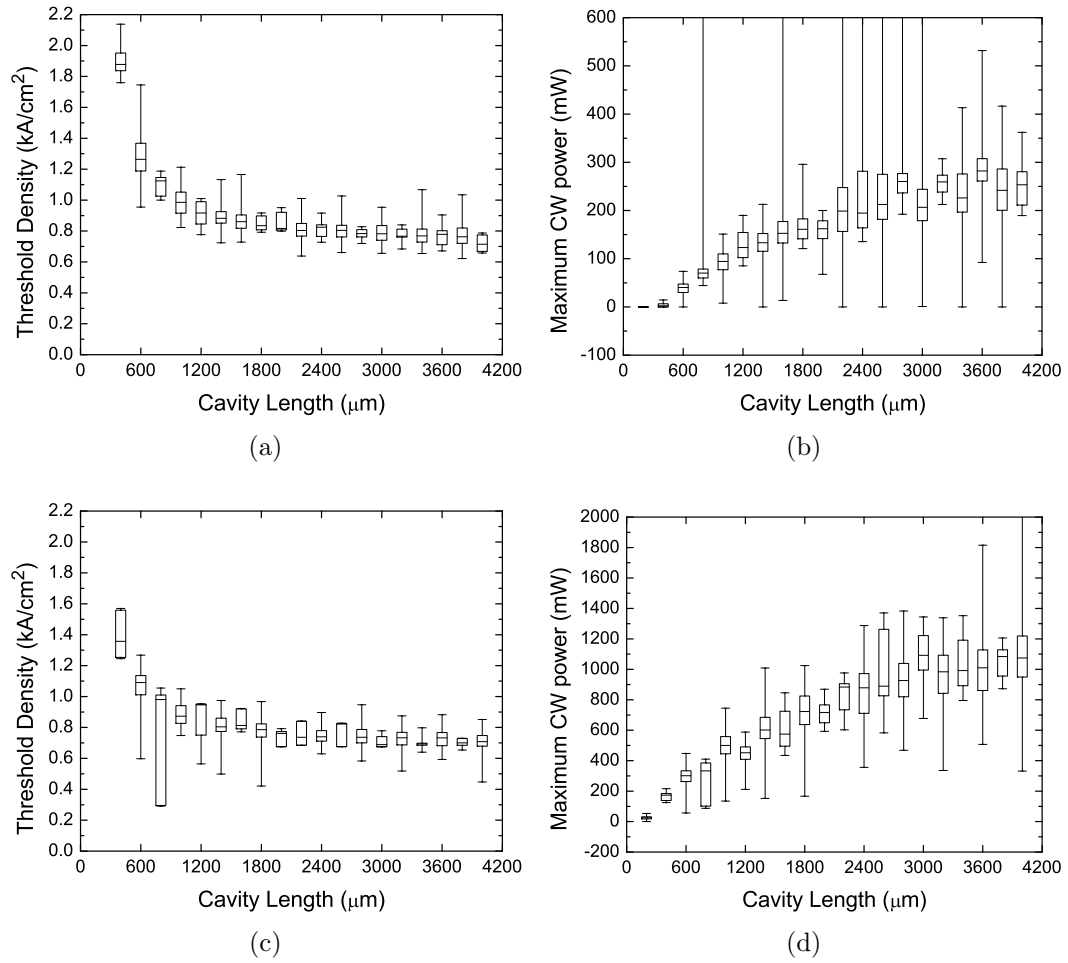


Figure 5.15: Epi-up standard mounting (a) and (b) and Epi-down mounting to diamond (c) and (d); box plot simulations of a $20\mu\text{m}$ wide **DQW** laser versus cavity length for comparison with **SQW** laser mounted epi-up in Figs. 5.11(b) and 5.11(d) and epi-down in Figs. 5.12(b) and 5.12(d).

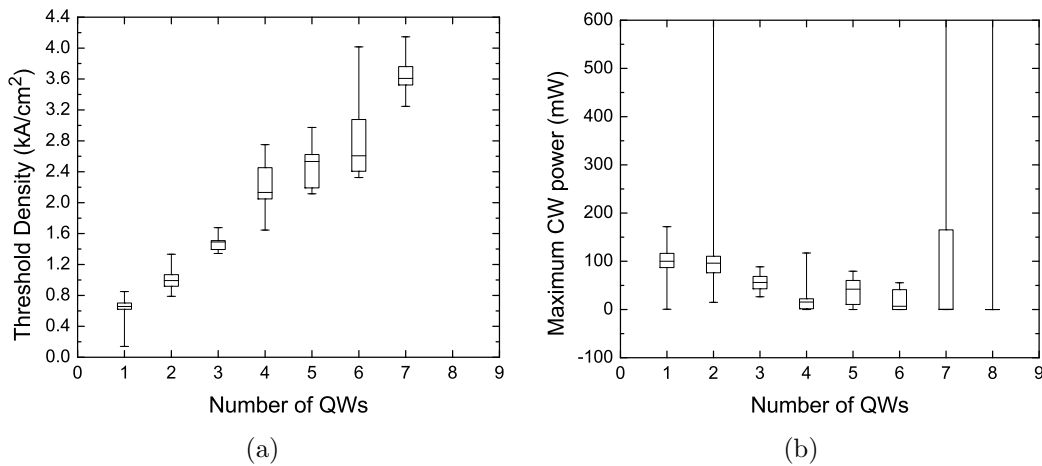


Figure 5.16: Epi-up standard mounting; box plot simulations of a $20 \times 1000 \mu\text{m}$ wide laser versus number of quantum wells.

at $T_s = 15^\circ \text{C}$ with three probe contacts and standard epi-up mounting. Compared to Figs. 5.11b and 5.11d, we observe better performance from the DQW only for short cavity lengths. Figs. 5.15c and 5.15d are the corresponding simulations for epi-down mounting to a diamond CVD heatsink. Again, very little change can be seen for the DQW compared to SQW other than a higher threshold density and slightly lower output power for long cavity lengths.

Figs. 5.16a and 5.16b show dependence on the number of quantum wells of the threshold density and maximum CW output power, of a $20 \times 1000 \mu\text{m}$ laser at $T_s = 15^\circ \text{C}$ with three probe contacts and standard epi-up mounting. The performance gets worse as the number of wells is increased. The ideal number of quantum wells for this sized device at this temperature is one. Other simulations (not shown) indicate that increasing the number of quantum wells only helps when the stage temperature is elevated or the device length is very short. This is expected according to Equation 5.19 and the strong temperature sensitivity of g_0 .

5.5 Microscopic Modeling – The Rate Equation Model

Carrier and photon dynamics have been investigated through modified rate equations with Langevin noise sources. The active region is divided into segments of length $dx=v_g dt$ and a homemade 4th order Runge-Kutta PDE solver, written in C, is used to approximate the solution to:

$$\frac{\partial n}{\partial t} = \frac{J}{qd} + D \frac{\partial^2 n}{\partial^2 x} - \frac{n}{\tau} - v_g(\Gamma + \Gamma_u)g(n)(N_L + N_R) + F_n(t) \quad (5.20)$$

$$\frac{\partial N_{L,R}}{\partial t} = v_g(\Gamma g(n) - \alpha_i)N_{L,R} + \frac{1}{2} \frac{\theta}{\tau_r} + F_{N_{L,R}}(t) \quad (5.21)$$

with mode propagation and boundary conditions:

$$\begin{aligned} N_R(x, t + dt) &= N_R(x - v_g dt, t) & N_R(0, t + dt) &= R_L N_L(0, t) \\ N_L(x, t + dt) &= N_L(x + v_g dt, t) & N_L(L, t + dt) &= R_R N_R(L, t) \end{aligned} \quad (5.22)$$

where n is the electron carrier density, J is the injected current density, d is the QW thickness, D is the diffusion constant, x is the position along the cavity length, τ is the carrier lifetime, v_g is the group velocity, N_L and N_R are the left and right moving photon densities, F_n and F_N are the carrier and photon Langevin noise sources, θ is the spontaneous emission factor, and τ_r is the radiative lifetime. It is important to note that the majority of these parameters depend on position in x , y , and z -directions. Only the QW region will be simulated and the model assumes that there is only one propagation mode. By including more terms N_L^i and N_R^i , multiple modes can be simulated. Outside the QW region, we assume transparent material, negligible carrier densities and ignore recombination.

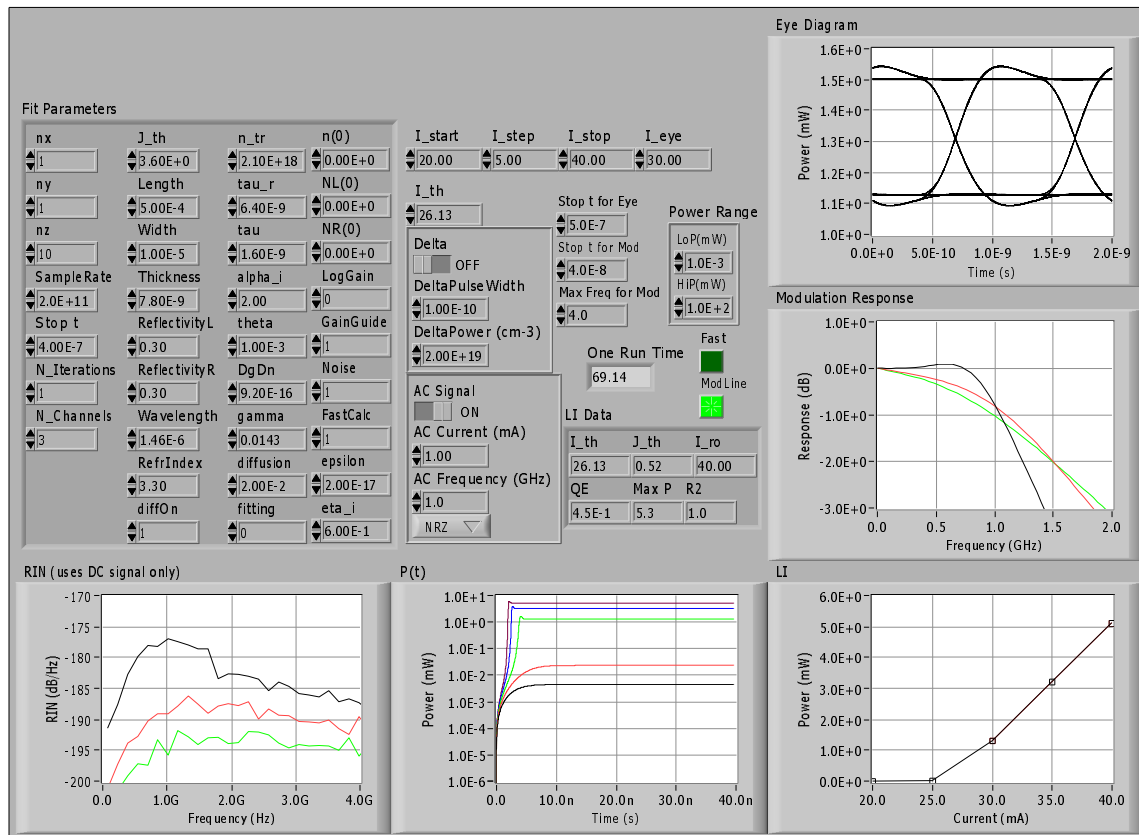


Figure 5.17: (Color) Simulations of eye diagram, small signal response, relative intensity noise, and L-I characteristics using the rate equation model for a $10 \times 500 \mu\text{m}$ laser.

A linear gain versus carrier density model with nonlinear gain compression was used to simulate the performance of a $10 \times 500 \mu\text{m}$ laser in Fig. 5.17. The top left corner of the figure shows the input parameters of the simulation. The lower left corner shows the RIN spectrum. The simulated RIN lineshape and behavior with DC optical power is similar to those of devices in Section 4.4, but the overall RIN level is $\approx 40\text{dB}$ lower than the measured data for two reasons. First, the noise generated due to the probabilistic nature of reflection from the mirrors was not included. Second, only one mode was simulated. Real devices have noise associated with power transfer between modes, spontaneous emission from non-lasing modes, and output coupling. The graph in the middle is the time evolution of the output power and the graph on the right is the L-I curve. A threshold density of $520\text{A}/\text{cm}^2$ and external efficiency of 45% are predicted. These values agree with the general trends in the macroscopic modeling of Section 5.4. Above the L-I curve is the modulation response as a function of frequency for applied currents of 30, 35, and 40mA. As the bias is increased, the modulation response becomes flatter and the maximum 3dB modulation frequency is increased. Faster devices can be obtained by decreasing the cavity length. The eye diagram for a 1GHz non-return to zero (NRZ) signal is shown in the upper right graph for a 30mA bias. Under these conditions, the eye opening is large and there is minimal intersymbol interference (ISI). There is negligible timing jitter since this was not explicitly simulated.

Fig. 5.18 shows the time evolution of the output power in the lower left figure and the drive current and light intensity response together on an arbitrary scale in the middle figure for a 5mA peak-to-peak laser drive current modulation with a 40mA DC bias. The column of graphs on the right displays the time evolution of the positional dependence of carrier and left and right moving photon densities. The intensity of the left moving photons is low at the top of the graph (right edge of laser) and builds up to a maximum at the bottom of the graph (left edge of laser). The reverse happens

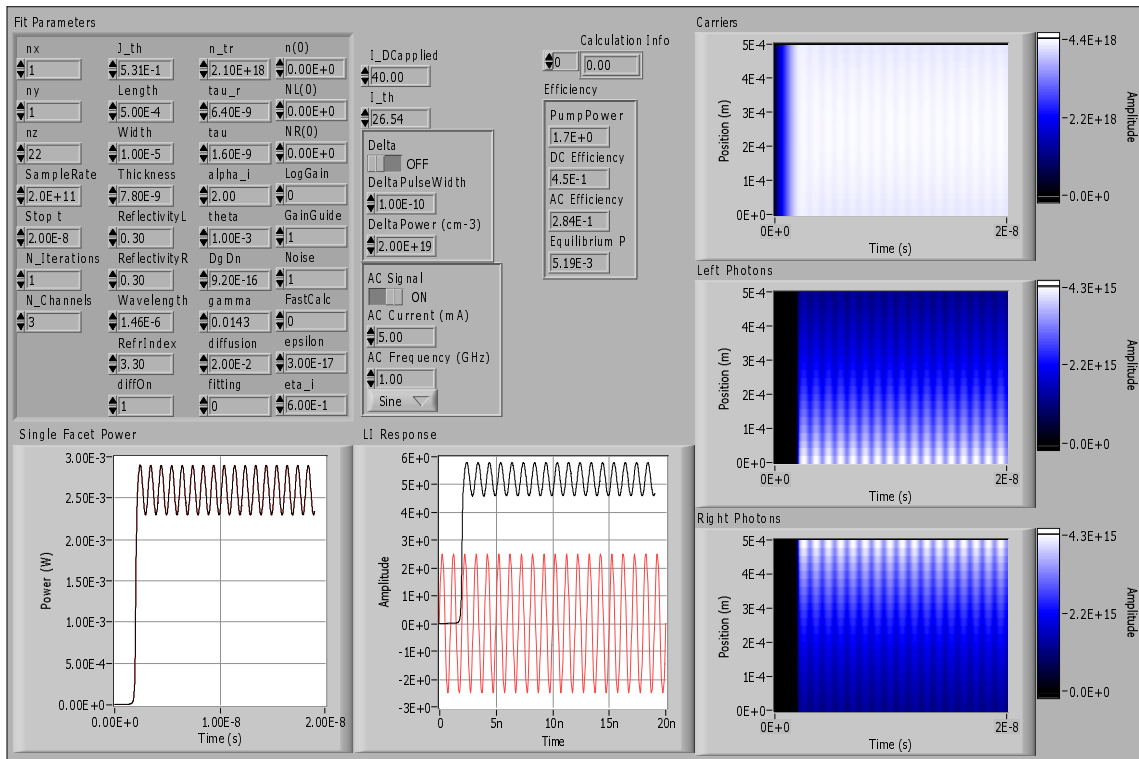


Figure 5.18: (Color) Simulations of carrier and photon dynamics for a $10 \times 500 \mu\text{m}$ laser under a 5mA modulation.

for right moving photons. The carrier density is roughly constant with position, but is slightly higher at the center, where the total photon density is lowest.

Initially, the carrier density is low, but after a few short transients, it soon oscillates around the steady state equilibrium due to the AC modulation current. These oscillations are visible as the faint vertical stripes. The optical field takes longer to build up because the carrier density must first reach threshold. The rise time for both the carrier and photon densities is determined by the total carrier lifetime, τ , (**NOT** the radiative lifetime, τ_r) because the time for the optical field to build up is determined by how quickly the carriers achieve inversion, which is dictated by the total carrier lifetime. At higher biases, the carriers achieve inversion sooner and the lag between the build up of the two densities disappears.

Chapter 6

Conclusion

Band structure modeling using multiband $\mathbf{k} \cdot \mathbf{p}$, the Band Anti-Crossing model, and Pikus-Bir strain Hamiltonian was performed to calculate a map of the bandgap, offsets, and effective masses for various GaInNAsSb material compositions. Two predicted features of the GaInNAsSb/GaAs material system are a large conduction band offset ratio and effective mass. The deeper confinement of electrons for GaInNAsSb/GaAs compared to InGaAsP/InP resulted in better temperature sensitivity, T_0 , and enhanced differential gain, dg/dn , which will facilitate uncooled and high-speed/high-power operation, respectively.

The spontaneous emission measurements performed below and above threshold indicate the presence of large amounts of non-radiative recombination and the failure of the radiative recombination rate to strongly clamp at threshold. At room temperature, non-radiative recombination represents 90% of the threshold current for 1st generation devices and about 80% for 2nd generation lasers. At elevated temperatures, carrier leakage or Auger recombination become the dominant non-radiative sources because of their strong dependence on temperature and carrier concentration. The weak clamping of the quasi-Fermi levels above threshold, possibly caused by the large nonlinear gain compression coefficient ε , allows additional recombination to occur, reducing the internal efficiency.

The multi-section gain technique was adapted to obtain absorption data and provide accurate measurements of the bandgap, band offsets, and effective masses of GaInNAsSb. Although the relatively even split in the electron/heavy hole band offsets is favorable, the effective barrier heights might be too small to prevent thermionic escape of both types of carriers at high temperatures.

Reducing ion damage during growth and optimizing material quality during a medium temperature RTA have resulted in significantly improved device performance over previous world records. Room temperature, CW, threshold densities below 500A/cm² and maximum output powers above 425mW at 1.5 μ m have been achieved from SQW GaInNAsSb lasers mounted epitaxial-side up. Z-parameter measurements and the probe contact study confirm that the improvements over our previous reports are primarily due to a reduction in the monomolecular recombination current and in the contact and series resistances. Two interstitial traps, (N-N)_{As} and (As-N)_{As}, believed to be located in the barrier have been identified as the probable sources of monomolecular recombination. Although strain compensation would be lost, switching from GaNAs barriers to GaAs barriers would reduce the trap recombination as well as provide better carrier confinement.

The Z-parameter measurements also confirmed that an increase in monomolecular recombination is responsible for device degradation during life testing. Reliability testing at 10mW CW from 1st generation lasers for less than 120 hours resulted in a doubling of operation current. The high levels of monomolecular recombination in these devices provide thermal energy that enhances defect propagation and eventually leads to extended defects. This further accelerates device failure by increasing the number of non-radiative recombination sites leading to a rapid initial rise in operation current. The process slowly saturates as the strain is relieved leading to a more gradual rise in current over time. Since 2nd generation lasers have much

lower monomolecular recombination, improved reliability was achieved. Operation at 200mW CW for nearly 500 hours resulted in only a 13% rise in current.

Without the previously dominant temperature-insensitive monomolecular recombination, the temperature stability of device operation was adversely affected. The characteristic temperatures for threshold current, T_0 , and for efficiency, T_1 , for a 2150 μm long 2nd generation device were 77K and 122K, respectively. Compared to 106K and 208K from a 1st generation device with an equivalent mirror loss ($L=983\mu\text{m}$ but HR coated), these values are significantly reduced and they indicate that carrier leakage or Auger recombination is now dominant. The temperature sensitivity of the internal efficiency and gain coefficient was found to strongly influence T_0 and T_1 .

The predicted enhanced differential gain of GaInNAsSb/GaAs lasers at 1.5 μm compared to InP-based lasers was verified experimentally through RIN analysis. The differential gain of approximately $1 \times 10^{-15} \text{cm}^2$ is significantly higher than the $2-8 \times 10^{-16} \text{cm}^2$ for multiple quantum well (MQW) InGaAsP/InP lasers and is a major advantage of the GaInNAsSb material system. High power and low threshold lasers can be achieved from a SQW structure for GaInNAsSb that can only be matched by MQW structures for InGaAsP. The enhanced differential gain also implies a lower carrier concentration at threshold and so we should expect to see lower non-radiative Auger recombination, which scales as n^3 in the non-degenerate limit.

The differential gain is very temperature sensitive and has a characteristic temperature of only 57K. Since the total loss increases very slightly with temperature and the transparency carrier density is predicted to have a large characteristic temperature of 244K, the low value of $T_0=64\text{K}$ for that device is attributed to behavior of the differential gain. This is consistent with the previous conclusion that the internal efficiency and gain coefficient are responsible for low values of T_0 since differential gain is directly related to these other two parameters. A large nonlinear gain compression of $\varepsilon=1.4 \times 10^{-16} \text{cm}^3$ was measured at room temperature. Nonlinear gain compression

leads to saturation of the peak laser emission intensity and spectral broadening at high power.

Laser performance has been simulated for various device geometries and mounting configurations using the characterized intrinsic electrical and optical parameters and their temperature dependence. Despite the decrease in external efficiency with cavity length, the simulations show that the optimum device length to maximize the CW output power is over $3000\mu\text{m}$ for a $20\mu\text{m}$ wide device for both epi-up and epi-down mounting. Output powers exceeding 1W seem easily attainable for lasers with a $20\mu\text{m}$ stripe width mounted epi-down to a diamond CVD heatsink. Higher CW output powers, comparable to the reported 8W from a $100\times 2000\mu\text{m}$ GaInNAs/GaAs at $1.3\mu\text{m}$ [44, 45] should also be possible in future GaInNAsSb/GaAs lasers at $1.5\mu\text{m}$ with larger areas (4.5W in the $100\times 4000\mu\text{m}$ simulation) enabling their use for Raman and doped-fiber amplifiers.

Although a multiple quantum well (MQW) laser has stronger optical confinement resulting in a lower the threshold carrier density and reduce leakage and Auger recombination, simulations of device performance indicate that the single quantum well (SQW) structure is ideal for room temperature operation. At elevated temperatures, the number of wells should be increased to compensate for the temperature sensitivity of the gain coefficient.

GaInNAsSb VCSELs, high power edge-emitting lasers, and narrow linewidth DFB lasers grown monolithically on GaAs will soon become widely commercialized throughout the low-loss telecommunication wavelength window due to their numerous advantages over InP-based devices. In addition to the improved intrinsic material parameters discussed in this thesis, GaInNAsSb has a major advantage over InGaAsP/InP because it is lattice matched to AlAs and GaAs. This leads to lower manufacturing costs, simpler DBR growths for VCSELs, and the possibility of using oxide apertures for carrier and optical confinement. GaInNAsSb is a unique material

system that can operate over a wide bandgap range 0.75-1.4eV and can be incorporated with novel GaAs-based optoelectronic devices, such as photonic bandgap crystals or nonlinear optics. It will no doubt revolutionize the telecommunications and photonic integrated circuit industries with its numerous applications.

Chapter 7

Future Research

Since GaInNAsSb is a novel material system, there still exist many intrinsic laser parameters that have not been measured or calculated. Future theoretical research could involve expanding the band structure modeling discussed in Chapter 2 to obtain the energy dispersion relations in the principal crystallographic directions throughout the entire Brillouin zone rather than just near the center of the zone in the effective mass approximation. Simulations of the carrier dynamics throughout the structure and thermal profiles of the laser as a function of injected current density are needed to supplement the existing code for waveguide and band structure modeling. With a self-consistent model for the band structure and thermal, electrical, and optical properties, more efficient optimization of the laser design can be achieved.

A major goal of future experimental research on GaInNAsSb should be to accurately measure the band offsets and effective masses, as well as the carrier density versus current relationship. The multiple section technique presented in Chapter 3 provided a coarse measurement for both. However, improved precision in the band offset/effective mass measurement can be achieved by performing photoreflectance (PR) and multiple section absorption studies on quantum wells of varying thickness using GaAs barriers, which have well-known parameters. For the carrier density measurement, integrating the measured differential carrier lifetime [95] produces more

accurate results than measurements of quasi-Fermi level separations, band structure and bandgap renormalization. The differential carrier lifetime can be measured using the impedance independent small-signal modulation technique described in [113] or the improved, but more difficult, pulsed optical pumping technique described in [114]. With a more accurate carrier density versus current measurement, further analysis of recombination can be performed and the conclusions of the Z-parameter technique can be corroborated.

Another research area that uses the same experimental set-up is measurement of the small-signal modulation characteristics of the laser above threshold. Laser parameters, such as: the linewidth enhancement factor ($\alpha = -2k_0 \frac{dn_r/dn}{dg/dn}$, where k_0 is the wavevector in free space and n_r is the refractive index), 3-dB modulation bandwidth, wavelength chirp, harmonic and intermodulation distortion, and spurious free dynamic range (SFDR) could be directly characterized rather than estimated theoretically. Also, the lasers could be integrated into test optical networks for measuring performance graphs, such as: eye-diagrams, bathtub curves, and bit error rate versus signal power.

Reliability and failure analysis is another practical research area. Due to our limited testing capabilities, the sample size of the reliability data is too small to perform any meaningful statistical analyses. Multiple racks of arrays of individual lasers tested in **parallel** under various temperatures, humidities, operation powers, and on-off modulation stresses will be invaluable in determining the viability of GaInNAsSb in commercial systems. Also, reliability testing of lasers grown under different conditions, with different material compositions and post-growth processing may help to further identify the sources of device degradation. In addition to Z-parameter analysis, deep level trap spectroscopy (DLTS) performed before and after life testing would be invaluable in determining how the trap density changes with operation. It seems that growth improvements, such as the deflection plates and arsenic cap, and

processing improvements, such as optimizing the rapid thermal anneal have reduced the overall defect density. However, additional studies on lasers with GaAs barriers or GaNAs barriers with a thin GaAs buffer layer between the barrier and QW are needed isolate the source of traps. The study will help to determine whether the traps are located primarily in the barriers or distributed throughout the barriers and QW and hopefully will tell us which growth factors most strongly affect trap formation.

Appendix A

Laser Test Station

The edge-emitting laser test station consists of a $\frac{5}{8}$ " thick, $2\frac{3}{4}$ " square copper heatsink and a $\frac{5}{16}$ " thick, $1\frac{3}{4}$ " wide by $1\frac{1}{8}$ " deep copper top stage for mounting samples. There is a thermo-electric cooler (TEC) module in between to control the temperature of the top stage. Sample mounting to the top stage is described more fully in Appendix B. For some measurements, a second TEC module (Magaland TEC1-7103, 30x30x4.7mm, Max Ratings: 8.1V, 3.3A, Heat Extraction: 16.4W), or a liquid chipset cooler (Koolance CHC-A05, 25x25x4mm, $\frac{1}{4}$ " ID tubes, Heat Extraction: 30W) is inserted to achieve a larger thermal gradient. To prevent condensation during measurements below 10°C , N_2 gas is flowed into a plastic bag enclosing the set-up.

In CW mode, the laser's voltage and current are monitored with the circuit shown in Fig. A.1. The ILX Lightwave 3744B (or 3722B) current source has a 10V compliance limit and can supply up to 4A (or 500mA) with a set-point resolution of $100\mu\text{A}$ (or $10\mu\text{A}$). Most of the current passes through the probe cabling (not shown) to the floating laser diode before flowing through the current sensing resistor network. The voltage across the network is measured on channel 1 of the oscilloscope. The current flowing through the laser is equal to this voltage divided by the effective network resistance. The effective resistance should be small so that the laser operation is

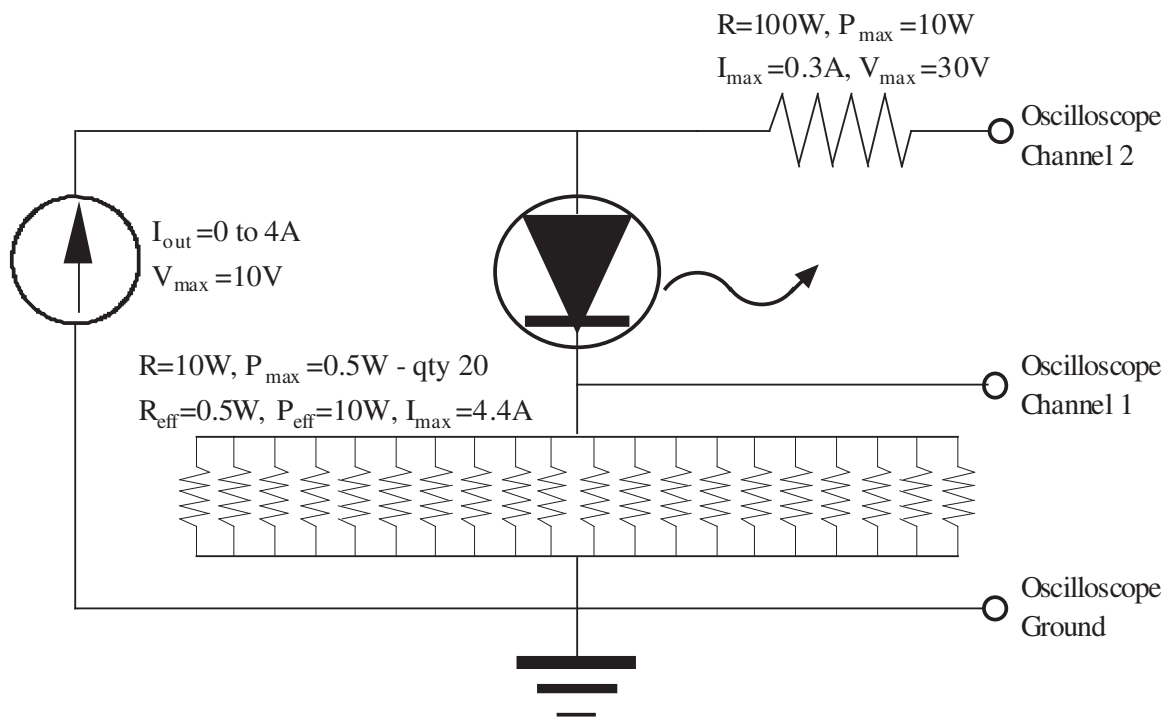


Figure A.1: Voltage and current monitoring circuit.

unaffected and so that the network is capable of handling the maximum supply current of 4A, but sufficiently large to produce a measurable voltage at low currents. Twenty 10Ω resistors, each with 0.5W ratings, are connected in parallel and serve as a 0.5Ω current sensing resistor network. The voltage across the laser and the network is measured on channel 2. The computer subtracts channel 1 from channel 2 to obtain the voltage across the laser. Both oscilloscope channels use the $1M\Omega$ input impedance setting. The 100Ω , 10W resistor protects the oscilloscope from receiving large currents if the laser diode is open and the oscilloscope is on the 50Ω impedance setting.

The pulsed mode monitoring circuit, provided by ILX Lightwave, is quite similar except that it was built with surface mount components ($\frac{1}{16}$ W ratings) and specifically for use with their LDP-3840 pulse generator (3A, 25V compliance). A 50Ω resistor replaces the 100Ω output resistor and the current sensing network consists of ten 5Ω resistors. Power dissipation is less worrisome in pulsed mode since the maximum duty cycle is 10%. A network of five 10Ω tuning resistors is inserted between the current source and the circuit node to the laser for impedance matching. These resistors are removed one by one until a suitable compromise between the pulse rise time and overshoot is attained. However, the pulse generator did not meet pulse rise time specifications (sold at a discount) and so no improvement in the tradeoff was observed when tuning resistors were removed. In addition, the long cable length ($\approx 0.5\text{m}$) to the laser probes precludes operation above 20MHz. Thus, a $1\mu\text{s}$ width (1% duty cycle) was used for almost all of the pulsed measurements. Occasionally, a 400ns minimum pulse width was used for ultra high power measurements. The circuit also had two reverse biased diodes in parallel with the laser and sensing resistor network to protect the laser if the laser polarity is accidentally reversed. However, we removed these diodes to be able to measure some semiconductor devices in reverse bias. In pulsed mode, channels 1 and 2 of the oscilloscope should be on the 50Ω impedance setting

for maximum frequency response and because the LDP-3840 is calibrated assuming a 100Ω parallel path to ground. The voltage across the laser is now calculated as twice the channel 2 reading minus the channel 1 value.

For both pulsed and CW measurements, the laser's optical power is collected with an integrating sphere (LabSphere IS-010, 1" diameter, Spectrafect coating, $1.7\text{J}/\text{cm}^2$ damage threshold). Channel 3 of the oscilloscope measures the laser power from the Thorlabs PDA400 detector, which is mounted on the detector port of the integrating sphere. The PDA400 is a 1mm diameter, 700-1800nm, InGaAs P-I-N detector (100mW CW damage threshold), with an internal transimpedance amplifier (TIA) that provides a switchable gain from 1.5×10^4 to $1.5 \times 10^6 \text{V}/\text{A}$ in 5 steps and a 10V maximum output. The frequency bandwidth is DC-10MHz on the minimum gain setting. A baffle inside the sphere prevents the incident light from directly striking the detector. Instead, incident light experiences diffuse reflection ($R \approx 90\%$) from the sphere's Lambertian surfaces (equal distribution of scattered light per unit solid angle) and a small but fixed fraction of the incident light reaches the detector. Provided that the beam is not clipped, this fraction is independent of the beam size, divergence, and entry angle of the incident light and is approximately given by the fractional area of the detector, 1:2000. Thus, optical powers up to 1.3W of CW can be measured before saturating the TIA. An important design point for the integrating sphere is that the port area should be small compared to the sphere surface area so that a uniform intensity distribution can be attained. Port reducers and port plugs are used to reduce the $\frac{1}{2}$ " detector port to $\frac{1}{8}$ " and to cover unused ports. The set-up was calibrated and the responsivity is $6\text{V}/\text{W}$ at 1500nm on the minimum TIA gain setting. Thus, the measurement range of the integrating sphere and oscilloscope combination is about $1\mu\text{W}$ -1.3W.

The alternative measurement arrangement involves focusing the laser light onto a single mode fiber (SMF28) or multimode fiber (GIF625) for measurement with a fiber

Table A.1: Fiber coupling efficiencies for various lens combinations for $10\mu\text{m}$ ridge waveguides.

Collimation	Focusing	Fiber	Efficiency	Imaging Limitations
C240	F220	GIF625	50%	Clip fast axis
C340	F220	GIF625	85%	Clip fast axis slightly
C240	F260	SMF28	20%	Clip fast axis, big slow axis spot size
C340	F260	SMF28	15%	Clip fast axis, huge slow axis spot size

coupled detector or an optical spectrum analyzer (OSA). Due to the large ellipticity of the laser beam, typically 5:1 to 20:1, less than 20% of the light can be focused onto single mode fiber without the use of circularizing optics. Optimal fiber coupling occurs when the laser's focused Gaussian beam spot size diameter, $2w_0$, exactly equals the mode field diameter of the fiber and beam focuses within the acceptance angle of the fiber. The main tradeoff is in matching the beam size and numerical aperture of the laser to the fiber for both the fast-axis (vertical) and slow-axis (horizontal). Ideally, the collimation and focusing lenses will have the same clear aperture and the beam diameter will fill the clear aperture of the lenses; otherwise, for a given numerical aperture lens, the focused spot size will be increased and the coupling efficiency reduced. The SMF28 fiber has a NA of 0.13 and a mode field diameter of $10.5\mu\text{m}$ ($9.3\mu\text{m}$) at 1550nm (1310nm), while the GIF625 has a NA of 0.27 and a $62.5\mu\text{m}$ core. The simulated beam diameter at the laser facet is $0.94 \times 8.25\mu\text{m}$ for the $10\mu\text{m}$ wide ridge waveguide, which leads to $\text{NA}_{fast}=0.71$ and $\text{NA}_{slow}=0.12$. Aspheric collimation lenses, such as Thorlabs C240TM-C ($f=8\text{mm}$, $\text{NA}=0.5$) or C340TM-C ($f=4.03\text{mm}$, $\text{NA}=0.62$) and fiber coupling packages F220FC-C ($f=11\text{mm}$, $\text{NA}=0.25$) for multimode fiber or F260FC-C ($f=15.29\text{mm}$, $\text{NA}=0.16$) for single mode fiber yield the best coupling efficiencies among the available aspheric lenses on the market. Aspheric lenses generally provide diffraction-limited performance since they do not suffer spherical

aberration from focusing highly divergent beams; however, they usually still experience chromatic aberration. The C240TM-C lens has a larger diameter than the other lenses and so its effective NA for unclipped beams is only 0.31. The approximate coupling efficiency for the various lens combinations is shown in Table A.1.

In all cases, the beam gets clipped along the fast axis since NA_{fast} for the laser exceeds NA of the collimating lens. The coupling efficiency to SMF28 increases as the width of the ridge waveguide decreases, i.e. the laser output beam becomes more circular. Even for the ideal waveguide geometry, the maximum coupling efficiency to SMF28 is less than 75% since the NA of the F260 lens exceeds the NA of the fiber. For some measurements, C280TM-C ($f=18.4\text{mm}$, $NA=0.15$) is used as a collimating lens to minimize the spot size at the fiber input or to reduce back reflections because of its long working distance. However, this leads to massive beam clipping on the fast axis and a maximum of about 20% coupling efficiency to either GIF625 or SMF28.

Attempts were made to improve collection efficiency using acylindrical lenses. An acylindrical lens also provides diffraction-limited performance but focuses light for only one axis. By using a high NA short focal length acylindrical lens for the fast axis, a low NA long focal length acylindrical lens for the slow axis, and a low NA (<0.13) long focal length aspheric focusing lens, collimation efficiencies onto SMF28 exceeding 80% were expected. However, two major unresolved obstacles were: (1) finding the right combination of lenses with the right NAs and focal length ratios and the same clear apertures and (2) individually mounting and aligning the lenses for the two axes. Monolithic acylindrical fast and slow axis lens pairs were also investigated, but the sub $200\mu\text{m}$ working distance of commercially available lens pairs made them impractical to mount for general laser testing.

Appendix B

Laser Sample Preparation

Laser samples were manually cleaved into bars of size 300-2500 μm cavity length by 3-10mm bar length. The mask used consisted of a 5 μm , 10 μm , and 20 μm ridge with a period of 150 μm as shown in Fig. B.1. Thus, many lasers could be tested from a single bar. Lasers were mounted epitaxial side up to a copper heatsink stage. Electrical contact to the bottom n-type metal was made through this stage. Contact to the top p-metal ridge was made at the center of the device with a single 24 μm or 5 μm diameter Tungsten probe. Care was taken in landing the probes to avoid scratching the ridge waveguide while applying sufficient pressure for electrical contact.

Prior to the realization of our first generation of CW devices at 1.5 μm in June 2003, conductive epoxy (Chemtronics CW2400 part B) was used to provide thermal and electrical contact between the lasers and the heatsink. The hardening agent (Chemtronics CW2400 part A) was not included so that samples could be removed after testing. For each sample, a fresh coating of epoxy paste B was applied to the stage with an intentionally broken half of a wide area plastic tweezers.

As configured, the laser heat sinking was sufficient for reliable pulsed measurements but was too poor and unstable for CW testing. Without epoxy paste A, epoxy paste B remained slightly fluid and the probe would slip off the p-metal ridge at

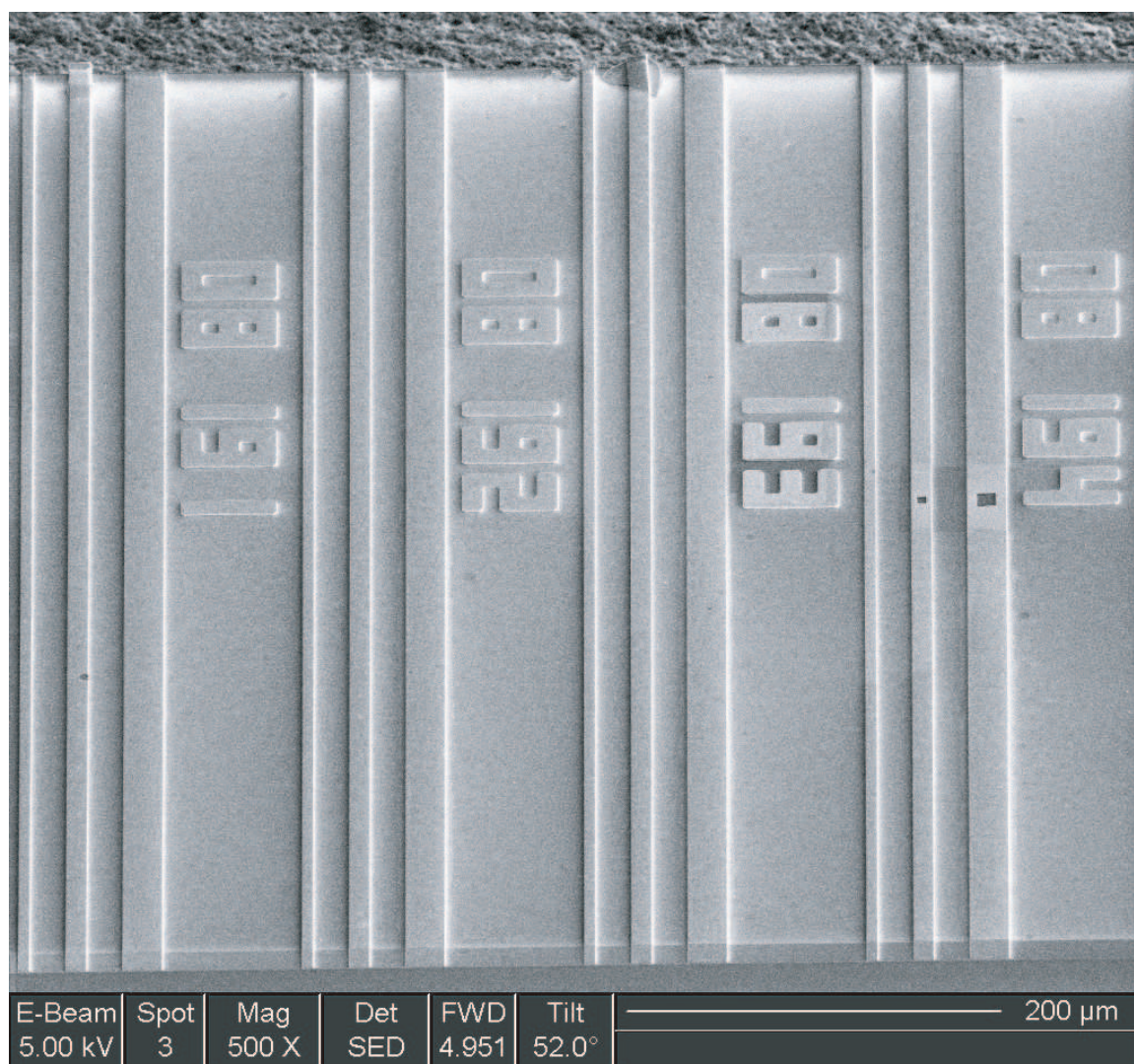


Figure B.1: SEM image (courtesy of Z. Rao) of a $750\mu\text{m}$ long HR coated bar with a $5\mu\text{m}$ square window etched in the top metal of 08-193.2, a $10\mu\text{m}$ wide laser sample, and a $10\mu\text{m}$ square window etched in the $20\mu\text{m}$ wide sample 08-193.3. The HR coating is visible on the upper edge of the scan. The laser bar extends past the bottom of the SEM scan.

Table B.1: Physical properties of various solders and heatsink materials.

Material	Melt Point (°C)	Composition (% mass)	Density (gm/cm ³)	Electrical Resistivity (μΩ-cm)	Thermal Conductivity (W/(cm-K))	Thermal Expansion (PPM/K)	Usage
IndAlloy 1E	118	⁵² In ⁴⁸ Sn	7.30	14.7	0.34	20	Soft solder
IndAlloy 4	157	¹⁰⁰ In	7.31	7.2	0.86	29	Soft solder
IndAlloy 106	183	⁶³ Sn ³⁷ Pb	8.40	15.0	0.50	25	Electronics
IndAlloy 182	280	⁸⁰ Au ²⁰ Sn	14.51	17.4	0.57	16	Hard solder
GaAs	5.32	...	0.55	5.73	Substrate
AlN	3.3	> 10 ²⁰	1.75	4.6	Heatsink
Copper	...	¹⁰⁰ Cu	8.92	1.72	3.98	16.5	Heatsink
Polycrystalline Diamond CVD	3.5	> 10 ²⁰	> 13	2	Heatsink

random times during L-I-V testing. Later, it was observed under the microscope that the paste was actually bubbling because the large Joule heating of the laser.

In July 2002, we switched from epoxy paste B to Indalloy 1E solder from Indium Corporation of America for mounting the gold-coated backside of the sample to the copper heatsink. Indalloy 1E is a ⁵²In⁴⁸Sn eutectic solder that melts at 118 °C and has good wettability on glass, quartz and many ceramics. It has a very low melting point and malleability, which is good for minimizing the effects of differences in the thermal expansion coefficients when dissimilar materials are soldered, i.e. the GaAs wafer and copper heatsink, and minimizing the oxidation of copper at high temperature. Material properties of Indalloy 1E, other potential solders and heatsink material are summarized in Table B.1 [115–125]. The electrical and thermal conductivities of Indalloy 1E are 11.7% and 8.5% of the value for copper. To minimize the path to copper heatsink as well as to prevent the solder from rolling up the side of the laser and coating the mirror facets or shorting out the junction, the minimum available solder thickness, 38μm, was used. This is about 32% as thick as the GaAs wafer and therefore

will contribute to the overall thermal and electrical resistance. However, more surface area is in contact and so the overall performance is significantly improved.

Indium Corp. recommended using 5RMA or 5RA flux with IndAlloy 1E and bonding at 140 °C for several seconds. The thermo-electric cooler (TEC) module on the stage is believed to be Melcor's CP1.0-127-08L. It uses the Peltier effect to achieve a temperature difference from a DC current and has maximum ratings of 2.5A, 15.4V, $\Delta T=67$ °C, and $Q_{max}=21.4$ W. For a 22 °C ambient room temperature, this implies a maximum achievable temperature of 89 °C, however, higher temperatures can be achieved in heating mode because during operation, the TEC generates waste heat that can also be dumped to the hot side. The TEC controller, ILX Lightwave's 3744B can supply 4A and 10V, but typically reaches a maximum temperature around 100 °C as the compliance voltage is reached. In order to reach the eutectic melting temperature, a 200W booster DC power supply, HP 6002A, with compliance limits of 10A or 50V, was used with careful attention paid to the current and voltage limits. When the TEC is at room temperature and the bias is increased from zero to 15V, the TEC current may exceed 2.5A. To prevent this, the current limit of the power supply is set to 2A and the voltage is only increased to 10V. As the TEC heats, the current at fixed voltage decreases; above 75 °C, the current drops to around 1A. The voltage bias is then increased to 15V and the stage temperature can reach 130 °C at about 1A after a few minutes. The bias voltage is then turned down to zero rather than powering off the supply because of potential transient spikes. The stage is allowed to cool on its own in the ambient environment to below 40 °C rather than reversing the TEC bias for active cooling. Many TEC manufacturers recommend that the temperature ramping rate should not exceed 1 °C/s. Active cooling at elevated temperatures, e.g. >75 °C to room temperature, has broken a TEC module on the VCSEL setup. The ramp-up and ramp-down procedures described above ensure that the TEC module is operating within recommended limits.

Hundreds of strips of varying length (4-12mm) were cut from the 1.27mm wide by $38\mu\text{m}$ thick roll of solder ribbon by pressing a flat screwdriver tip, like a knife-edge, against the solder laying flat on a work table. Pre-CW and first-generation laser bars were placed on top of a slightly larger solder strip (two parallel strips for longer devices) at the edge of the copper heatsink, which was pre-cleaned with acetone. The heatsink was heated to 125°C for about one minute. The solder melted and due to the weight of the bar, decent bonding was achieved as the stage slowly cooled in the ambient environment. Bonding was performed with and without flux. No noticeable improvement in performance was observed with the flux, which sometimes bubbled during bonding and slightly moved the sample. Thus, flux use was discontinued. To remove samples after testing, the stage is reheated and the sample is picked up with tweezers. Alternatively, at room temperature, a flat screwdriver can be used to simply push the solder and break its bond to the copper heatsink.

Shortly after achieving CW operation in the first generation of lasers, it was calculated and measured that there exists significant longitudinal resistance ($\approx 5\text{-}7\Omega$ along the length of a $20\times 1000\mu\text{m}$ device) due to the thin top p-metal. This could lead to non-uniform current injection along the device length, especially since the total series resistance of the device is around 5Ω . This was immediately remedied by increasing the number of probe contact points from one to three. As the number of probes increased, there was a slight improvement in the threshold density and differential quantum efficiency, but a large improvement in the maximum CW output power and CW operation temperature.

Another improvement in device mounting was to apply pressure during bonding. First, the solder was melted on the copper stage and solidified when the stage was allowed to cool down to 100°C (below the eutectic melting point). Next, the laser bar was placed on the solder and pressure was applied to the bar with probe tips on either end of the bar. The stage was then reheated to 125°C to bond to the sample

and naturally cooled back down. In this approach, a thinner and more uniform solder layer was obtained. The solder rolled up more by the edges, but only to a height that was still well below any epitaxial layers. The main drawback of the solder approach was that only one bar could be mounted on the stage at a time. Mounting a second bar requires heating the stage above the eutectic melting point, thereby deteriorating the quality of the bond for the first bar.

Direct electrical contact of the probes to the copper stage was investigated and 0.3-0.7 Ω of resistance was measured. The high contact resistance was attributed mainly to the surface oxidation of the copper stage. In order to achieve better thermal and electrical contact, oxygen-free copper sub-mounts were incorporated in February 2004. A 6" square sheet, 0.064" thick, of Alloy 101 electronic grade oxygen-free copper (McMaster-Carr part 89675K12) was cut into $\frac{1}{4}$ ", $\frac{3}{8}$ ", and $\frac{1}{2}$ " squares using the large table shear in the Physics Machine shop. It was necessary to stand on the treadle and jump to generate sufficient force and cut this thickness of copper. The squares were soaked in acetone and stored in a N₂ purge box until use. First and second generation laser bars were first mounted onto these sub-mounts using the previously described soldering procedure. Next, a thin coat of GC Electronics Silver Print I was painted on the main copper stage and the sub-mount was glued into place. The print provided excellent thermal and electrical performance when wet or after drying, a few hours later. Sub-mounts were carefully pried off the stage with a razor. The sub-mounts permitted easier storage and remounting of lasers. More importantly, several bars could be mounted for testing simultaneously since the sub-mount bonding could be done on a separate stage, i.e. the VCSEL test station.

The final improvement to the sample mounting techniques was to use the probe tips and their sub-micron precision positioners to place the solder and the sample at the very edge of the copper sub-mount during bonding. If part of the laser hangs over the edge, that portion of the device has worse heat-sinking and electrical contact.

This leads to extra device heating and a redshift of the laser gain peak relative to the rest of the cavity. This increases the threshold density and may contribute to spectral broadening. Conversely, if the sample is too far from the edge, the output beam can be clipped by the heatsink. To find the right balance, the solder and sample were individually positioned at the sub-mount edge. The solder strip was rested on the sub-mount, which was clipped to the VCSEL stage. The probes contacted the sub-mount and then were lifted slightly and used to push the solder just barely beyond the edge of the sub-mount. This ensures the laser can make good contact to the very edge of the copper stage. After the solder was melted and re-solidified on the sub-mount, the sample was placed on the solder (or at least partially straddling the solder and sub-mount) before being pushed to the sub-mount edge. Finally, the probes apply pressure on top of the sample and the solder is re-melted and re-solidified. The sample straddling is important because it is difficult to carefully push the sample from the sub-mount onto the top of the solder with the probes.

Samples with and without MBE growth and processing improvements and with and without device mounting improvements were tested in pulsed and CW mode. With the same device mounting, the first generation devices showed a 3x decrease in pulsed threshold density compared to pre-2003 lasers. However, comparing the first and second generation devices, there was very little change in the maximum pulsed output power at the 3A current limit of the pulse generator, despite the nearly 2x difference in threshold density. Comparing second generation devices with different mountings, there was a 5x improvement in maximum CW output power. Thus, the general conclusion is that better MBE growth and processing greatly improved the threshold density, while better device mounting improved the maximum CW output power.

Future improvements to packaging technology would involve mounting epitaxial side down onto AlN substrates or diamond substrates grown by chemical vapor deposition (CVD). AlN and diamond are electrical insulators. Standard metallizations that can be patterned on these heatsink materials for electrical contact to the lasers are Ti(100)/Pt(200)/Au(5000)/Pt(300)/Au-Sn(3500) or a significantly thinner combination of Ti(100)/W(120)/Ti(40)/Au-Sn(3500), where the thicknesses are in nm. AlN has a 3x higher thermal conductivity than GaAs and a good match in thermal expansion coefficients, which allows the use of high temperature hard solders. The polycrystalline diamond offers over 25x better thermal conductivity than GaAs and is even 3x better than copper; however, the coefficient of expansion's match to GaAs is not as good as AlN's match. Thus, a soft deformable solder, such as 2000nm of IndAlloy 1E or 4 instead of Au-Sn might have to be used as the final metallization layer. However, this generally leads to degradation with time and temperature as the gold of the device contact diffuses into the indium solder layer and forms brittle and thermally resistive intermetallic compounds [126].

We have attempted mounting epitaxial side **up** onto AlN and diamond CVD substrates using IndAlloy 1E. However, the thickness of the GaAs wafer and solder were too large to realize any of the benefits of reduced thermal resistance.

Appendix C

Measuring Relative Intensity Noise With An Electrical Spectrum Analyzer

A basic or scalar electrical spectrum analyzer (ESA), such as the HP8566B used in the relative intensity noise (RIN) measurement, typically measure the magnitude of a voltage signal rather than the in-phase (I) and quadrature (Q) components. This is known as voltage envelope detection. For noise measurements, it is assumed that the voltages v_I and v_Q have independent Gaussian distributions with mean zero and standard deviation σ . The area of voltage space between v and $v+dv$ is $2\pi v dv$ and the probability that $v \leq \sqrt{v_I^2 + v_Q^2} \leq v + dv$ simplifies to:

$$\frac{1}{2\pi\sigma^2} \text{Exp}\left(-\frac{v^2}{2\sigma^2}\right) \quad (\text{C.1})$$

Thus, the probability distribution function (PDF) for the voltage magnitude, v , is given by the Rayleigh distribution (for $v \geq 0$):

$$PDF(v) = \frac{v}{\sigma^2} \text{Exp}\left(-\frac{v^2}{2\sigma^2}\right) \quad (\text{C.2})$$

This distribution peaks at $v=\sigma$ and has the following properties:

$$\begin{aligned}
\int_0^{\infty} PDF(v)dv &= 1 \\
\int_0^{\infty} vPDF(v)dv &= \sigma\sqrt{\frac{\pi}{2}} \\
\int_0^{\infty} v^2PDF(v)dv &= 2\sigma^2
\end{aligned} \tag{C.3}$$

For RIN, we want to measure the ratio of the mean-square optical intensity noise in a 1Hz bandwidth to the square of the DC optical power. Since the electrical power is proportional to the square of the optical power, this is equivalent to the ratio of the time-averaged electrical noise power in a 1Hz bandwidth to the DC electrical power. Thus, our goal is to measure:

$$\bar{P}_e = \left\langle \int_0^{\infty} \frac{v^2(t)}{R} PDF(v)dv \right\rangle = \frac{2\sigma^2}{R} \tag{C.4}$$

where R is the impedance, but the ESA records $v(t)$ and so it will report:

$$\frac{\left\langle \int_0^{\infty} v(t)PDF(v)dv \right\rangle^2}{R} = \frac{\pi\sigma^2}{2R} \tag{C.5}$$

Using Equation C.3, this discrepancy is corrected by multiplying the result by $4/\pi$ or adding 1.05dB.

To cover a wider dynamic range, ESAs typically operate in logarithmic mode, whereby the vertical scale is in decibels rather than linear units, such as Watts. The log amplifier compresses large peaks and expands small signals. As a result, the average noise power is lower than the true noise power (the average of the log < the log of the average). As before, this can be corrected with a correction factor calculated assuming the Rayleigh distribution. The overall correction, for voltage-envelope detection, is to add 2.51dB for logarithmic mode or 1.05dB for linear mode.

Another correction arises from the non-squareness of the resolution bandwidth filter of the ESA. The ideal filter is a flat pass-band with infinite attenuation outside the pass-band. Most ESAs use four-pole synchronously tuned filters to achieve this, which results in a Gaussian like shape pass-band. To correct for this equivalent noise bandwidth, subtract 0.52dB. Also, to normalize to a 1Hz bandwidth, subtract $10 \cdot \text{Log}(\text{RBW})$ where RBW is the set resolution bandwidth in Hz.

Noise measurements are generally difficult to analyze because of the variance in measurements. To reduce this variance, averaging in at least one of three forms is employed. First, one can average the measurements in time by decreasing the video bandwidth or increasing the video averaging. This results in longer sweep times and is acceptable, provided that the laser signal does not drift over time. Second, one can average the measurements in frequency by increasing the resolution bandwidth. This generally shortens the sweep time for a fixed frequency span, but results in signal smearing. Third, one can average adjacent data points, which is similar to increasing the resolution bandwidth with the advantage that error bars for the noise can be calculated if so desired. In the RIN measurement, the noise spectrum is usually sufficiently wide, >500MHz, that the maximum resolution bandwidth setting of the 8566B ESA, 3MHz, can be used and 32 point adjacent averaging can be performed since the data points are usually sufficiently dense that the total frequency spacing of the 32 points does not significantly exceed the resolution bandwidth. A 3 or 10kHz video bandwidth with 1-4 averages is used, resulting in a sweep time around 1 minute.

The MKNOISE function on the ESA performs all of the corrections, including adjacent averaging. In MKNOISE mode, the sweep must first be acquired and then the marker is stepped through the frequency data and the noise at each marker is read to the computer, resulting in incredibly slow data acquisition. Instead, the whole sweep is sent to the computer and the corrections described above are performed there.

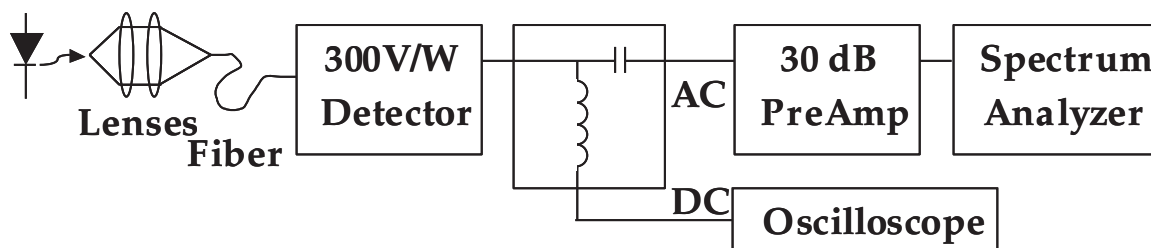


Figure C.1: RIN measurement setup. Laser light is focused onto a single mode fiber and converted to an electrical signal whose AC and DC components are measured separately.

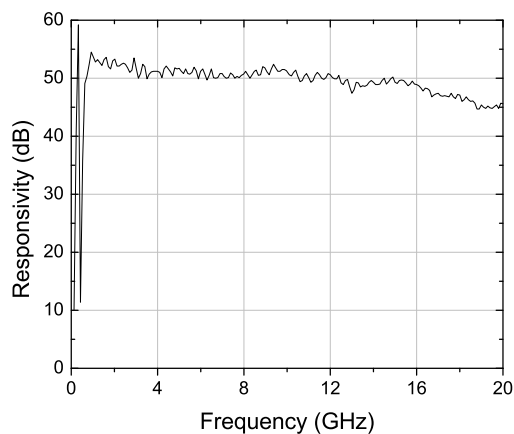


Figure C.2: Overall electrical gain of the RIN measurement system as a function of frequency.

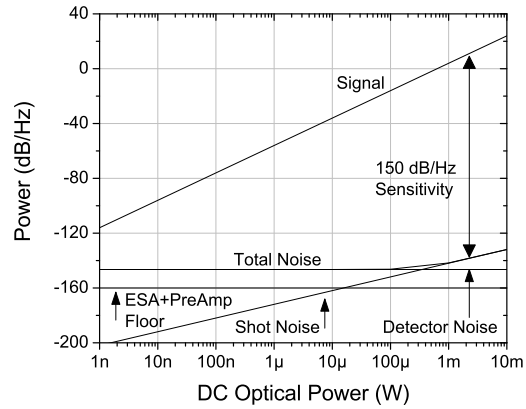


Figure C.3: System noise sources as a function of input DC optical power. The signal increases 20dB per decade. Detector noise is independent of power and is the dominant noise source below 0.5mW. Shot noise increases 10dB per decade and becomes dominant above 1mW.

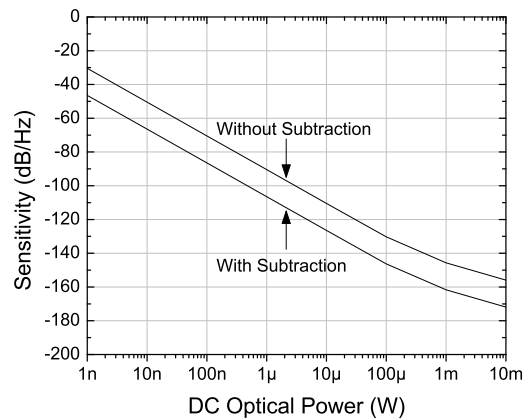


Figure C.4: Overall RIN measurement sensitivity with and without noise subtraction as a function of input DC optical power.

The RIN measurement set-up, shown in Fig. C.1 consists of the Agilent 11982A detector (1200-1600nm, 0-15GHz, 300V/W) followed by Picosecond Pulse Lab 5545 Bias Tee (65kHz-20GHz) and the Agilent 8449B amplifier (1-26.5GHz, ≈ 25 dB gain) and HP 8566B ESA (0-22GHz). Laser light is focused onto a single mode fiber and received by the 11982A detector. The built-in transimpedance amplifier of the detector provides approximately 23dB of gain. The bias tee, connected in reverse, separates the AC and DC signal components. The AC component is sent to the 8449B amplifier and measured with the ESA while the DC component is measured on the oscilloscope. The 8449B amplifier reduces the noise floor of the ESA from -135dB/Hz to -160dB/Hz. The overall system gain was measured as a function of frequency with the Agilent 8703A lightwave component analyzer and is shown in Fig. C.2. The bandwidths for the detector and amplifier limit the frequency range of valid RIN measurements to 0.7-20GHz. The ESA has two different frequency measurement ranges 0-2.5GHz and 2-22GHz and so sequential sweeps in each range and spectrum patching by the computer is performed to obtain full RIN spectra. Fig. C.3 shows the sources of measurement noise, referenced at the input of the 8449B amplifier, as a function of DC optical power. The dominant noise source changes from detector noise to shot noise at 0.5mW. The computer subtracts shot noise from the spectrum after the DC optical power is measured. The system had been calibrated with the 1550nm LED of the Agilent 83437A, a uniform noise source. The computer also subtracts the system's noise floor after collecting the laser-on and laser-off sweeps under the same measurement settings. These two subtractions generally result in a 12-16dB improvement in the measurement sensitivity as shown in Fig. C.4, but create many undefined data points (negative noise) at low laser power levels.

Appendix D

LabView Data Acquisition And Analysis Programs

Various data acquisition and analysis programs were written in LabView, but only the main program, entitled “3840PulsedOSA.vi” will be discussed here. The front panel of the program is shown in Fig. D.1. The program is designed to sweep over a range of currents at a fixed temperature and measure various laser related data and then sweep over a range of temperatures before outputting the acquired data and calculated laser parameters to several text files. Controls (input parameters) have a gray background while indicators (measurement results) have a white background. We will denote control and indicator labels in bold.

A wide range of testing equipment is controlled via the GPIB interface. The top row of controls list the GPIB **Bus** ID and GPIB addresses for the equipment that can be controlled by the program. The list includes the HP70951B optical spectrum analyzer (OSA), ILX Lightwave 3744B current source, 3840LDP pulsed current source, 3722 current source, HP54825A oscilloscope, HP8566B electrical spectrum analyzer (ESA), HP8153A lightwave multimeter, HP34401A digital multimeter, HP8656A signal generator, and Newport 1830C detector.

The **OSA Settings** cluster contains controls for the OSA. The **Center** and **Span** wavelengths are given in nm and the number of data points can be set from 3 to 2048

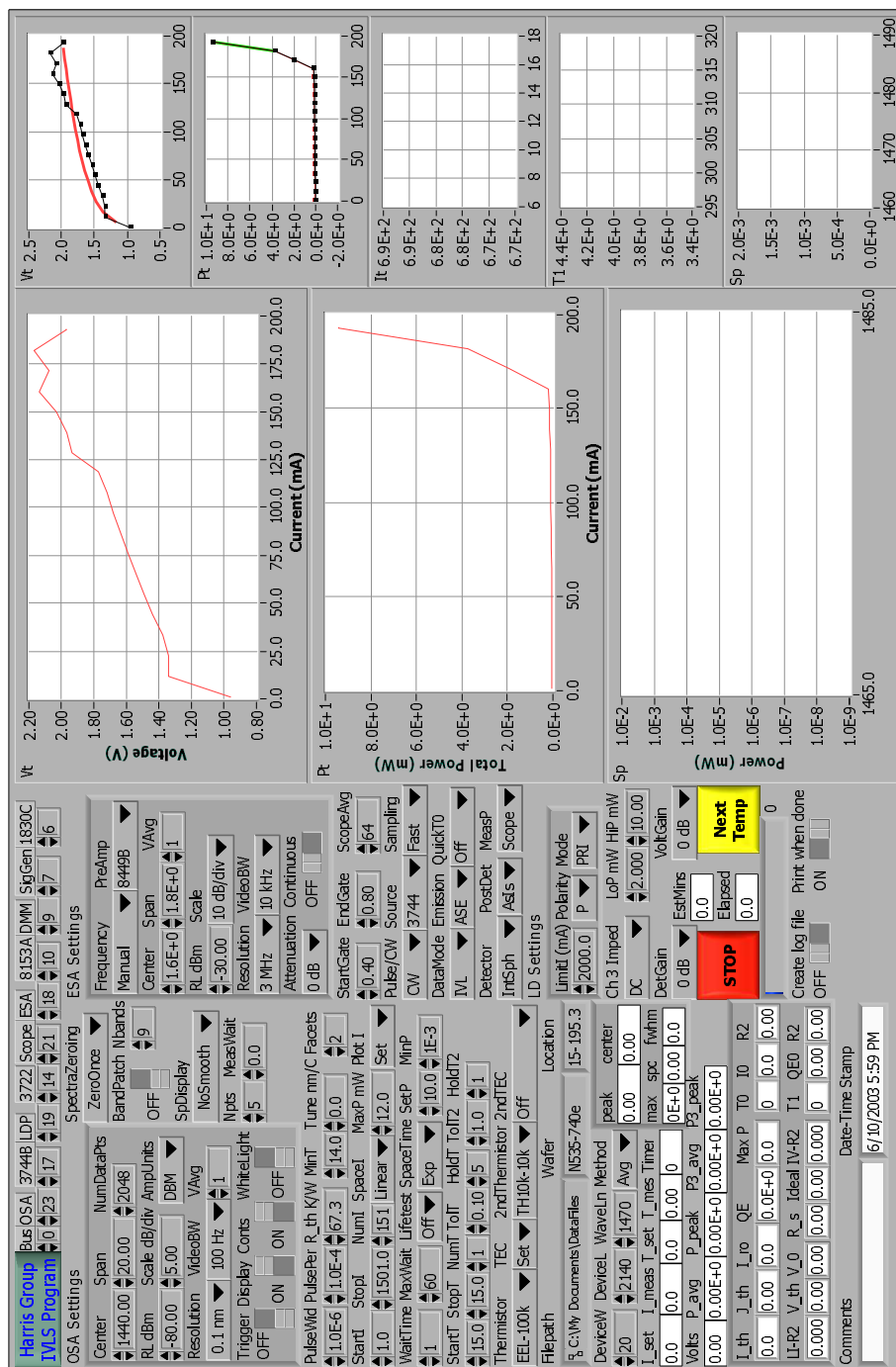


Figure D.1: (Color) LabView main program front panel with L-I-V data from our 1st CW laser.

(usually 2048). The program usually ignores the next line since the reference level (top of screen), amplitude scale in dB/division, and amplitude units are auto-scaled in the program based on the measurement signal. The **Resolution** bandwidth determines how closely in wavelengths two peaks can be resolved. A narrow bandwidth leads to a weak signal power. The resolution bandwidth should be around 1% of the span. Smaller bandwidths cause the sweep to take excessively long and the data points are spaced out by too much to resolve spectral features anyways. Larger bandwidths lead to unnecessary smearing out of spectral data. The **VideoBW** determines how long the OSA integrates a measurement point in time. Small video bandwidth reduces the noise floor but makes the sweep time longer. Video averaging (**VAvg**) lets the analyzer sweep several times and average before returning a spectrum. The last line is rarely used, except for the built in white-light source of the OSA.

To the right of **OSA Settings** are the controls **SpectraZeroing** for subtraction of the data with the laser off, **BandPatch** for extending the span of a spectra by performing sweeps over a narrow range and then patching the data together on the computer, **SpDisplay** for smoothing of the spectrum displayed, and **MeasWait** for a time delay between measurements.

The **ESA Settings** cluster is similar to the **OSA Settings** cluster. **Frequency** can either be set manually or on a pre-selected frequency band. The program corrects for a pre-amplifier (**PreAmp**). Electrical signals with a DC component need to be blocked by a suitable capacitor prior to the ESA input or attenuated by at least 10dB by the ESA.

The line of controls below the **OSA Settings** cluster has pulse width and period settings. A thermal resistance may be entered for testing at fixed active region temperature; the program will stop if the set temperature falls below **MinT**. **Tune nm/C** adjusts the OSA center wavelength to keep the spectrum in the measurement window

as the temperature varies. **Facets** multiplies the measured power to obtain the total power.

The next line contains **StartI**, **StopI**, **NumI**, and **SpaceI** to determine how the current is ramped. The program stops if **MaxP** is reached. **PlotI** determines whether the set or measured current is plotted and used for calculating thresholds and efficiencies.

The next line is for reliability testing. **WaitTime**, **MaxWait**, and **SpaceTime** set how frequently data is acquired during life testing. **Lifetest** can be turned off, or operate in constant current or constant power modes. **SetP** is the desired set point for constant power operation. If the power falls below **MinP** in either life test mode or if the current rises above **LimitI** (inside the **LD Settings** cluster on the lower right of the screen) in constant power mode, the program will stop.

The next line has controls for the temperature ramping. **StartT**, **StopT**, **NumT** determine how the current is ramped. **ToIT**, **HoldT**, **ToIT2**, **HoldT2** determine how closely and for how long the temperature of each stage must stabilize to the set temperature before the program continues. The **Thermistor**, **TEC**, **2ndThermistor**, and **2ndTEC** determine which stage is being used and whether a stage should be on, off, held at a set temperature even after the program finishes, or actively adjusting to maintain constant active region temperature.

The next line sets the file paths and names for the scan. Files are created with **Wafer** and **Location** in the title and placed in the **Filepath** directory. The next half-line is for entering the device dimensions **DeviceW** & **DeviceL** and wavelength and whether to analyze the peak power or gated average of the pulsed waveform. **Comments**, way at the bottom, is a control that will save user comments as part of the settings file.

Moving to the right, below **ESA Settings**, are controls for **StartGate** and **EndGate**, which determine where in the pulsed waveform is gated for measurement.

ScopeAvg sets how many averages the scope performs at each measurement. The line below has **Pulse/CW** that sets pulsed or CW mode, **Source** that chooses which CW current controller is used, and **Sampling** that sets whether the scope is in fast scan or high-resolution mode.

DataMode is one of the most important controls. It sets whether a simple L-I-V scan is performed, an L-I-V with optical spectrum, an L-I-V with electrical spectrum (for RIN) or an L-I-V with small signal modulation. The program only uses **Emission** to put an identifier in the file name depending on what type of measurement is made. **QuickT0** is rarely used, but allows the T_0 measurement to be made quickly by not restarting each L-I-V from **StartI**, but rather from a set amount below the last threshold as the temperature is increased.

Detector tells the program which calibration to use and whether to communicate with auxiliary detectors, such as the 8153A. **PostDet** adjusts calibration depending on whether there is a reverse bias tee after the detector and **MeasP** tells whether the power will be measured by the scope or a DMM.

The **LD Settings** cluster has the current limit **LimitI** for all current controllers, the **Polarity** and **Mode**, which only apply to the pulsed source. **Ch 3 Imped** sets the scope's input impedance for power measurements. **LoP** and **HiP** set the range of currents over which the threshold and efficiency are calculated. The algorithm to determine threshold is (1) find the maximum in the L-I curve and cut off data for currents beyond the maximum, (2) find the location where the slope of the L-I curve significantly changes and cut off data for currents below this point, and (3) limit the current range to those specified by **LoP** and **HiP** and then perform a linear fit on the remaining data. **DetGain** and **VoltGain** are used to account for any additional detector or post detector gains. **Stop** and **NextTemp** allow the program to be stopped completely or to move on to the next temperature while saving the data and turning necessary instruments off. It is important to use these controls

rather than the stop button at the top of the program if data needs to be saved or instruments need to exit. The last two controls are **Create log file**, which is invaluable for protecting and viewing data collected during long reliability tests and **Print when done**, which does exactly that.

The indicators begin with **I_set**, **I_meas**, **T_set**, **T_meas**, **Timer**, **Volts**, **P_avg**, **P_peak**, **P3_avg**, and **P3_peak**, which give the present readings. Though it is not a cluster, we will call this set of values **PresentReadings**. In the cluster to the right of this, which has a hidden label **PeakInfo**, there are controls **peak**, **center**, **max**, **spc**, and **fwhm** that give the peak and center of the spectrum, the maximum amplitude, the spacing between Fabry-Pérot modes and the full width at half maximum of the spectrum.

The next cluster of indicators has a hidden label **Characteristics** and contains **I_th**, **J_th**, **I_ro**, **QE**, **MaxP**, **LI-R2**, **V_th**, **V_0**, **R_s**, **Ideal**, **IV-R2**, which are the threshold current, threshold density, rollover current (location of maximum power), quantum efficiency, maximum power, R^2 value for the L-I linear fit, threshold voltage, V_0 parameter defined in Section 5.1, series resistance, ideality factor, and R^2 value for the I-V non-linear fit. These parameters are all for a specific temperature. To the right of them is **T0**, **I0**, **R2**, **T1**, **QE0**, **R2**, which are the values of T_0 , threshold current at a reference temperature (taken to be 0K), R^2 value for the $\ln(J_{th})$ vs T linear fit used to determine T_0 , the value of T_1 , the quantum efficiency at the reference temperature, and the R^2 value for the $\ln(\eta_e)$ vs T linear fit used to determine T_1 . The other three indicators are **Date-Time Stamp**, **EstMins**, and **Elapsed**, which tell when the program was started, an estimate of how many minutes remain, and the elapsed time in minutes.

The graphs display V-I, L-I, spectra, V-t, L-t, I-t, T_0 , T_1 and a few other curves. The program generates three to five types of output files. The .set file contains information on the settings used. The .t0 file contains the values of the **Characteristics**

cluster for each temperature as well as the calculated values for T_0 and T_1 . The .ivl files (1 per temperature) contain the values of **PresentReadings**. For optical (or electrical) spectra, there will also be .spo (.spe) which contain the spectra and .peaks (.peake) which contain the values of **PeakInfo**. Each file includes the sample identification and date time stamp at the top.

Appendix E

List Of Acronyms

Table E.1: List of Acronyms

Acronym	Description
AR	Anti-Reflective
ARO	Army Research Office
ASE	Amplified Spontaneous Emission
BAC	Band Anti-Crossing
BGR	Bandgap Renormalization
CHCC	(C=conduction, H=heavy hole) Auger process
CHHS	(C=conduction, H=heavy hole, S=split-off) Auger process
COMD	Catastrophic Optical Mirror Damage
CVD	Chemical Vapor Deposition
CW	Continuous wave
CWDM	Coarse Wavelength Division Multiplexing
DARPA	Defense Advanced Research Projects Agency
DBR	Distributed Bragg Reflector
DFB	Distributed Feedback

Continued on next page

Acronym	Description
DQW	Double Quantum Well
DWDM	Dense Wavelength Division Multiplexing
EDFA	Erbium Doped Fiber Amplifier
ESA	Electrical Spectrum Analyzer
FCA	Free Carrier Absorption
FFT	Fast Fourier Transform
FIB	Focused Ion Beam
FWHM	Full Width Half Maximum
HR	High Reflective
ISI	Intersymbol interference
ITU	International Telecommunication Union
IVBA	Intervalence Band Absorption
MARCO	Microelectronics Advanced Research Corporation
MBE	Molecular Beam Epitaxy
MQW	Multiple Quantum Well
NPSC	National Physical Science Consortium
NSF	National Science Foundation
NRZ	Non-Return to Zero
OSA	Optical Spectrum Analyzer
PARC	Palo Alto Research Center (Xerox)
PASE	Partially Amplified Spontaneous Emission
PDF	Probability Distribution Function
PR	Photorefectance
QCSE	Quantum Confined Stark Effect
QW	Quantum Well

Continued on next page

Acronym	Description
RBW	Resolution Bandwidth
RIN	Relative Intensity Noise
RT	Room Temperature
RTA	Rapid Thermal Annealing
SCH	Separate Confinement Heterostructure
SFDR	Spurious Free Dynamic Range
SNRC	Stanford Network Research Center
SPRC	Stanford Photonics Research Center
SQW	Single Quantum Well
SRS	Stimulated Raman Scattering
TDM	Time Division Multiplexing
TE	Transverse Electric
TEC	Thermo-Electric Cooler
TIA	Transimpedance Amplifier
TM	Transverse Magnetic
TSE	True Spontaneous Emission
VBW	Video Bandwidth
VCSEL	Vertical-Cavity Surface-Emitting Laser
WDM	Wavelength Division Multiplexing

References

- [1] URL http://www.nua.ie/surveys/how_many_online/index.html
- [2] URL http://www.mrv.com/wdm/tech_cwdm.php
- [3] G. Agrawal, *Fiber-Optic Communication Systems* (Wiley, New York, 2002), 1st ed., p6.
- [4] M. Shimizu, M. Yamada, H. Horiguchi, T. Takeshita, and M. Okayasu, “Erbium-doped fibre amplifiers with an extremely high gain coefficient of 11.0 dB/mW,” *Electron. Lett.* **26**, 1641–1643 (1990).
- [5] V. Alwayn, *Optical Network Design and Implementation* (Cisco Press, 2004), 1st ed., pp70–73.
- [6] H. Soda, K. Iga, C. Kitahara, and Y. Suematsu, “GaInAsP/InP surface emitting injection lasers,” *Jpn. J. Appl. Phys.* **18**, 2329–2330 (1979).
- [7] V. Jayaraman, J. Geske, M. MacDougal, F. Peters, T. Lowers, and T. Char, “Uniform threshold current, continuous-wave, singlemode 1300 nm vertical cavity lasers from 0 to 70 degrees C,” *Electron. Lett.* **34**, 1405–1407 (1998).
- [8] W. Yuen, G. Li, R. Nabiev, J. Boucart, P. Kner, R. Stone, D. Zhang, M. Beaudoin, T. Zheng, C. He, et al., “High-performance 1.6 μm single-epitaxy top-emitting VCSEL,” *Electron. Lett.* **36**, 1121–1123 (2000).

- [9] E. Hall, G. Almuneau, J. Kim, O. Sjolund, H. Kroemer, and L. Coldren, “Electrically-pumped, single-epitaxial VCSELs at 1.55 μm with Sb-based mirrors,” *Electron. Lett.* **35**, 1337–1338 (1999).
- [10] S. Uchiyama, N. Yolouchi, and T. Ninomiya, “Continuous-wave operation up to 36 degrees C of 1.3- μm GaInAsP-InP vertical-cavity surface-emitting laser,” *IEEE Photon. Tech. Lett.* **9**, 141–142 (1997).
- [11] J. Lott, N. Ledentsov, V. Ustinov, Z. Alferov, and D. Bimberg, “InAs-InGaAs quantum dot VCSELs on GaAs substrates emitting at 1.3 μm ,” *2000 Memoirs of the Institute of Scientific and Industrial Research Osaka* **57**, 80–87 (2000).
- [12] O. Blum and J. Klem, “Characteristics of GaAsSb single-quantum-well-lasers emitting near 1.3 μm ,” *IEEE Photon. Tech. Lett.* **12**, 771–773 (2000).
- [13] M. Kondow, K. Uomi, A. Niwa, T. Kitatani, S. Watahiki, and Y. Yazawa, “Gas-source molecular beam epitaxy of $\text{GaN}_x\text{As}_{1-x}$ using a N radical as the N source,” *Jpn. J. Appl. Phys.* **33**, L1056–L1058 (1994).
- [14] M. Kondow, K. Uomi, A. Niwa, T. Kitatani, S. Watahiki, and Y. Yazawa, “GaInNAs: a novel material for long-wavelength-range laser diodes with excellent high-temperature performance,” *Jpn. J. Appl. Phys.* **35**, 1273–1275 (1996).
- [15] I. Vurgaftman and J. Meyer, “Band parameters for nitrogen-containing semiconductors,” *J. Appl. Phys.* **94**, 3675–3696 (2003).
- [16] X. Yang, M. Jurkovic, J. Heroux, and W. Wang, “Molecular beam epitaxial growth of InGaAsN:Sb/GaAs quantum wells for long-wavelength semiconductor lasers,” *Appl. Phys. Lett.* **75**, 178–180 (1999).

- [17] H. Shimizu, K. Kumada, S. Uchiyama, and A. Kasukawa, “High Performance CW 1.26 μm GaInNAsSb-SQW and 1.20 μm GaInAsSb-SQW Ridge Lasers,” *Electron. Lett.* **36**, 1701–1703 (2000).
- [18] V. Gambin, W. Ha, M. Wistey, H. Yuen, S. Bank, S. Kim, and J. S. Harris Jr., “GaInNAsSb for 1.3-1.6 μm long wavelength lasers grown by molecular beam epitaxy,” *IEEE J. Sel. Top. Quantum Electron.* **8**, 795–800 (2002).
- [19] M. Kondow, S. Nakatsuka, T. Kitatani, Y. Yazawa, and M. Okai, “Room-temperature continuous-wave operation of GaInNAs/GaAs laser diode,” *Electron. Lett.* **32**, 2244–2245 (1996).
- [20] M. Hetterich, M. Dawson, A. Egorov, D. Bernklau, and H. Riechert, “Electronic states and band alignment in GaInNAs/GaAs quantum-well structures with low nitrogen content,” *Appl. Phys. Lett.* **76**, 1030–1032 (2000).
- [21] M. Kondow, T. Kitatani, S. Nakatsuka, M. C. Larson, K. Nakahara, Y. Yazawa, M. Okai, and K. Uomi, “GaInNAs: a Novel Material for Long-wavelength Semiconductor Lasers,” *IEEE J. Sel. Top. Quantum Electron.* **3**, 719–730 (1997).
- [22] N. Tansu and L. Mawst, “Low-threshold Strain-compensated InGaAs(N) ($\lambda = 1.19\text{-}1.31 \mu\text{m}$) Quantum-well Lasers,” *IEEE Photon. Technol. Lett.* **14**, 444–446 (2002).
- [23] W. Ha, V. Gambin, S. Bank, M. Wistey, H. Yuen, S. Kim, and J. S. Harris Jr., “Long-wavelength GaInNAs(Sb) Lasers on GaAs,” *IEEE J. Quantum Electron.* **38**, 1260–1267 (2002).
- [24] L. Li, V. Sallet, G. Patriarche, L. Largeau, S. Bouchoule, K. Merghem, L. Travers, and J. C. Harmand, “1.5 μm Laser on GaAs with GaInNAsSb Quinary Quantum Well,” *Electron. Lett.* **39**, 519–520 (2003).

- [25] D. Gollub, S. Moses, M. Fischer, and A. Forchel, “1.42 μm Continuous-wave Operation of GaInNAs Laser Diodes,” *Electron. Lett.* **39**, 777–778 (2003).
- [26] S. Bank, M. Wistey, H. Yuen, L. Goddard, W. Ha, and J. S. Harris Jr., “Low-threshold CW GaInNAsSb/GaAs Laser at 1.49 μm ,” *Electron. Lett.* **39**, 1445–1446 (2003).
- [27] S. Bank, M. Wistey, L. Goddard, H. Yuen, V. Lordi, and J. S. Harris Jr., “Low-threshold continuous-wave 1.5- μm GaInNAsSb lasers grown on GaAs,” *IEEE J. Quantum Electron.* **40**, 656–664 (2004).
- [28] S. Bank, M. Wistey, L. Goddard, H. Yuen, H. Bae, and J. S. Harris Jr., “High-performance 1.5 μm GaInNAsSb Lasers Grown on GaAs,” *Electron. Lett.* **40**, 1186–1187 (2004).
- [29] R. Averbeck, G. Jaschke, L. Geelhaar, and H. Riechert, “Low threshold InGaAsN/GaAs lasers beyond 1500 nm,” *ICMBE Conference*, Edinburgh, Scotland (2004).
- [30] C. Coldren, M. Larson, S. Spruytte, and J. S. Harris, “1200 nm GaAs-based Vertical Cavity Lasers Employing GaInNAs Multiquantum Well Active Regions,” *Electron. Lett.* **36**, 951–952 (2000).
- [31] K. Choquette, J. Klem, A. Fischer, O. Blum, A. Allerman, I. Friz, S. Kurz, W. B. R. Sieg, K. Geib, J. Scott, et al., “Room Temperature Continuous Wave InGaAsN Quantum Well Vertical-cavity Lasers Emitting at 1.3 μm ,” *Electron. Lett.* **36**, 1388–1390 (2000).
- [32] G. Steinle, H. Riechert, and A. Y. Egorov, “Monolithic VCSEL with InGaAsN Active Region emitting at 1.28 μm and CW Output Power Exceeding 500 μW at Room Temperature,” *Electron. Lett.* **37**, 93–95 (2001).

- [33] T. Takeuchi, Y. Chang, M. Leary, A. Tandon, H. Luan, D. Bour, S. Corzine, R. Twist, and M. Tan, “1.3 μm InGaAsN Vertical Cavity Surface Emitting Lasers Grown by MOCVD,” *Electron. Lett.* **38**, 1438–1440 (2002).
- [34] M. Wistey, S. Bank, H. Yuen, L. Goddard, and J. S. Harris, “Monolithic, GaInNAsSb VCSELs at 1.46 μm on GaAs by MBE,” *Electron. Lett.* **39**, 1822–1823 (2003).
- [35] M. Reinhard, M. Fischer, M. Kamp, J. Hofmann, and A. Forchel, “1.3- μm GaInNAs–AlGaAs Distributed Feedback Lasers,” *IEEE Photon. Tech. Lett.* **12**, 239–241 (2000).
- [36] D. Gollub, M. Kamp, A. Forchel, J. Seufert, S. Bank, M. Wistey, L. Goddard, H. Yuen, and J. S. Harris, “Continuous-Wave Operation of GaInNAsSb Distributed Feedback Lasers at 1.5 μm ,” *Electron. Lett.* **37**, 1487–1488 (2004).
- [37] L. Goddard, S. Bank, M. Wistey, H. Yuen, H. Bae, and J. S. Harris Jr., “Reduced Monomolecular Recombination in GaInNAsSb/GaAs Lasers at 1.5 μm ,” *LEOS Conference*, Rio Grande, PR, session MO 6, (2004).
- [38] M. Wistey, S. Bank, H. Yuen, and J. S. Harris, “Reduced Damage During Growth of GaInNAs Using Low Voltage Ion Deflection Plates,” submitted to *Appl. Phys. Lett.*
- [39] M. Wistey, S. Bank, H. Yuen, L. Goddard, and J. S. Harris, “Protecting Wafer During Plasma Ignition by Use of an Arsenic Cap,” submitted to *J. Vac. Sci. & Tech. B.*
- [40] S. Bank, M. Wistey, H. Yuen, L. Goddard, H. Bae, and J. S. Harris, “MBE Growth of Low-Threshold CW GaInNAsSb Lasers at 1.5 μm ,” submitted to *J. Vac. Sci. & Tech. B.*

- [41] R. Fehse, S. Jin, S. Sweeney, A. Adams, E. O'Reilly, H. Riechert, S. Illek, and A. Egorov, "Evidence for large monomolecular recombination contribution to threshold current in 1.3 μm GaInNAs semiconductor lasers," *Electron. Lett.* **37**, 1518–1520 (2001).
- [42] R. Fehse, S. Tomic, A. Adams, S. Sweeney, E. O'Reilly, A. Andreev, and H. Riechert, "A quantitative study of radiative, Auger, and defect related recombination processes in 1.3- μm GaInNAs-based quantum-well lasers," *IEEE J. Sel. Top. Quantum Electron.* **8**, 801–810 (2002).
- [43] A. Phillips, S. Sweeney, A. Adams, and P. Thijs, "The temperature dependence of 1.3- and 1.5- μm compressively strained InGaAs(P) MQW semiconductor lasers," *IEEE J. Sel. Top. Quantum Electron.* **5**, 401–412 (1999).
- [44] H. Riechert, A. Egorov, D. Livshits, B. Borchert, and S. Illek, "InGaAsN/GaAs heterostructures for long-wavelength light-emitting devices," *Nanotechnology* **11**, 201–205 (2000).
- [45] D. Livshits, A. Egorov, and H. Riechert, "8W continuous wave operation of InGaAsN lasers at 1.3 μm ," *Electron. Lett.* **36**, 1381–1382 (2000).
- [46] M. Kondow, T. Kitatani, K. Nakahara, and T. Tanaka, "A 1.3- μm GaInNAs laser diode with a lifetime of over 1000 hours," *Jpn. J. Appl. Phys. Part 2* **38**, L1355–L1356 (1999).
- [47] M. Itoh, H. Sugiura, H. Yasaka, Y. Kondo, K. Kishi, M. Fukuda, and Y. Itaya, "Differential gain and threshold current of 1.3 μm tensile-strained InGaAsP multi quantum well buried-heterostructure lasers grown by metalorganic molecular beam epitaxial growth," *Appl. Phys. Lett.* **72**, 1553–1555 (1998).

- [48] I. Vurgaftman, J. Meyer, and L. Ram-Mohan, “Band parameters for III-V compound semiconductors and their alloys,” *J. Appl. Phys.* **89**, 5815–5875 (2001).
- [49] P. Thijs, L. Tiemeijer, P. Kuindersma, J. Binsma, and T. Dongen, “High-performance 1.5 μm wavelength InGaAs-InGaAsP strained quantum well lasers and amplifiers,” *IEEE J. Quantum Electron.* **27**, 1426–1439 (1991).
- [50] J. Bardeen, “An improved calculation of the energies of metallic Li and Na,” *J. Chem. Phys.* **6**, 367–371 (1938).
- [51] F. Seitz, *The Modern Theory of Solids* (McGraw Hill, New York, 1940), 1st ed., p352.
- [52] J. Slater and G. Koster, “Simplified LCAO method for the periodic potential problem,” *Phys. Rev.* **94**, 1498–1524 (1954).
- [53] J. Phillips and L. Kleinman, “New method for calculating wave functions in crystals and molecules,” *Phys. Rev.* **116**, 287–294 (1959).
- [54] G. Pikus and G. Bir, “Effects of deformation on the hole energy spectrum of germanium and silicon,” *Sov. Phys.-Solid State* **1**, 1502–1517 (1960).
- [55] G. Bir and G. Pikus, *Symmetry and Strain-Induced Effects in Semiconductors* (Wiley, New York, 1974).
- [56] S. Chuang, *Physics of Optoelectronic Devices* (Wiley, New York, 1995), 1st ed., p137.
- [57] S. Chuang, *Physics of Optoelectronic Devices* (Wiley, New York, 1995), 1st ed., p660.
- [58] S. Chuang, *Physics of Optoelectronic Devices* (Wiley, New York, 1995), 1st ed., p661.

- [59] S. Chuang, “Efficient band-structure calculations of strained quantum wells using a two-by-two Hamiltonian,” *Phys. Rev. B* **43**, 9649–9661 (1991).
- [60] S. Chuang, *Physics of Optoelectronic Devices* (Wiley, New York, 1995), 1st ed., pp148–149.
- [61] S. Chuang, *Physics of Optoelectronic Devices* (Wiley, New York, 1995), 1st ed., pp156–157.
- [62] T. Ostromek, “Evaluation of matrix elements of the 8×8 $\mathbf{k} \cdot \mathbf{p}$ Hamiltonian with \mathbf{k} -dependent spin-orbit contributions for the zinc-blende structure of GaAs,” *Phys. Rev. B* **54**, 14467–14479 (1996).
- [63] S. Chuang, *Physics of Optoelectronic Devices* (Wiley, New York, 1995), 1st ed., p186.
- [64] J. Vechten and K. Malloy, “The temperature dependence of band offsets for semiconductor heterojunctions in general and for the particular cases of AlAs-GaAs and HgTe-CdTe,” *J. Phys. Condens. Matter* **2**, 281–293 (1990).
- [65] W. Shan, W. Walukiewicz, J. Ager, E. Haller, J. Geisz, D. Friedman, J. Olson, and S. Kurtz, “Effect of nitrogen on the band structure of GaInNAs alloys,” *J. Appl. Phys.* **86**, 2349–2351 (1999).
- [66] A. Allred, “Electronegativity values from thermochemical data,” *J. Inorg. Nucl. Chem.* **17**, 215–221 (1961).
- [67] A. Allred and A. Hensley, “Electronegativities of Nitrogen, Phosphorus, Arsenic, Antimony, and Bismuth,” *J. Inorg. Nucl. Chem.* **17**, 43–54 (1961).
- [68] W. Shan, W. Walukiewicz, J. Ager, E. Haller, J. Geisz, D. Friedman, J. Olson, and S. Kurtz, “Band anticrossing in GaInNAs alloys,” *Phys. Rev. Lett.* **82**, 1221–1224 (1999).

- [69] S. Tomic, E. O'Reilly, P. Klar, H. Gruning, W. Heimbrodt, W. Chen, and I. Buyanova, "Influence of conduction-band nonparabolicity on electron confinement and effective mass in $\text{GaN}_x\text{As}_{1-x}/\text{GaAs}$ quantum wells," *Phys. Rev. B* **69**, 245305-1-12 (2004).
- [70] S. Choulis, T. Hosea, S. Tomic, M. Kamal-Saadi, A. Adams, E. O'Reilly, B. Weinstein, and P. Klar, "Electronic structure of $\text{In}_y\text{Ga}_{1-y}\text{As}_{1-x}\text{N}_x/\text{GaAs}$ multiple quantum wells in the dilute-N regime from pressure and $\mathbf{k} \cdot \mathbf{p}$ studies," *Phys. Rev. B* **66**, 165321-1-9 (2002).
- [71] A. Polimeni, M. Capizzi, M. Geddo, M. Fischer, M. Reinhardt, and A. Forchel, "Effect of nitrogen on the temperature dependence of the energy gap in $\text{In}_x\text{Ga}_{1-x}\text{As}_{1-y}\text{N}_y/\text{GaAs}$ single quantum wells," *Phys. Rev. B* **63**, 195320-1-5 (2001).
- [72] Z. Pan, L. Li, Y. Lin, B. Sun, D. Jiang, and W. Ge, "Conduction band offset and electron effective mass in $\text{GaInNAs}/\text{GaAs}$ quantum-well structures with low nitrogen concentration," *Appl. Phys. Lett.* **78**, 2217-2219 (2001).
- [73] H. Sun, M. Dawson, M. Othman, J. Yong, J. Rorison, P. Gilet, L. Grenouillet, and A. Million, "Optical transitions in $\text{GaInNAs}/\text{GaAs}$ multi-quantum wells with varying N content investigated by photoluminescence excitation spectroscopy," *Appl. Phys. Lett.* **82**, 376-378 (2003).
- [74] L. Goddard, S. Bank, M. Wistey, H. Yuen, Z. Rao, and J. S. Harris Jr., "Recombination, Gain, Band Structure, Efficiency, and Reliability of $1.5\text{-}\mu\text{m}$ $\text{GaInNAsSb}/\text{GaAs}$ Lasers," accepted for publication in *J. Appl. Phys.*
- [75] S. Spruytte, M. Larson, W. Wampler, C. Coldren, H. Peterson, and J. S. Harris, "Nitrogen incorporation in group III-nitride-arsenide materials grown by

- elemental source molecular beam epitaxy,” *J. Crystal Growth* **227-228**, 506–515 (2001).
- [76] S. Spruytte, *MBE Growth of Nitride-Arsenides for Long-wavelength Optoelectronics* (Ph.D. thesis, Stanford University, 2001).
- [77] M. Wistey, S. Bank, H. Yuen, and J. S. Harris, “Real-Time Ion Count from Nitrogen Plasma Source,” *North American MBE Conference*, session P2-9, (2003).
- [78] P. Krispin, V. Gambin, J. S. Harris, and K. Ploog, “Nitrogen-related electron traps in Ga(As,N) layers ($\leq 3\%$ N),” *J. Appl. Phys.* **93**, 6095–6099 (2003).
- [79] S. Chuang, *Physics of Optoelectronic Devices* (Wiley, New York, 1995), 1st ed., p351.
- [80] D. Ahn and S. Chuang, “The theory of strained-layer quantum-well lasers with bandgap renormalization,” *IEEE J. Quantum Electron.* **30**, 350–365 (1994).
- [81] A. Haug, “Relations between the T_0 values of bulk and quantum-well GaAs,” *Appl. Phys. B: Photophys. Laser Chem.* **44**, 151–153 (1987).
- [82] J. Thomson, H. Summers, P. Hulyer, P. Snowton, and P. Blood, “Determination of single-pass optical gain and internal loss using a multisection device,” *Appl. Phys. Lett.* **75**, 2527–2529 (1999).
- [83] M. Ya, Y. Chen, and Y. Huang, “Nonlinear behaviors of valence-band splitting and deformation potential in dilute GaN_xAs_{1-x} alloys,” *J. Appl. Phys.* **92**, 1446–1449 (2002).
- [84] Y. Zhang, A. Mascarenhas, H. Xin, and C. Tu, “Valence-band splitting and shear deformation potential of dilute GaAs_{1-x}N_x alloys,” *Phys. Rev. B* **61**, 4433–4436 (2000).

- [85] H. Schneider and K. v. Klitzing, “Thermionic emission and Gaussian transport of holes in a GaAs/Al_xGa_{1-x}As multiple-quantum-well structure,” *Phys. Rev. B* **38**, 6160–6165 (1988).
- [86] R. Kudrawiec, H. Yuen, K. Ryczko, J. Misiewicz, S. Bank, M. Wistey, H. Bae, and J. S. Harris Jr., “Photorefectance and photoluminescence investigations of a step-like GaInNAsSb/GaAsN/GaAs quantum well tailored at 1.5 μm : the energy level structure and the Stokes shift,” *J. Appl. Phys.* **97**, 053515-1–7 (2005).
- [87] L. Coldren and S. Corzine, *Diode Lasers and Photonic Integrated Circuits* (Wiley, New York, 1995), 1st ed., p138.
- [88] L. Goddard, S. Bank, M. Wistey, H. Yuen, and J. S. Harris Jr., “High performance GaInNAsSb/GaAs lasers at 1.5 μm ,” accepted for publication in *Proc. SPIE* **5738**-23.
- [89] S. Chuang, *Physics of Optoelectronic Devices* (Wiley, New York, 1995), 1st ed., pp427–428.
- [90] P. Smowton and P. Blood, “The differential efficiency of quantum well lasers,” *IEEE J. Sel. Top. Quantum Electron.* **3**, 491–498 (1997).
- [91] P. Smowton and P. Blood, “On the determination of internal optical mode loss of semiconductor lasers,” *Appl. Phys. Lett.* **70**, 2365–2367 (1997).
- [92] S. Bank, L. Goddard, M. Wistey, H. Yuen, and J. S. Harris Jr., “On the temperature sensitivity of 1.5 μm GaInNAsSb lasers,” submitted to *IEEE J. Sel. Top. Quantum Electron.*
- [93] S. Sweeney, A. Phillips, A. Adams, E. O’Reilly, and P. Thijs, “The effect of temperature dependent processes on the performance of 1.5- μm compressively

- strained InGaAs(P) MQW semiconductor diode lasers,” *IEEE Photonic. Tech. L.* **10**, 1076–1078 (1998).
- [94] L. Goddard, S. Bank, M. Wistey, H. Yuen, and J. S. Harris Jr., in *CLEO/IQEC and PhAST Technical Digest on CD-ROM (The Optical Society of America)* (Washington, DC, 2004), session CTuP22.
- [95] R. Olshansky, C. Su, J. Manning, and W. Powazinik, “Measurement of radiative and nonradiative recombination rates in InGaAsP and AlGaAs light sources,” *IEEE J. Quantum Electron.* **QE-20**, 838–854 (1984).
- [96] D. Bour, D. Treat, R. Thornton, R. Geels, and D. Welch, “Drift leakage current in AlGaInP quantum-well lasers,” *IEEE J. Quantum Electron.* **29**, 1337–1343 (1993).
- [97] V. Chazapis, H. Blom, K. Vodopyanov, A. Norman, and C. Phillips, “Midinfrared picosecond spectroscopy studies of Auger recombination in InSb,” *Phys. Rev. B* **52**, 2516–2521 (1995).
- [98] N. Dutta, “Calculation of Auger rates in a quantum well structure and its application to InGaAsP quantum well lasers,” *J. Appl. Phys.* **54**, 1236–1245 (1983).
- [99] A. Haug, “Carrier density dependence of Auger recombination,” *Solid State Electron.* **21**, 1281–1284 (1978).
- [100] A. R. Adams (personal communication, 2004).
- [101] A. Haug, “Band-to-band Auger recombination in semiconductors,” *J. Phys. Chem. Solids* **49**, 599–605 (1988).

- [102] S. Prakash, L. Chirovsky, R. Naone, D. Galt, D. Kisker, and A. Jackson, "Reliability of 1.3 micron VCSELs for metro area networks," *Proc. SPIE* **4994**, 44–54 (2003).
- [103] N. Tansu, Y. Chang, T. Takeuchi, D. Bour, S. Corzine, M. Tan, and L. Mawst, "Temperature Analysis and Characteristics of Highly Strained InGaAs-GaAsP-GaAs ($\lambda > 1.17 \mu\text{m}$) Quantum-well Lasers," *IEEE J. Quantum Electron.* **38**, 640–651 (2002).
- [104] A. Mathur and P. Dapkus, "Fabrication, Characterization and Analysis of Low Threshold Current Density 1.55- μm -Strained Quantum-Well Lasers," *IEEE J. Quantum Electron.* **32**, 222–226 (1996).
- [105] C. Miller, "Intensity modulation and noise characterization of high-speed semiconductor lasers," *IEEE LTS.* **2**, 44–50 (1991).
- [106] M. Tatham, I. Lealman, C. Seltzer, L. Westbrook, and D. Cooper, "Resonance Frequency, Damping, and Differential Gain in 1.5 μm Multiple Quantum-Well Lasers," *IEEE J. Quantum Electron.* **28**, 408–414 (1992).
- [107] N. Yokouchi, N. Yamanaka, N. Iwai, Y. Nakahira, and A. Kasukawa, "Tensile-Strained GaInAsP-InP Quantum-Well Lasers Emitting at 1.3 μm ," *IEEE J. Quantum Electron.* **32**, 2148–2155 (1996).
- [108] H. Shimizu, K. Kumada, S. Uchiyama, and A. Kasukawa, "Extremely large differential gain of 1.26 μm GaInNAsSb-SQW ridge lasers," *Electron. Lett.* **37**, 28–30 (2001).
- [109] H. Shimizu, K. Kumada, S. Uchiyama, and A. Kasukawa, "Extremely Large Differential Gain of 1.26 μm GaInNAsSb-SQW Ridge Lasers," *Electron. Lett.* **37**, 28–30 (2001).

- [110] J. Ralston, S. Weisser, I. Esquivias, E. Larkins, J. Rosenzweig, P. Tasker, and J. Fleissner, "Control of Differential Gain, Nonlinear Gain, and Damping Factor for High-Speed Application of GaAs-Based MQW Lasers," *IEEE J. Quantum Electron.* **29**, 1648–1659 (1993).
- [111] L. Coldren and S. Corzine, *Diode Lasers and Photonic Integrated Circuits* (Wiley, New York, 1995), 1st ed., p56.
- [112] F. Masana, "A closed form solution of junction to substrate thermal resistance in semiconductor chips," *IEEE T Compon Pack A* **19**, 539–545 (1996).
- [113] J. Pikal, C. Menoni, H. Temkin, P. Thiagarajan, and G. Robinson, "Impedance independent optical carrier lifetime measurements in semiconductor lasers," *Rev. Sci. Inst.* **69**, 4247–4248 (1998).
- [114] O. Anton, D. Patel, C. Menoni, Y. Jeng-Ya, L. Mawst, J. Pikal, and N. Tansu, in *CLEO/IQEC and PhAST Technical Digest on CD-ROM (The Optical Society of America)* (Washington, DC, 2004), session CTuJ1.
- [115] URL <http://www.indium.com/products/alloychart.php>
- [116] URL http://emat.eng.hmc.edu/matlsprops/alloys/80au_20sn.htm
- [117] A. Mickelson, N. Basavanhally, and Y. Lee, *Optoelectronic Packaging* (Wiley, New York, 1997), 1st ed., p60.
- [118] URL <http://www.ioffe.ru/SVA/NSM/Semicond/GaAs/basic.html>
- [119] URL <http://www.ioffe.ru/SVA/NSM/Semicond/GaAs/thermal.html>
- [120] URL <http://www.ioffe.ru/SVA/NSM/Semicond/AlN/basic.html>
- [121] URL <http://www.edgepolishing.com/aluminum-nitride.htm>

- [122] URL <http://www.webelements.com/webelements/elements/text/Cu/>
- [123] URL http://www.diamonex.com/products_CVD.htm
- [124] URL <http://hypertextbook.com/facts/2004/KerryRemulla.shtml>
- [125] URL http://www.ddk.com/CVD/general_properties_of_cvd_diamon.htm
- [126] A. Mickelson, N. Basavanhally, and Y. Lee, *Optoelectronic Packaging* (Wiley, New York, 1997), 1st ed., pp59–67.

Index

- Absorption
 - Measured Results, 47–49, 55
 - Multiple Section Technique, 43–44
 - Spectral Features, 40
- Amplified Spontaneous Emission
 - Measurement Techniques, 41
 - PASE, 60–61
- Arrhenius Fit, 87–89

- Band Anti-Crossing Model
 - BAC, 19–23
- Band Structure
 - Calculations, 25–32
 - Measured Results, 52–55
- Bandgap Redshift, 40, 80
- Bandgap Renormalization
 - BGR, 40, 45, 47, 49, 55–57
 - Measured Results, 55–56
- Beam Collimation, 143–145
- Bowing Parameter, 17

- Carrier Density, 56–58, 86, 92, 99, 127, 131
 - Clamping, 58–60, 100
 - Effect On Recombination, 62–67
- Carrier Dynamics, 127–131
- Carrier Lifetime, *see* Differential Carrier Lifetime
- Characteristic Temperatures, 86–91
 - Laser Performance Modeling, 116
- Coupling Efficiency, *see* Fiber

- D Parameter, 93–95
- Damping Coefficient, 93–95
- Deep Level Trap Spectroscopy
 - DLTS, 138
- Deformation Potentials, 14
- Density Of States, 37, 64, 67
- Differential Carrier Lifetime, 98, 137–138
 - Definition, 95
 - Measured Results, 98
- Differential Gain, *see* Gain

- Effective Masses
 - Calculations, 27
 - Measured Results, 52
- Efficiency
 - External, 61, 73
 - 1st Generation, 34
 - 2nd Generation, 77, 79, 80, 82, 83
 - Length Dependence, 80
 - Simulation, 117–120
- Injection, 61
- Internal, 47, 58–62, 89
- Spreading, 61
- Electrical Spectrum Analyzer
 - ESA, 154–156
- Electronegativity, 19, 21, 22
- Erbium Doped Fiber Amplifier
 - EDFA, 5
- Exciton, 33, 40, 41, 75
 - Absorption Peak, 49
 - Binding Energy, 49
- External Quantum Efficiency, *see* Efficiency
- Eye Diagram
 - Simulations, 129
- Fabrication, 34–35
- Failure Rate, 76
- Fermi Level Pinning, 58–62
- Fermi-Dirac Statistics, 64–65
- Fiber
 - Attenuation, 1, 3
 - Capacity, 4
 - Coupling Efficiency, 143–145
 - Dispersion, 1
 - Dispersion Shifted, 5
- Gain, 45
 - Differential Gain, 94–95, 98–99
 - Measured Results, 98
 - Measured Results, 44–47
 - Multiple Section Technique, 41, 43–44
 - Nonlinear Gain Compression, 80, 95, 98–100, 129
 - Measured Results, 98
 - Spectral Features, 40
 - Versus Current, 45–47
- Growth, 34–35
- Heat Sinking, 146–153
- Heat Spreading, *see* Thermal Model
- Hole Burning, *see* Spectral Hole Burning

- Ideality Factor, 102–107
- Infrared Absorption, 3
- Integrating Sphere, 143
- Internal Loss, *see* Loss
- Internal Quantum Efficiency, *see* Efficiency
- Interpolation, 16–18
- Intersymbol Interference
 - ISI, 129
- Intervalence Band Absorption, 90

- Jitter, 129

- K Parameter, 94–95

- L-I-V
 - 1st Generation
 - CW, 73–74
 - Pulsed, 74
 - 2nd Generation
 - CW, 79, 82, 83
 - Pulsed, 80
 - Temperature Dependent, 87
 - Measurement Program, 164
 - Simulations, 116–117
- LabView Data Acquisition, 160
- Lambertian Surface, 143
- Langevin Noise Source, 92, 127
- Linewidth Enhancement Factor, 138
- Loss
 - Internal, 44, 47, 89
 - Mirror, 86
 - Effect On Performance, 120
- Luttinger Parameters, 14

- Mirror Damage, 98
- Mirror Loss, *see* Loss
- Modulation, 127–131, 138
- Molecular Beam Epitaxy, 34
- Multiband $\mathbf{k} \cdot \mathbf{p}$, 11–19

- Networks
 - Local Area, 1, 3
 - Long-Haul, 4, 5
 - Metro Area, 1, 4
 - Storage Area, 1
 - Wide Area, 1
- Noise
 - Amplifier, 92
 - Detector, 92, 159
 - Shot, 92, 159
 - Thermal, 92
- Non-Return To Zero Signal, 129
- Nonlinear Gain Compression, *see* Gain

- Photon Dynamics, 127–131
- Photoreflectance, 19, 55, 137
- Polarization, *see* Transverse Electric or Transverse Magnetic
- Quantum Confined Stark Effect
 - QCSE, 43
- Quasi-Fermi Level Separation, 55, 56
- Raman Amplifier, 5
- Rate Equations, 92, 127–131
- Rayleigh Distribution, 154–155
- Rayleigh Scattering, 3
- Recombination
 - Above Threshold, 61
 - Auger, 62–67
 - Distribution At Threshold, 69, 85
 - Effect on Gain, 89
 - Effect on Internal Efficiency, 90
 - Leakage, 63–67, 85
 - Measurement Technique, 36, 62–71, 84
 - Monomolecular, 33, 34, 62–67
 - Radiative, 62–67
 - Reduced Monomolecular, 79
 - Temperature Dependence, 70–71
 - Trap, 40, 61–62, 69–70
 - Effect On Reliability, 74–75, 100
- Relative Intensity Noise
 - Definition, 91–92
 - Measured Results, 95–100
 - Measurement With An ESA, 154–159
 - Optical Network Requirements, 92
 - Parameters, 93
 - Simulations, 129
 - Theory, 92–95
- Reliability
 - 1st Generation, 73–76
 - 2nd Generation, 100
- Resistance, *see* Series Resistance, Thermal Resistance
- Resonance Frequency, 93–94
- Schawlow-Townes linewidth, 93
- Series Resistance, 79–83, 103–106
- Shot Noise, *see* Noise
- Small Signal Response
 - Simulations, 129
- Spectral Hole Burning, 99–100
- Split Interstitials, 133
 - Effect On Reliability, 100
 - Energy Location, 39
 - Formation, 61
 - Partial Filling, 69

- Split-off Energy Δ , 13, 27
- Spontaneous Emission
 - Measured Results, 44
 - Multiple Section Technique, 43–44
 - Spectral Features, 36–41
- Spot Size Diameter, 144–145
- Stimulated Raman Scattering, 5
- Strain, 6, 14–17, 20, 30, 35
 - Barriers, 37, 61, 133
 - Effect On Differential Gain, 98
 - Effect On Reliability, 6, 74
 - QW, 37
 - Valence Band Splitting, 51
- Telecommunication Bands, 4
- Thermal Model, 109
- Thermal Resistance, 79–83, 108–114
- Threshold Voltage, 83
- Transverse Electric
 - Absorption Spectra, 47–49, 55
 - Gain Spectra, 44–47
 - Selection Rules, 37
 - Spontaneous Emission Spectra, 44
- Transverse Magnetic
 - Absorption Spectra, 47–49, 55
 - Gain Spectra, 44–47
 - Selection Rules, 37
 - Spontaneous Emission Spectra, 44
- Varshni Parameters, 18
- Voltage
 - V_0 , 103–108
- Waveguides, 114–116
- Wavelength Division Multiplexing
 - CWDM, 4
 - DWDM, 4–5
 - WDM, 4
- Z-Parameter, 74–75
 - 1st Generation, 68–71
 - Comparison Of Generations, 84–86
 - Theory, 62–67